Some contributions to model reduction of parametric systems in nonlinear mechanics

Tommaso Taddei

To cite this version:

Tommaso Taddei. Some contributions to model reduction of parametric systems in nonlinear mechanics. Mathematics [math]. École doctorale Mathématiques et Informatique, Université de Bordeaux, 2024. tel-04808369

HAL Id: tel-04808369
https://inria.hal.science/tel-04808369v1

Submitted on 28 Nov 2024

Université de Bordeaux

École doctorale de Mathématiques et informatique

Habilitation à Diriger les Recherches

Spécialité: Mathématiques appliquées

Présentée et soutenue par

Tommaso TADDEI

Some contributions to model reduction of parametric systems in nonlinear mechanics

Le **24 Avril 2024**

Jury :

M. Charbel FARHAT, Professeur
M. Yvon MADAY, Professeur
M. Angelo IOLLO, Professeur

Rapporteurs
M.me Virginie EHRLACHER, Chercheuse
M. Jan HESTHAVEN, Professeur
M. Mario OHLBERGER, Professeur

A Carlo e Sofia

Nonostante tutto c'è
la nostra stupida improbabile felicità

Acknowledgements

I would like to express my sincere gratitude to the members of the jury: Charbel Farhat, Yvon Maday, and Angelo Iollo, as well as the reviewers, Virginie Ehrlacher, Jan Hesthaven, and Mario Ohlberger, for their encouraging and very valuable comments on various aspects of my research.

In the process of writing this thesis, I have had the opportunity to look back at my research activity over the past few years as a member of the MEMPHIS team at Inria Bordeaux. Therefore, I would like to thank the people who have contributed to this work.

First of all, I would like to thank my PhD adviser Anthony Patera and my postdoc supervisor Yvon Maday: their constant support and invaluable guidance have played a pivotal role in shaping me into the researcher I am today.

I am deeply grateful to Angelo Iollo, the leader of the Inria team MEMPHIS, for warmly welcoming me into the team and for his wise leadership over the past six years. I am thankful to my colleagues in team MEMPHIS—Michel Bergmann, Afaf Bouharguane, Giuliano Carlino, Astrid Decoune, and Alessia del Grosso—for the many enlightening scientific discussions that have greatly broadened my understanding of various aspects of scientific computing; I also warmly thank our team assistant Anne-Laure Gautier: her continuous support in all these has played a pivotal role in the success of our team. In addition, I would like to thank my colleagues involved in the Chaire PROVE, particularly Denis Sipp: this experience has been extremely enriching and has opened up fascinating new research perspectives for me.

I want to extend special thanks to the PhD students and postdocs with whom I have had the privilege of collaborating over the years: Eki Agouzal, Birgul Koch, Jon Labatut, Abdessamad Moussaddak, Giulia Sambataro, Ishak Tifouti, and Lei Zhang. Contributing to the mentorship and training of these talented young researchers, while simultaneously learning from them, has undoubtedly been the most rewarding aspect of my work at Inria.

Several papers presented in this manuscript are done in collaboration with colleagues outside the MEMPHIS team. I would like to mention in particular Nicolas Barral, Andrea Ferrero, and Kathrin Smetana. Special thanks also to Masayuki Yano for the countless discussions on model reduction, discontinuous Galerkin methods and beyond, and to Pierre Mounoud for his decisive help with the theoretical results presented in Chapter 3.

One of the most captivating aspects of my tenure at Inria has been my active involvement in numerous industrial research projects, notably with EDF R&D and Optimad s.r.l. Through frequent interactions with talented researchers from these organizations — Jean-Philippe Argaud, Guilhem Fertè, Cedric Gouery, and Angelique Ponçot from EDF, as well as Haysam Telib from Optimad s.r.l. — I gained invaluable insights into the practical application of concepts stemming from my research activities. These exchanges not only allowed me to witness firsthand the implementation of ideas derived from my work but also provided me with a deeper understanding of the challenges that currently hinder the widespread adoption of model reduction techniques in industrial contexts.

The writing of this manuscript coincided with the birth of my son Carlo. In light of this, I would like to thank my parents Laura and Marzio for their constant support and my wife Sofia for always being by my side, even when thousands of kilometers separate us. To my wife Sofia and to our son Carlo this thesis is dedicated.

Contents

Chapter 1

Introduction

1.1 Outline of the document

This manuscript deals with the work on model order reduction (MOR) methods that I carried out at Sorbonne University and at Inria Bordeaux since my arrival in October 2018; the manuscript is divided into three chapters.

The first chapter focuses on linear-subspace model reduction of parametric systems. The chapter reviews some key elements of MOR techniques for parametric partial differential equations (PDEs) including hyper-reduction, greedy sampling, and *a posteriori* error estimation; it discusses the least-square Petrov-Galerkin formulation developed in [TT19], my postdoctoral work on the stabilization of Galerkin ROMs for turbulent flows [TT7], the treatment of parameterized geometries [TT17], the application of MOR techniques to structural mechanics problems with internal variables [TT8] and their integration with an industrial finite element (FE) code (`code_aster`) that is broadly used in nonlinear mechanics [TT2]. The work of this chapter is in collaboration with E. Agouzal, J.P. Argaud, M. Bergmann, G. Ferté, L. Fick, A. Iollo, Y. Maday, A.T. Patera, G. Sambataro and L. Zhang.

The second chapter deals with the development and the analysis of registration methods for model reduction. In their full generality, registration techniques aim to identify a deformation map that minimizes a suitable merit function; in the MOR framework, registration methods are designed to identify and then track coherent structures of compact support, such as shocks or shear layers, to facilitate the task of approximating the solution to a parametric PDE. In this chapter, I first review the problem of registration in bounded geometries; then, I discuss the application of registration methods to projection-based MOR and finally I review the application to non-intrusive MOR. I first proposed a general registration procedure for bounded domains in [TT13]; I further developed the methodology of [TT13] in a series of works with several coauthors [TT6, TT14, TT18, TT19]. The presentation of the second chapter is based on the recent works [TT15], [TT4] and [TT5]. The work on registration is in collaboration with N. Barral, S. Cucchiara, A. Ferrero, A. Iollo, H. Telib, I. Tifouti, and L. Zhang.

The third chapter deals with the development of component-based (CB) MOR techniques for large-scale systems: CB MOR techniques rely on the introduction of a library of components for which a local reduced-order approximation and a local reduced-order model (ROM) are built during an offline stage; given a new configuration, components from the library are instantiated to form the global system and then the global solution is estimated by gluing together the local ROMs. The deployment of an effective CB-ROM relies on two distinct building blocks: first, a data compression strategy for the construction of local reduced-order approximations for each archetype component; second, a rapid and reliable domain decomposition (DD) strategy for online global predictions. I first present a general data compression procedure that combines randomized localized training based on oversampling with adaptive enrichment based on global reduced-order solves [TT11]; then, I present an optimization-based overlapping DD strategy first proposed in [TT9] for a nonlinear mechanics problem based on a neo-Hookean constitutive law. The work of this chapter is in collaboration with A. Iollo, G. Sambataro, and K. Smetana.

1.2 Publication list

I list below my full list of publications. I distinguish between (i) journal publications from works completed before the PhD defense, (ii) journal publications from works completed after the PhD defense, (iii) papers that are currently under review, and (iv) conference proceedings.

Publications from works completed during the PhD or before

1. T. Taddei, S. Perotto, A. Quarteroni, *Reduced basis techniques for nonlinear conservation laws.* ESAIM: Mathematical Modelling and Numerical Analysis (M2AN), 2015.
2. T. Taddei, A. Quarteroni, S. Salsa, *An Offline-Online Riemann solver for one-dimensional systems of conservation laws.* Vietnam Journal of Mathematics, 2016.
3. T. Taddei, J.D. Penn, A.T. Patera, *Validation by Monte Carlo sampling of experimental observation functionals.* International Journal for Numerical Methods in Engineering, 2017.
4. T. Taddei, *An adaptive parametrized-background data-weak approach to variational data assimilation.* ESAIM: Mathematical Modelling and Numerical Analysis, 2017.
5. T. Taddei, J. D. Penn, M. Yano, A. T. Patera, *Simulation-Based Classification; a model-order-reduction approach for Structural Health Monitoring.* Archives of Computational Methods in Engineering (S.I.: Machine Learning in Computational Mechanics), 2018.
6. T. Taddei, A. T. Patera, *A localization strategy for data assimilation; application to state estimation and parameter estimation.* SIAM Journal on Scientific Computing (SISC), 2018.

Publications from works completed after the PhD

7. P. Gallinari, Y. Maday, M. Sangnier, O. Schwander, T. Taddei, *Reduced basis' acquisition by a learning process for rapid on-line approximation of solution to PDE's: Laminar Flow Past a Backstep.* Archives of Computational Methods in Engineering (S.I.: Machine Learning in Computational Mechanics), 2018.
8. L. Fick, Y. Maday, A. T. Patera, T. Taddei, *A stabilized POD model for turbulent flows over a range of Reynolds numbers: optimal parameter sampling and constrained projection.* Journal of Computational Physics, 2018.
9. Y. Maday, T. Taddei, *Adaptive PBDW approach to state estimation: noisy observations; user-defined update spaces.* SIAM Journal on Scientific Computing (SISC), 2019.
10. T. Taddei, *An offline/online procedure for dual norm calculations of parameterized functionals: empirical quadrature and empirical test spaces.* Advances in Computational Mathematics (ACOM), 2019.
11. T. Taddei, *A registration method for model order reduction: data compression and geometry reduction.* SIAM Journal on Scientific Computing (SISC), 2020.
12. T. Taddei, L. Zhang, *Space-time registration-based model reduction of parameterized one-dimensional hyperbolic PDEs.* ESAIM: Mathematical Modelling and Numerical Analysis, 2021.
13. T. Taddei, L. Zhang, *A discretize-then-map approach for the treatment of parameterized geometries in model order reduction.* Computer Methods in Applied Mechanics and Engineering (CMAME), 2021.
14. T. Taddei, L. Zhang, *Registration-based model reduction in complex two-dimensional geometries.* Journal of Scientific Computing (JSC), 2021.
15. A. Ferrero, T. Taddei, L. Zhang, *Registration-based model reduction of parameterized two-dimensional conservation laws.* Journal of Computational Physics (JCP), 2021.
16. A. Iollo, G. Sambataro, T. Taddei, *A projection-based model reduction method for nonlinear mechanics with internal variables: application to thermo-hydro-mechanical systems.* International Journal for Numerical Methods in Engineering (IJNME), 2022.
17. A. Iollo, T. Taddei, *Mapping of coherent structures in parameterized flows by learning optimal transportation with Gaussian models.* Journal of Computational Physics (JCP), 2022.
18. A. Iollo, G. Sambataro, T. Taddei, *A one-shot overlapping Schwartz method for component-based model reduction: application to nonlinear elasticity.* Computer Methods in Applied Mechanics and Engineering (CMAME), 2023.
19. K. Smetana, T. Taddei, *Localized model reduction for nonlinear elliptic partial differential equations: localized training, partition of unity, and adaptive enrichment.* SIAM Journal on Scientific Computing (SISC), 2023.

20. E. Agouzal, J.P. Argaud, M. Bergmann, G. Ferté, T. Taddei, *A projection-based reduced-order model for parametric quasi-static nonlinear mechanics using an open-source industrial code.* International Journal for Numerical Methods in Engineering (IJNME), 2024.
21. N. Barral, T. Taddei, I. Tifouti, *Registration-based model reduction of parameterized PDEs with spatio-parameter adaptivity.* Journal of Computational Physics (JCP), 2024.
22. E. Agouzal, T. Taddei, *Accelerated construction of projection-based reduced-order models via incremental approaches.* Advanced Modeling and Simulation in Engineering Sciences (AMSES), 2024.
23. T. Taddei, X. Xu, L. Zhang. *A non-overlapping optimization-based domain decomposition approach to component-based model reduction of incompressible flows.* Journal of Computational Physics (JCP), *accepted.*

Submitted papers

24. T. Taddei, *An optimization-based registration approach to geometry reduction.* 2022.
25. T. Taddei, *Compositional maps for registration in complex geometries.* 2023.
26. S. Cucchiara, A. Iollo, T. Taddei, H. Telib, *Model order reduction by convex displacement interpolation.* 2023.
27. E. Agouzal, J.P. Argaud, M. Bergmann, G. Ferté, S.Michel-Ponnelle, T. Taddei, *Projection-based model order reduction for prestressed concrete with an application to the standard section of a nuclear containment building.* 2023.

Conference proceedings

28. Y. C. Taumhas, D. Labeurthre, F. Madiot, O. Mula, T. Taddei, *Impact of physical model error on state estimation for neutronics applications.* ESAIM: Proceedings and Surveys (CEMRACS 2021), 2023.
29. D. Q. Bui, P. Mollo, F. Nobile, T. Taddei, *A component-based data assimilation strategy with applications to vascular flows.* ESAIM: Proceedings and Surveys (CEMRACS 2021), 2023.
30. A. Iollo, G. Sambataro, T. Taddei, *An optimization-based model order reduction approach for coupled problems: application to thermo-hydro-mechanical systems.* Proceedings of the conference COUPLED 2023, *submitted.*

1.3 Advising activities

Since my arrival in Bordeaux, I have had the opportunity to advise the work of several PhD students and post-doctoral fellows.

PhD students:

1. Giulia Sambataro, University of Bordeaux – Inria, *defended on December 13th, 2022.*
   Title: Component-based model order reduction strategies for THM equations.
   Co-adviser: Angelo Iollo;
2. Eki Agouzal, University of Bordeaux – Inria (industrial PhD thesis, with EDF), *started in April 2021.*
   Title: Estimation of the mechanical behavior of containment by data assimilation.
   Co-adviser: Michel Bergmann;
3. Ishak Tifouti, University of Bordeaux – Inria, *started in October 2022.*
   Title: Registration-based model reduction with mesh adaptation.
   Co-adviser: Nicolas Barral.
4. Jon Labatut, University of Bordeaux – Inria and Onera, *started in October 2022.*
   Title: Identification and adaptive mapping of coherent structures in parameterized compressible flows. Application to model order reduction.
   Co-adviser: Angelo Iollo.
5. Abdessamad Moussadak, University of Bordeaux – Inria (industrial PhD thesis, with EDF) *started in December 2023.*
   Title: Model reduction for river and coastal hydraulics.
   Co-adviser: Astrid Decoune.

Postdoctoral fellows:

1. Lei Zhang, Inria, *October 2019 – September 2021.*
   Title of the project: Nonlinear reduction strategies for hyperbolic problems.
2. Birgul Koc, Inria-IFPEN *June 2022 – November 2023.*
   Title of the project: Nonlinear reduction strategies for porous media problems
   Co-adviser: Angelo Iollo.

Chapter 2

Linear-subspace model reduction of parametric systems

Numerical modeling and simulation is of paramount importance to predict the response, improve the design, and monitor the structural health of physical and biological systems. Mathematical models are often in the form of partial differential equations (PDEs) and depend on several parameters (e.g., geometric features, operating conditions, material properties): accurate predictions hence require extensive explorations of the parameter domain, which might be prohibitively expensive for standard (e.g., finite element) methods. Model order reduction (MOR) aims to reduce the marginal cost associated with the solution to parameterized systems; model reduction is motivated by *many-query* (optimization, parameter sweeps) and *real-time* (interactive design, monitoring) applications, which naturally arise in the field of continuum mechanics.

This chapter summarizes my contributions to linear-subspace (or linear) projection-based model order reduction (PMOR) of parametric PDEs. The distinctive features of linear PMOR are twofold: first, the approximation of the state field through a linear or affine expansion of parameter-independent empirical modes with parameter-dependent coefficients that are determined by solving a suitable physics-informed reduced-order model (ROM); second, an offline-online computational decomposition to reduce the marginal cost to solve the ROM for new parameter values. In section 2.1, I briefly review the key elements of PMOR techniques, I introduce relevant notation that is used in the remainder of the manuscript, I illustrate some key challenges of PMOR methods, and I present the hyper-reduced least-square Petrov-Galerkin (LSPG) formulation that is employed in the remainder of the manuscript for the approximation of nonlinear conservation laws. In section 2.2, I present my works on Galerkin ROMs for nonlinear problems in structural mechanics [TT2, TT8] ; in section 2.3, I discuss my postdoctoral work on the stabilization of Galerkin ROMs for turbulent flows [TT7]; in section 2.4, I review the work on the treatment of parametric geometries in PMOR [TT17]. Section 2.5 offers some insights on ongoing efforts on the subject.

2.1 Projection-based model reduction of parametric PDEs

The past two decades have witnessed dramatic advances in the development of PMOR techniques for linear and nonlinear PDEs based on linear or affine approximations. Below, I summarize the key elements of MOR techniques based on the offline/online computational paradigm, with emphasis on steady-state problems. In particular, I review least-square Petrov-Galerkin [20] (or minimum residual [64]) formulations for non-symmetric problems. In this regard, I developed in collaboration with Lei Zhang a new hyper-reduced LSPG formulation [TT4, TT6, TT19] for parametric conservation laws of the form

$$\nabla \cdot F_\mu(u_\mu, \nabla u_\mu) = S_\mu(u_\mu) \quad \text{in } \Omega, \tag{2.1}$$

where $\Omega \subset \mathbb{R}^d$ is a d-dimensional Lipschitz domain. This formulation is employed in Chapter 3 in combination with registration techniques for the approximation of first-order conservation laws featuring shock-dominated flows.

2.1.1 Preliminary definitions

I denote by $\mu = [\mu_1, \ldots, \mu_P]$ the vector of P parameters in the parameter region $\mathcal{P}$; then, I introduce the solution field $u_\mu : \Omega \to \mathbb{R}^D$, $u_\mu \in \mathcal{X}$, such that

$$\mathfrak{R}_\mu(u_\mu, v) = 0 \quad \forall\, v \in \mathcal{Y}, \tag{2.2}$$

where $D > 0$ denotes the number of state variables, $\left(\mathcal{X}, \|\cdot\| = \sqrt{(\cdot,\cdot)}\right)$ and $\left(\mathcal{Y}, |||\cdot||| = \sqrt{((\cdot,\cdot))}\right)$ are suitable Hilbert spaces in Ω, and $\mathfrak{R}_\mu : \mathcal{X} \times \mathcal{Y} \to \mathbb{R}$ is a linear or nonlinear variational form that depends on $\mu \in \mathcal{P}$. Problem (2.2) might correspond to a space-only variational formulation of a steady PDE or to a space-time formulation of an unsteady PDE: in this manuscript, (2.2) refers to the variational formulation of the steady conservation law (2.1). I denote by $\mathcal{M} := \{u_\mu : \mu \in \mathcal{P}\}$ the solution manifold, which collects the solutions to the problem of interest for all parameters in $\mathcal{P}$.

In view of the numerical discretization, I introduce the high-fidelity (HF) mesh $\mathcal{T}_{\rm hf} = \left(\{x_i^{\rm hf}\}_{i=1}^{N_{\rm v}}, \texttt{T}\right)$ where $\{x_i^{\rm hf}\}_{i=1}^{N_{\rm v}} \subset \overline{\Omega}$ are the nodes of the mesh and $\texttt{T}$ is the connectivity matrix that links the nodes of the mesh to the elements — that is, $\texttt{T}_{k,i} \in \{1,\ldots,N_{\rm v}\}$ contains the index of the i-th node of the k-th element of the mesh. I denote by $\widehat{\texttt{D}} = \{\tilde{x} \in [0,1]^d : \sum_{i=1}^d (\tilde{x})_i < 1\}$ the reference element and by $\texttt{D}_1,\ldots,\texttt{D}_{N_{\rm e}}$ the elements of the mesh. I denote by $\mathcal{X}_{\rm hf}$ and $\mathcal{Y}_{\rm hf}$ the (continuous or discontinuous) trial and test finite element (FE) spaces associated with the mesh $\mathcal{T}_{\rm hf}$ and I define $N_{\rm hf} = \dim(\mathcal{X}_{\rm hf}) = \dim(\mathcal{Y}_{\rm hf})$: $\mathcal{X}_{\rm hf}$ and $\mathcal{Y}_{\rm hf}$ might differ due to the choice of the inner product and due to the treatment of Dirichlet boundary conditions.

I consider a FE isoparametric discretization of the geometry. I define the Lagrangian basis $\{\ell_i\}_{i=1}^{n_{\rm lp}}$ of the polynomial space $\mathbb{P}_{\texttt{p}}(\widehat{\texttt{D}})$ associated with the nodes $\{\tilde{x}_i\}_{i=1}^{n_{\rm lp}}$; then, I introduce the mappings $\{\Psi_k^{\rm fe}\}_k$ such that

$$\Psi_k^{\rm fe}(\tilde{x}) = \sum_{i=1}^{n_{\rm lp}} x^{\rm hf}_{\texttt{T}_{k,i}} \, \ell_i(\tilde{x}). \tag{2.3}$$

Note that $\Psi_k^{\rm fe}$ is completely characterized by the nodes in the k-th element $\texttt{X}_k^{\rm hf} := \{x^{\rm hf}_{\texttt{T}_{k,i}}\}_{i=1}^{n_{\rm lp}}$, $k = 1,\ldots,N_{\rm e}$. I introduce the bases $\{\phi_i^{\rm hf}\}_{i=1}^{N_{\rm hf}}$ and $\{\nu_i^{\rm hf}\}_{i=1}^{N_{\rm hf}}$ of $\mathcal{X}_{\rm hf}$ and $\mathcal{Y}_{\rm hf}$, respectively. Given $u \in \mathcal{X}_{\rm hf}$ (resp., $v \in \mathcal{Y}_{\rm hf}$), I denote by $\mathbf{u} \in \mathbb{R}^{N_{\rm hf}}$ (resp., $\mathbf{v} \in \mathbb{R}^{N_{\rm hf}}$) the corresponding FE vector

$$u = \sum_{i=1}^{N_{\rm hf}} (\mathbf{u})_i \phi_i^{\rm hf}, \quad v = \sum_{i=1}^{N_{\rm hf}} (\mathbf{v})_i \nu_i^{\rm hf}. \tag{2.4}$$

In view of geometrical parametrizations, given the family of parameterized domains $\{\Omega_\mu : \mu \in \mathcal{P}\}$ and the reference domain Ω, I introduce the parametric mapping $\Phi : \Omega \times \mathcal{P} \to \mathbb{R}^d$ such that $\Phi_\mu := \Phi(\cdot;\mu)$ is a bijection from Ω to the physical domain Ω_μ for any $\mu \in \mathcal{P}$. I further define the "mapped" mesh $\Phi_\mu(\mathcal{T}_{\rm hf}) := \left(\{\Phi_\mu(x_i^{\rm hf})\}_{i=1}^{N_{\rm v}}, \texttt{T}\right)$, which shares with $\mathcal{T}_{\rm hf}$ the same topology. For nodal continuous or discontinuous formulations, the vector $\mathbf{u}$ contains the evaluation of the FE field u in the nodes of the mesh: we hence find that, if $(\Phi_\mu(\mathcal{T}_{\rm hf}), \mathbf{u})$ is an approximation of the field u, the pair $(\mathcal{T}_{\rm hf}, \mathbf{u})$ approximates $u \circ \Phi_\mu$.

Then, I introduce the HF estimate $u_\mu^{\rm hf}$ of the solution field as the solution to the problem:

$$\text{find } u_\mu^{\rm hf} \in \mathcal{X}_{\rm hf} \text{ s.t. } \mathfrak{R}_\mu^{\rm hf}(u_\mu^{\rm hf}, v) = 0 \quad \forall\, v \in \mathcal{Y}_{\rm hf}, \tag{2.5}$$

where $\mathfrak{R}_\mu^{\rm hf} : \mathcal{X}_{\rm hf} \times \mathcal{Y}_{\rm hf} \to \mathbb{R}$ is the HF residual associated with the PDE model (2.2) and the HF discretization. In view of the discussion, I also write the algebraic counterpart of (2.5):

$$\text{find } \mathbf{u}_\mu^{\rm hf} \in \mathbb{R}^{N_{\rm hf}} \text{ s.t. } \mathbf{R}_\mu^{\rm hf}\left(\mathbf{u}_\mu^{\rm hf}\right) = 0, \quad \text{where } \left(\mathbf{R}_\mu^{\rm hf}\left(\mathbf{u}_\mu^{\rm hf}\right)\right)_i = \mathfrak{R}_\mu^{\rm hf}(u_\mu^{\rm hf}, \nu_i^{\rm hf}),\ i = 1,\ldots,N_{\rm hf}; \tag{2.6}$$

furthermore, I explicitly write the residual as

$$\mathfrak{R}_\mu^{\rm hf}(w,v) = \sum_{k=1}^{N_{\rm e}} \mathfrak{r}_{k,\mu}^{\rm hf,e}(E_k w, E_k v) + \sum_{j=1}^{N_{\rm f}} \mathfrak{r}_{j,\mu}^{\rm hf,f}(E_j^{\rm f} w, E_j^{\rm f} v) \tag{2.7}$$

where $N_{\rm e}$ is the total number of elements of the mesh, $N_{\rm f}$ is the total number of facets, $E_k w$ is the restriction of the FE field w to the k-th element of the mesh, while $E_j^{\rm f} w$ is the restriction of w to the j-th facet of the mesh and possibly to the neighboring elements. I also define the Jacobian of $\mathfrak{R}_\mu^{\rm hf}$ at $w \in \mathcal{X}_{\rm hf}$, $\mathfrak{J}_\mu^{\rm hf}[w] : \mathcal{X}_{\rm hf} \times \mathcal{Y}_{\rm hf} \to \mathbb{R}$, such that

$$\mathfrak{J}_\mu^{\rm hf}[w](u,v) := \lim_{\epsilon \to 0} \frac{1}{\epsilon}\left(\mathfrak{R}_\mu^{\rm hf}(w + \epsilon u, v) - \mathfrak{R}_\mu^{\rm hf}(w,v)\right). \tag{2.8}$$

I introduce the symmetric positive definite (SPD) matrices $\mathbf{X}, \mathbf{Y} \in \mathbb{R}^{N_{\rm hf} \times N_{\rm hf}}$ associated with the inner products of $\mathcal{X}, \mathcal{Y}$, that is

$$(u,v) = \mathbf{v}^\top \mathbf{X} \mathbf{u}, \quad ((w,z)) = \mathbf{z}^\top \mathbf{Y} \mathbf{w}, \tag{2.9}$$

for all $u, v \in \mathcal{X}_{\rm hf}$ and $w, z \in \mathcal{Y}_{\rm hf}$; the choice of $\mathbf{X}, \mathbf{Y}$ is closely related to the particular PDE of interest and is briefly discussed below. Given the functional $F : \mathcal{Y}_{\rm hf} \to \mathbb{R}$, I define the vector $\mathbf{F} \in \mathbb{R}^{N_{\rm hf}}$ such that $(\mathbf{F})_i = F(\nu_i^{\rm hf})$ for $i = 1,\ldots,N_{\rm hf}$. I denote by $\mathcal{Y}'_{\rm hf}$ the dual space of $\mathcal{Y}_{\rm hf}$, and I introduce the dual norm

$$\|F\|_{\mathcal{Y}'_{\rm hf}} := \sup_{v \in \mathcal{Y}_{\rm hf}} \frac{F(v)}{|||v|||} = \sqrt{\mathbf{F}^\top \mathbf{Y}^{-1} \mathbf{F}}. \tag{2.10}$$

I introduce the Riesz operator $R_{\mathcal{Y}_{\rm hf}} : \mathcal{Y}_{\rm hf}' \to \mathcal{Y}_{\rm hf}$ such that $f = R_{\mathcal{Y}_{\rm hf}}(F)$ satisfies

$$((f, v)) = F(v) \quad \forall\, v \in \mathcal{Y}_{\rm hf}; \tag{2.11}$$

note that $\mathbf{f} = \mathbf{Y}^{-1}\mathbf{F}$, for any $F \in \mathcal{Y}_{\rm hf}'$. Given the linear subspace $\mathcal{Z} \subset \mathcal{X}_{\rm hf}$, I further define the projection operator $\Pi_{\mathcal{Z}} : \mathcal{X}_{\rm hf} \to \mathcal{Z}$ such that

$$\Pi_{\mathcal{Z}} u = \arg \min_{w \in \mathcal{Z}} \|w - u\|. \tag{2.12}$$

Linear (or affine) MOR approaches seek approximations of the form $\widehat{u}_\mu = Z \widehat{\boldsymbol{\alpha}}_\mu$ where $\widehat{\boldsymbol{\alpha}}_\mu \in \mathbb{R}^n$ is a vector of parameter-dependent generalized coordinates and $Z : \mathbb{R}^n \to \mathcal{X}_{\rm hf}$ is either a linear or an affine operator,

$$Z\boldsymbol{\alpha} = \sum_{i=1}^{n} (\boldsymbol{\alpha})_i \zeta_i \quad \text{(linear ansatz)}, \qquad Z\boldsymbol{\alpha} = \bar{u} + \sum_{i=1}^{n} (\boldsymbol{\alpha})_i \zeta_i \quad \text{(affine ansatz)}, \quad \forall\, \boldsymbol{\alpha} \in \mathbb{R}^n, \tag{2.13}$$

with $\bar{u}, \zeta_1, \ldots, \zeta_n \in \mathcal{X}_{\rm hf}$. In the remainder, Z is dubbed the reduced-order basis (ROB) of the MOR procedure.

A reduced-order model provides an explicit or implicit definition of the generalized coordinates (or latent variables) $\widehat{\boldsymbol{\alpha}}_\mu \in \mathbb{R}^n$ such that $\widehat{u}_\mu = Z\widehat{\boldsymbol{\alpha}}_\mu$ is an estimate of the state for the parameter $\mu \in \mathcal{P}$. PMOR techniques rely on the projection of the state equations onto a suitable test space to obtain a rapid and reliable ROM for the generalized coordinates $\widehat{\boldsymbol{\alpha}}_\mu$. Specifically, PMOR methods rely either on Galerkin projection or (least-square) Petrov-Galerkin projection.

2.1.2 Offline-online decomposition

PMOR techniques rely on an offline/online decomposition to reduce marginal costs. During the offline or learning phase, the solution to the HF model (2.5) is estimated for several parameter values to generate the ROB Z and the ROM (2.14) (or (2.20)) for the generalized coordinates. During the online or prediction phase, given a new value of the parameter, the ROM is solved to rapidly estimate the solution field and relevant quantities of interest. A PMOR technique for (2.5) comprises three building blocks: (i) a data compression strategy for the construction of the ROB Z in (2.13) for the HF solution manifold $\mathcal{M}_{\rm hf} := \left\{ u_\mu^{\rm hf} : \mu \in \mathcal{P} \right\}$; (ii) a ROM for the rapid and reliable prediction of the solution $u_\mu^{\rm hf}$ for any value of the parameter; and (iii) an *a posteriori* error estimator for certification. Algorithm 1 summarizes the key steps of the offline/online computational procedure for (2.5): I refer to [13, 44, 78, 82] for a thorough discussion on the various elements of the approach.

Algorithm 1 Offline/online computational paradigm for (2.5)

```
Offline stage.                                                        expensive, performed once.
1: Sampling: compute $u_{\mu^1}^{\rm hf}, \ldots, u_{\mu^{n_{\rm train}}}^{\rm hf} \in \mathcal{M}_{\rm hf}$ using the HF solver.
2: Data compression: compute the operator $Z : \mathbb{R}^n \to \mathcal{X}_{\rm hf}$.
3: ROM construction: define the ROM for the solution coefficients.   $\to$ ${\rm ROM}_n : \mu \in \mathcal{P} \mapsto \widehat{\boldsymbol{\alpha}}_\mu$

Online stage.                                     inexpensive, performed for any new $\mu \in \mathcal{P}$.
1: ROM evaluation: given $\mu \in \mathcal{P}$, compute $\widehat{\boldsymbol{\alpha}}_\mu = {\rm ROM}_n(\mu)$ and $\widehat{u}_\mu := Z\widehat{\boldsymbol{\alpha}}_\mu$.
2: Error estimation: estimate the error $\|u_\mu^{\rm hf} - \widehat{u}_\mu\|$.
```

Research in PMOR focuses on the development and analysis of each building block of Algorithm 1 for parametric (elliptic, parabolic, hyperbolic) PDEs. The weak-greedy algorithm [94] and its extension to unsteady PDE [39] are prominent techniques for adaptive sampling of the parameter domain; proper orthogonal decomposition (POD, [88, 95]) is broadly used to build the low-dimensional ROB using a set of snapshots; *a posteriori* error estimators are typically based on the $\mathcal{Y}'$ norm of the discrete residual and might be corrected by a suitable stability factor to determine a rigorous upper bound for the error [50, 98]. In the next section, I comment on Galerkin and Petrov-Galerkin schemes for the definition of the ROM.

2.1.3 Galerkin and Petrov-Galerkin reduced order models

I denote by $\mathcal{Z} \subset \mathcal{X}_{\rm hf}$ the reduced space spanned by $\zeta_1, \ldots, \zeta_n \in \mathcal{X}_{\rm hf}$ in (2.13), $\mathcal{Z} = {\rm span}\{\zeta_i\}_{i=1}^n$. Galerkin ROMs are obtained by projecting the state equations onto the same ROB used for approximation:

$$\text{find } \widehat{u}_\mu = Z\widehat{\boldsymbol{\alpha}}_\mu \text{ s.t. } \widehat{\mathfrak{R}}_\mu(Z\widehat{\boldsymbol{\alpha}}_\mu, v) = 0 \quad \forall\, v \in \mathcal{Z}. \tag{2.14}$$

Note that Galerkin ROMs involve the surrogate residual $\widehat{\mathfrak{R}}$ as opposed to the HF residual $\mathfrak{R}^{\rm hf}$: the problem of determining an accurate and rapidly computable surrogate of the HF residual is referred to as *hyper-reduction*

[84] and is key for the efficiency of MOR procedures. Galerkin projection is provably optimal for coercive problems but might be unstable for linear inf-sup stable and nonlinear problems: the inadequacy of Galerkin ROMs to deal with important classes of PDEs has motivated the development of least-square Petrov-Galerkin (or minimum residual) ROMs.

Maday et al. [64] (see also [77, section 5.3.1]) proposed to minimize the weighted residual:

$$\widehat{\boldsymbol{\alpha}}_\mu \in \arg\min_{\boldsymbol{\alpha}\in\mathbb{R}^n} \sup_{v\in\mathcal{Y}} \frac{\mathfrak{R}_\mu^{\rm hf}(Z\boldsymbol{\alpha}, v)}{|||v|||}. \tag{2.15}$$

If the problem of interest is linear and *parametrically-affine*, that is

$$\mathfrak{R}_\mu^{\rm hf}(u,v) = \sum_{q=1}^{Q_{\rm a}} (\boldsymbol{\Theta}_\mu^{\rm a})_q \mathfrak{A}_q(u,v) - \sum_{q=1}^{Q_{\rm f}} (\boldsymbol{\Theta}_\mu^{\rm f})_q F_q(v),$$

where $\mathfrak{A}_1,\ldots,\mathfrak{A}_{Q_{\rm a}}$ are suitable parameter-independent bilinear forms and $F_1,\ldots,F_{Q_{\rm f}}$ are parameter-independent linear forms, it is possible to show (see, e.g., [78, Chapter 3.7.1]) that[1]

$$\sup_{v\in\mathcal{Y}} \frac{\mathfrak{R}_\mu^{\rm hf}(Z\boldsymbol{\alpha}, v)}{|||v|||} = \sqrt{\boldsymbol{\Theta}_\mu^{\rm r}(\boldsymbol{\alpha})^\top \boldsymbol{\Sigma} \boldsymbol{\Theta}_\mu^{\rm r}(\boldsymbol{\alpha})}, \quad \text{where } \boldsymbol{\Theta}_\mu^{\rm r}(\boldsymbol{\alpha}) = \text{vec}\left(-\boldsymbol{\Theta}_\mu^{\rm f}, \boldsymbol{\Theta}_\mu^{\rm a}(\boldsymbol{\alpha})_1, \ldots, \boldsymbol{\Theta}_\mu^{\rm a}(\boldsymbol{\alpha})_n\right), \tag{2.16}$$

and $\boldsymbol{\Sigma} \in \mathbb{R}^{n_{\rm r}\times n_{\rm r}}$ is a parameter-independent symmetric positive semi-definite matrix, with $n_{\rm r} = Q_{\rm a} n + Q_{\rm f}$. Provided that the vector-valued functions $\boldsymbol{\Theta}_\mu^{\rm a} : \mathcal{P} \to \mathbb{R}^{Q_{\rm a}}$ and $\boldsymbol{\Theta}_\mu^{\rm f} : \mathcal{P} \to \mathbb{R}^{Q_{\rm f}}$ can be evaluated efficiently, we can exploit (2.16) to efficiently solve the minimum residual formulation (2.15) for parametrically-affine linear systems. Yano [98] extended the formulation to parametrically-affine problems with quadratic nonlinearities. However, the extension to general nonlinear non-affine problems requires the development of specialized hyper-reduction techniques.

Carlberg et al. [20] proposed an alternative hyper-reduced minimum residual formulation for general steady and unsteady nonlinear problems; the point of departure is the discrete system of equations (2.6). The authors of [20] rely on gappy proper orthogonal decomposition (gappy POD, [31]) to devise an efficient PROM for arbitrary nonlinear problems; since then, the method in [20] has been successfully applied to a broad range of steady and unsteady large-scale nonlinear CFD problems (see, e.g., [15, 96]). If we denote by $\{\mathbf{e}_k\}_{k=1}^{N_{\rm hf}}$ the canonical basis in $\mathbb{R}^{N_{\rm hf}}$, Carlberg proposed a low-rank approximation of the residual of the form

$$\mathbf{R}_\mu^{\rm hf}\left(\bar{\mathbf{u}} + \mathbf{Z}\boldsymbol{\alpha}\right) \approx \mathbf{Z}_{\rm r}\left(\mathbf{P}_{\rm s}^\top \mathbf{Z}_{\rm r}\right)^\dagger \mathbf{P}_{\rm s}^\top \mathbf{R}_\mu^{\rm hf}\left(\bar{\mathbf{u}} + \mathbf{Z}\boldsymbol{\alpha}\right), \tag{2.17}$$

where $\mathbf{Z}_{\rm r} \in \mathbb{R}^{N_{\rm hf}\times n_{\rm r}}$ is a reduced-order basis for the residual and $\mathbf{P}_{\rm s} = [\mathbf{e}_{i_1},\ldots,\mathbf{e}_{i_m}]$ with $i_1,\ldots,i_m \in \{1,\ldots,N_{\rm hf}\}$ and $m \geq n_{\rm r}$ is a sampling matrix; note that the approximation in (2.17) requires the evaluation of $m \ll N_{\rm hf}$ entries of the HF residual and is thus amenable for real-time computations. In conclusion, the formulation of [20] can be stated as

$$\text{find } \widehat{\boldsymbol{\alpha}}_\mu \in \arg\min_{\boldsymbol{\alpha}\in\mathbb{R}^n} \left\| \mathbf{Y}^{-1/2}\mathbf{Z}_{\rm r}\left(\mathbf{P}_{\rm s}^\top \mathbf{Z}_{\rm r}\right)^\dagger \mathbf{P}_{\rm s}^\top \mathbf{R}_\mu^{\rm hf}\left(\bar{\mathbf{u}} + \mathbf{Z}\boldsymbol{\alpha}\right)\right\|_2, \tag{2.18}$$

which can be efficiently solved using the Gauss-Newton method. Even if the formulation (2.18) can cope with arbitrary choices of the test norm matrix $\mathbf{Y}$, the authors of [20] consider diagonal test norms for which the computation of $\mathbf{Y}^{-1/2}$ is trivial.

In [TT19], together with Zhang, I considered a different least-square Petrov-Galerkin formulation based on the introduction of a so-called *empirical test space* — a closely-related technique has been recently presented in [29]. The point of departure is the variational statement (2.15). First, the high-dimensional test space $\mathcal{Y}$ is replaced by the low-dimensional space $\mathcal{Y}_m = \text{span}\{\psi_i\}_{i=1}^m \subset \mathcal{Y}$ with $m \geq n$,

$$\widehat{\boldsymbol{\alpha}}_\mu \in \arg\min_{\boldsymbol{\alpha}\in\mathbb{R}^n} \sup_{v\in\mathcal{Y}_m} \frac{\mathfrak{R}_\mu^{\rm hf}(Z\boldsymbol{\alpha}, v)}{|||v|||}. \tag{2.19}$$

Provided that $\{\psi_i\}_i$ is an orthonormal basis of $\mathcal{Y}_m$, we find that

$$\sup_{v\in\mathcal{Y}_m} \frac{\mathfrak{R}_\mu^{\rm hf}(Z\boldsymbol{\alpha}, v)}{|||v|||} = \|\widehat{\mathbf{R}}_\mu^{\rm hf}(\boldsymbol{\alpha})\|_2 \quad \text{where } \left(\widehat{\mathbf{R}}_\mu^{\rm hf}(\boldsymbol{\alpha})\right)_i = \mathfrak{R}_\mu^{\rm hf}(Z\boldsymbol{\alpha}, \psi_i) \;\; i = 1,\ldots,m;$$

therefore, (2.19) reads as a nonlinear least-square problem with m equations and n unknowns, which can be solved using standard optimization (Gauss-Newton, Levenberg-Marquardt) tools. Clearly, (2.19) is still

---

[1] I provide below the explicit formula for linear approximations; an analogous formula can be obtained for affine approximations; we omit the details.

expensive to solve due to the need to compute the HF integrals over the whole computational domain. Dedicated hyper-reduction strategies should thus be implemented to replace the HF residual in (2.19) with an inexpensive surrogate to ultimately obtain

$$\widehat{\boldsymbol{\alpha}}_\mu \in \arg\min_{\boldsymbol{\alpha}\in\mathbb{R}^n} \|\widehat{\mathbf{R}}_\mu(\boldsymbol{\alpha})\|_2 \quad \text{where} \quad \left(\widehat{\mathbf{R}}_\mu(\boldsymbol{\alpha})\right)_i = \widehat{\mathfrak{R}}_\mu(Z\boldsymbol{\alpha}, \psi_i) \;\; i = 1, \ldots, m. \tag{2.20}$$

2.1.4 Deployment of (2.20)

The practical construction of the LSPG ROM (2.20) requires (i) the definition of the trial ROB, (ii) the definition of the empirical test space $\mathcal{Y}_m$, (iii) the choice of the test norm $|||\cdot||| = \sqrt{((\cdot,\cdot))}$, (iv) the construction of the residual surrogate through hyper-reduction.

- *Construction of the trial ROB.* We resort to the weak-greedy algorithm (cf. [94]) to build the ROM and the trial ROB Z; the weak-greedy method relies on the repeated maximization of an error indicator to adaptively sample the parameter domain. In our implementation, we consider the $\mathcal{Y}'$ norm of the discrete residual to drive the greedy search.

- *Construction of the test space.* For linear problems, given the reduced space $\mathcal{Z} = \text{span}\{\zeta_i\}_{i=1}^n$, it is possible to show (cf. [TT19, Appendix C], see also [25]) that the stability of the LSPG formulation is guaranteed if and only if the test space $\mathcal{Y}_m$ approximates the manifold $\{R_{\mathcal{Y}_{\rm hf}}\mathfrak{J}_\mu[u_\mu]\ (\zeta_i,\cdot)\ :\ i = 1,\ldots,n, \mu \in \mathcal{P}\}$ where $R_{\mathcal{Y}_{\rm hf}}$ is introduced in (2.11) and $\mathfrak{J}_\mu$ denotes the Jacobian (cf. (2.8)). Therefore, in [TT19] (see also [TT17]), I proposed to construct the test space $\mathcal{Y}_m$ using proper orthogonal decomposition (POD) based on the method of snapshots [88]:

  $$\mathcal{Y}_m = \texttt{POD}\left(\{R_{\mathcal{Y}_{\rm hf}}\mathfrak{J}_\mu[u_\mu](\zeta_i,\cdot)\ :\ i = 1,\ldots,n,\ \ \mu \in \mathcal{P}_{\rm train}\},\ ((\cdot,\cdot)),\ m\right), \tag{2.21}$$

  where notation $\texttt{POD}\left(\{\mathcal{D}_{\rm train},\ ((\cdot,\cdot)),\ m\right)$ refers to the construction of the m-dimensional POD space associated with the dataset of snapshots $\mathcal{D}_{\rm train}$ and the inner product $((\cdot,\cdot))$. Notice that the test space $\mathcal{Y}_m$ (and then the LSPG formulation) strongly depends on the choice of the inner product.

- *Definition of the test norm.* The LSPG ROM critically depends on the choice of the inner product $((\cdot,\cdot))$, which enters in the POD for the construction of the test space $\mathcal{Y}_m$ (2.21). For the Reynolds-averaged incompressible Navier-Stokes equations (cf. section 2.4) with Spalart-Allmaras turbulence model considered in [TT17], we rely on the H^1 norm for velocity and turbulent viscosity and the L^2 norm for pressure — we add properly-chosen scaling factors to account for different units and different magnitudes (cf. [TT17, Eq. (47)]). For the compressible Euler equations, we consider a discrete H^1 norm: since we rely on the discontinuous Galerkin (DG) FE method for HF computations, we choose the form $((\cdot,\cdot))$ that corresponds to the symmetrized DG discretization of a reaction-diffusion operator with Neumann boundary conditions with BR2 diffusive flux (cf. [12]). A thorough analysis of the impact on performance of the choice of the inner product is the subject of ongoing research.

- *Hyper-reduction.* As discussed in [33], we might distinguish between approximate-then-project (e.g., [11, 21]) and reduced quadrature (e.g., [4, 32, 101]) approaches for hyper-reduction. Reduced quadrature approaches frame the problem of finding a low-dimensional yet accurate quadrature rule to estimate the integrals in $\mathfrak{R}^{\rm hf}$ associated with the elements of the test basis as a sparse representation problem and then resort to optimization methods to find an approximate solution to the latter. Reduced quadrature approaches inherit relevant stability and conservation properties [32, 99] from the underlying numerical scheme and allow us to leverage the fast and vectorized routines implemented in many FE/finite volume codes.

  We consider reduced quadrature rules based on sampling of mesh elements and facets; following [32], we rely on the non-negative least-square method to find the sparse quadrature rule. Exploiting notation introduced in (2.7), we consider the weighted residual:

  $$\mathfrak{R}_\mu^{\rm eq}(u,v) = \sum_{k=1}^{N_{\rm e}} \rho_k^{\rm eq,e}\mathfrak{r}_{k,\mu}^{\rm hf,e}(E_k w, E_k v) + \sum_{j=1}^{N_{\rm f}} \rho_k^{\rm eq,f}\mathfrak{r}_{j,\mu}^{\rm hf,f}(E_j^{\rm f} w, E_j^{\rm f} v) \quad \forall\, q, v \in \mathcal{X}_{\rm hf}, \tag{2.22}$$

  that depends on the sparse weights $\boldsymbol{\rho}^{\rm eq,e} \in \mathbb{R}^{N_{\rm e}}$ and $\boldsymbol{\rho}^{\rm eq,f} \in \mathbb{R}^{N_{\rm f}}$. I refer to [TT4] for a detailed description of the hyper-reduction procedure considered in the numerical experiments, and to [33] for a thorough review of hyper-reduction methods for nonlinear PDEs.

2.2 Hyper-reduced Galerkin ROMs for nonlinear problems in structural mechanics

The PhD project of Giulia Sambataro focused on the development of PMOR techniques for coupled problems in nonlinear mechanics with internal variables; the thesis was funded by ANDRA (French national radioactive waste management agency). The ongoing industrial PhD project of Eki Agouzal, which is funded by Electricité de France (EDF), aims to extend the work of Sambataro to three-dimensional problems and to integrate the Galerkin procedure in the open-source software `code_aster` [28].

2.2.1 Methodology

Given the parameter $\mu \in \mathcal{P}$, the Hilbert spaces $\mathcal{X}$ and $\mathcal{W}$ defined over the domain Ω, and the time interval $\mathtt{I} := (0, t_{\rm f}]$, we seek $(u_\mu, \gamma_\mu) \in C(\mathtt{I}; \mathcal{X}) \times C(\mathtt{I}; \mathcal{W})$ such that

$$\begin{cases} \mathfrak{R}_\mu(u_\mu(t), \partial_t u_\mu(t), \partial_{tt} u_\mu(t), \gamma_\mu(t), v) = 0 & \forall\, v \in \mathcal{X},\ t \in \mathtt{I}, \\[2mm] \partial_t \gamma_\mu(x,t) = \mathfrak{F}_\mu(\nabla u_\mu(x,t), \gamma_\mu(x,t)) & x \in \Omega,\ t \in \mathtt{I} \end{cases} \tag{2.23}$$

with suitable initial and boundary conditions. Here, u_μ is the set of state variables, while γ_μ is the vector of internal variables; $\mathfrak{R}_\mu$ denotes the variational form associated with the balance equations, which read as evolutionary PDEs and depend on the state and the internal variables; finally, $(2.23)_2$ is a system of parameterized ordinary differential equations that are associated with the material constitutive laws.

Problem (2.23) is discretized using a one-stage implicit time integrator and the continuous finite element (FE) method. We introduce the time grid $\{t^k\}_{k=1}^{N_{\rm t}}$ and the FE space $\mathcal{X}_{\rm hf} \subset \mathcal{X}$; we denote by $\Omega_{\rm qd} = \{x_i^{\rm qd}\}_{i=1}^{N_{\rm qd}}$ the set of quadrature points. Given the state estimate $u_\mu^{(k-1)} \in \mathcal{X}_{\rm hf}$ and the estimate $\gamma_\mu^{(k-1)}$ of the internal variables in the quadrature points $\Omega_{\rm qd}$ for $t = t^{k-1}$, we seek $(u_\mu^{(k)}, \gamma_\mu^{(k)})$ such that

$$\begin{cases} \mathfrak{R}_\mu^{\rm hf}(u_\mu^{(k)}, u_\mu^{(k-1)}, \gamma_\mu^{(k)}, v; \mu) = 0 & \forall\, v \in \mathcal{X}_{\rm hf}, \\[2mm] \gamma_\mu^{(k)}(x) = \mathfrak{F}_\mu^{\rm hf}\left(\nabla u_\mu^{(k)}(x), \gamma_\mu^{(k-1)}(x)\right) & x \in \Omega_{\rm qd} \end{cases} \tag{2.24}$$

for $k = 1, 2, \ldots, N_{\rm t}$, where $\mathfrak{R}^{\rm hf}$ and $\mathfrak{F}^{\rm hf}$ are suitable operators associated with the discretization of $\mathfrak{R}$ and $\mathfrak{F}$, respectively. Problem (2.24) is solved using an iterative (Newton) solver at each step to find $u_\mu^{(k)}$ and then $\gamma_\mu^{(k)}$.

In [TT8], we developed an hyper-reduced Galerkin ROM for (2.24), with application to thermo-hydro-mechanical (THM) systems. The distinctive features of our formulation are twofold: first, an elementwise empirical quadrature procedure for hyper-reduction; second, a POD-Greedy strategy for effective sampling of the parameter space. We introduce the reduced space $\mathcal{Z} = {\rm span}\{\zeta_i\}_{i=1}^n \subset \mathcal{X}_{\rm hf}$ and, recalling (2.7), the weighted residual

$$\widehat{\mathfrak{R}}_\mu(w, z, \gamma, v) = \sum_{k \in \mathtt{I}_{\rm eq,e}} \rho_k^{\rm eq,e} \mathfrak{r}_{k,\mu}^{\rm hf,e}(E_k w, E_k z, E_k \gamma, E_k v) + \sum_{j \in \in \mathtt{I}_{\rm eq,f}} \rho_j^{\rm eq,f} \mathfrak{r}_{j,\mu}^{\rm hf,f}(E_j^{\rm f} w, E_j^{\rm f} z, E_j^{\rm f} \gamma, E_j^{\rm f} v), \tag{2.25}$$

where $\mathtt{I}_{\rm eq,e} \subset \{1, \ldots, N_{\rm e}\}$ and $\mathtt{I}_{\rm eq,f} \subset \{1, \ldots, N_{\rm f}\}$ are suitable sets of indices that identify the *reduced mesh*, which corresponds to a subset of elements and facets of the HF mesh $\mathcal{T}_{\rm hf}$, used for PMOR computations, and $\boldsymbol{\rho}^{\rm eq,e} \in \mathbb{R}^{N_{\rm e}}$, $\boldsymbol{\rho}^{\rm eq,f} \in \mathbb{R}^{N_{\rm f}}$ are suitable sets of non-negative weights; we also introduce the set of quadrature nodes $\Omega_{\rm qd}^{\rm eq} \subset \Omega_{\rm qd}$ associated with the sampled elements and facets. Finally, we introduce the Galerkin ROM: find $\widehat{u}_\mu^{(k)} \in \mathcal{Z}$ and $\widehat{\gamma}_\mu^{(k)} : \Omega_{\rm qd}^{\rm eq} \to \mathbb{R}^{D_{\rm int}}$ such that

$$\begin{cases} \widehat{\mathfrak{R}}_\mu(u_\mu^{(k)}, u_\mu^{(k-1)}, \gamma_\mu^{(k)}, v; \mu) = 0 & \forall\, v \in \mathcal{Z}, \\[2mm] \gamma_\mu^{(k)}(x) = \mathfrak{F}_\mu^{\rm hf}\left(\nabla u_\mu^{(k)}(x), \gamma_\mu^{(k-1)}(x)\right) & x \in \Omega_{\rm qd}^{\rm eq} \end{cases} \tag{2.26}$$

for $k = 1, 2, \ldots, N_{\rm t}$. Note that the Galerkin ROM does not involve the definition of a reduced space for the internal variables, which are computed exclusively in the sampled quadrature points $\Omega_{\rm qd}^{\rm eq}$.

Some comments are in order.

- Concerning hyper-reduction, in [TT8], we exploited the analysis in [101] to determine the sparse representation problem and then, following [32], we solved a non-negative least-square problem to find the quadrature rule.

- The POD-Greedy method was first proposed in [39] and combines a greedy search to effectively explore the parameter domain with POD to compress the solution trajectory for each selected parameter value. For temporal compression, in [TT8] we compared the hierarchical POD (cf. [38, section 3.5]) with the hierarchical approximate POD (HAPOD) method analyzed in [45]: both approaches are designed to avoid the storage of the solution trajectory for all selected parameter values. Furthermore, we relied on a time-averaged error indicator — that exploits the previous works in [TT7, TT12] — to drive the greedy search.

In [TT2], we extended the method of [TT8] to three-dimensional problems and we integrated the PMOR procedure in the open-source software code_aster. The work in [TT2] represents one of the very first applications of PMOR in code_aster. In [TT2], we focused on problems of the form

$$\begin{cases} \mathfrak{R}_\mu^{\rm hf}(\sigma_\mu^{(k)}, v; \mu) = 0 & \forall\, v \in \mathcal{X}_{\rm hf}, \\[1em] \sigma_\mu^{(k)}(x) = \mathfrak{F}_\mu^{\rm hf}\left(\nabla u_\mu^{(k)}(x), \sigma_\mu^{(k-1)}(x)\right) & x \in \Omega_{\rm qd}, \end{cases} \tag{2.27}$$

where u_μ is the displacement field and σ_μ is the stress tensor; for problems of the form (2.27), we developed a specialized residual indicator based on Gappy-POD [31].

2.2.2 Numerical results

In [TT8] we considered a two-dimensional THM problem, which models the long-term ($\approx \mathcal{O}(100)$ years) behavior of the geological site surrounding radioactive waste which is placed inside repositories (dubbed *alveoli*) located deep underground; the model was chosen based on discussions with the researchers Antoine Pasteau and Marc Leconte from ANDRA. I refer to [TT8] and to the PhD thesis [86, Chapter 3] for a thorough presentation of the physical model; the model comprises four state variables (solid displacement, water pressure and temperature) and four internal variables. In the numerical experiments, we considered the sensitivity with respect to four parameters associated with the constitutive laws (cf. [TT8, section 4.5]): we considered variations of ±15% with respect to the nominal value.

Figure 2.1 summarizes the key results of [TT8]. Figure 2.1(a) shows the geometry considered in the numerical simulations: the red bars at the bottom of the domain indicate the alveoli, which are modelled as boundary conditions for the temperature (energy) equation; the three horizontal regions (USC, UT, UA) indicate three different regions of the geological medium, which are characterized by different material properties. Figure 2.1(b) shows the behavior of the temperature difference between final and initial configuration for the nominal value of the parameters; Figure 2.1(c) shows the out-of-sample discrete $L^2(\mathtt{I}; \mathcal{X})$ relative prediction error as a function of the number n of retained modes, for three iterations of the POD-Greedy algorithm with HAPOD temporal compression based on the time-averaged error indicator ("POD-Greedy") and on the true error ("strong-Greedy"). We observe that the proposed error indicator is as effective as the true error to drive the greedy strategy.

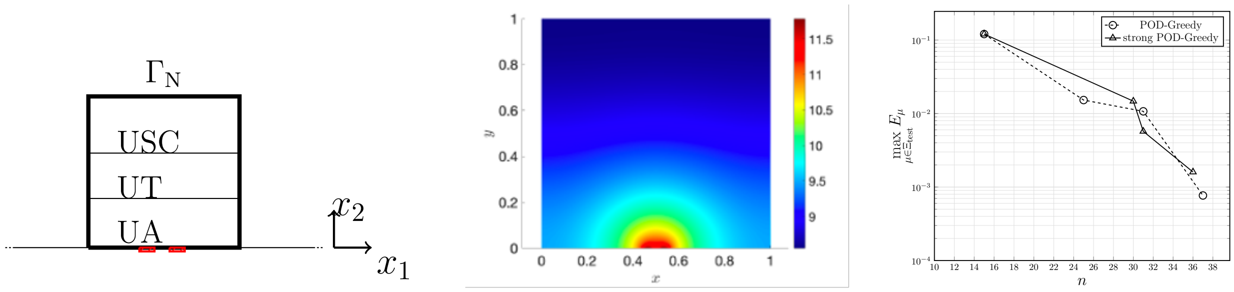

(a) (b) $T_\mu(t_{\rm f}) - T_\mu(0)$ (c) HA-POD Greedy

Figure 2.1: model reduction of THM systems. (a) system configuration. (b) temperature difference between final and initial configuration. (c) out-of-sample discrete $L^2(\mathtt{I}; \mathcal{X})$ relative prediction error for three iterations of the POD-Greedy algorithm with HAPOD temporal compression.

In [TT2], we studied the performance of the hyper-reduced Galerkin ROM for a three-dimensional plate with a circular hole subject to a tension force; we assumed that the total deformation is the sum of a plastic part and an elastic part, and we relied on the Von Mises criterion for isotropic hardening to model the plastic deformation. We studied variations with respect to two parameters associated with the constitutive law: the Poisson's ratio ν and the strain hardening coefficient $a_{\rm pui}$ associated with the strain hardening curve.

Figure 2.2 summarizes the key results of [TT2]. Figure 2.2(a) shows a section of the computational domain; Figure 2.2(b) shows the parameter domain and indicates the parameters of the training set used for the greedy algorithm; Figures 2.2(c)-(d) show the behavior of the residual indicator $\Delta_{n,\mu}$ which is used to drive the greedy search and the relative discrete $L^2(\mathtt{I};\mathcal{X})$ prediction error between the HF solution and the reduced solution. We observe that for this model problem the convergence is extremely fast. We obtain speedups of the order 20 with $n = \mathcal{O}(20)$ modes (cf. [TT2]) with respect to the HF industrial code.

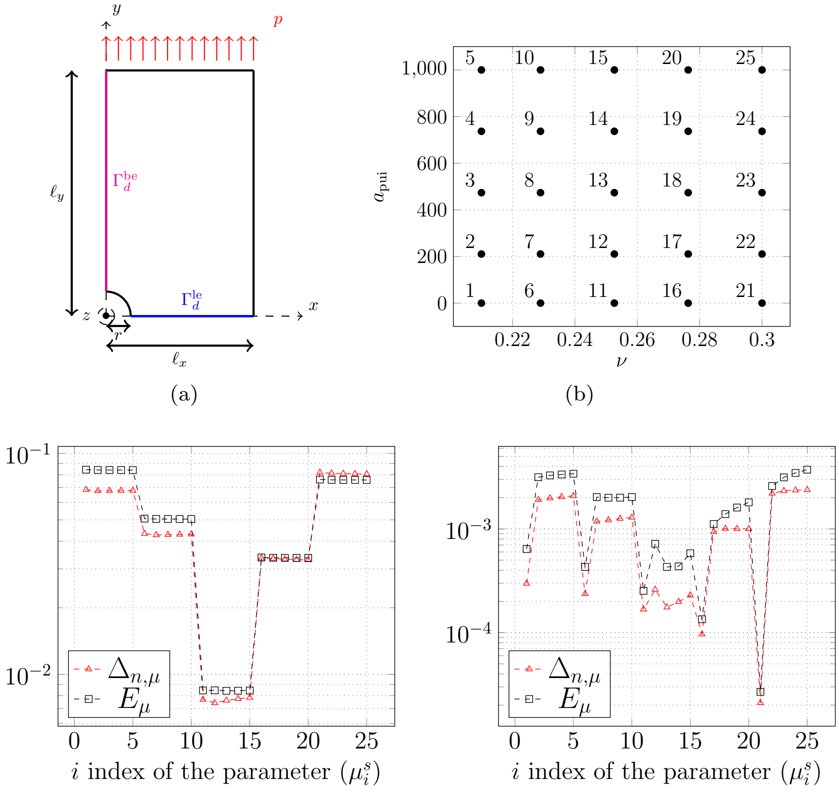

(a)

(b)

(c) it = 1

(d) it = 2

Figure 2.2: model reduction of nonlinear three-dimensional elastoplasticity. (a) system configuration. (b) training set $\mathcal{P}_{\rm train}$ used in the POD-Greedy algorithm. (c)-(d) behavior of the residual-based error indicator $\Delta_{n,\mu}$ and of the relative $L^2(\mathtt{I};\mathcal{X})$ state estimation error E_μ for the first two iterations of the greedy procedure.

2.3 Stabilized Galerkin ROMs for turbulent flows

During my postdoc at Sorbonne University, I developed a Galerkin ROM for parameterized incompressible turbulent flows [TT7]. The key features of the approach are threefold: (i) a constrained Galerkin formulation with box constraints for the computation of the reduced-order solution, (ii) a time-averaged *a posteriori* indicator for the error in the prediction of the mean flow, and (iii) a POD-Greedy strategy for the construction of the reduced space informed by the above-mentioned *a posteriori* indicator. The work in [TT7] provided the foundations for a 2018 NEUP (Nuclear Energy University program) project on MOR of turbulent thermal flows (PI: Prof. Paul Fischer), which enabled the extension to three-dimensional problems [51, 93]. In this manuscript, I present the constrained formulation; I refer to [TT7] for a detailed presentation of the other features of the approach.

2.3.1 Model problem

I consider the unsteady incompressible Navier-Stokes equations for high-Reynolds number flows with no-slip boundary conditions:

$$\begin{cases} \partial_t u + (u\cdot\nabla)u - \frac{1}{\rm Re}\Delta u + \nabla p = f & \text{in}\,\Omega\times\mathbb{R}_+, \\ \nabla\cdot u = 0 & \text{in}\,\Omega\times\mathbb{R}_+, \\ u = g & \text{on}\,\partial\Omega\times\mathbb{R}_+, \\ u = u_0 & \text{on}\,\Omega\times\{0\}, \end{cases} \tag{2.28}$$

where $\Omega \subset \mathbb{R}^d$, and f, g, u_0 are suitable fields, and $\mathrm{Re} > 0$ is the Reynolds number. In [TT7], we consider the lid-driven cavity flow with $\Omega = (-1,1)^2$, $f = 0$, $g = [(1-x_1^2)^2, 0]$ on $\Gamma_{\mathrm{top}} = \{x \in \partial\Omega : x_2 = 1\}$ and $g = 0$ on $\partial\Omega \setminus \Gamma_{\mathrm{top}}$. For sufficiently large values of the Reynolds number, the solution to (2.28) exhibits a chaotic behavior (cf. [17]); the goal of numerical simulations is hence to predict relevant time-averaged quantities of interest such as the long-time averaged velocity field and the turbulent kinetic energy (TKE).

We resort to a $\mathbb{Q}_M - \mathbb{Q}_{M-2}$ spectral element ([74]) discretization in space, and to an explicit three-step Adams-Bashforth (AB3)/ implicit two-step Adams-Moulton (AM2) discretization in time. HF simulations are performed using the open-source software `nek5000` ([34]). We set $M = 8$, we consider a 16 by 16 structured quadrilateral mesh and we consider an equispaced time grid $\{t_{\mathrm{g}}^j = j\Delta t\}_{j=0}^J$, with[2] $\Delta t = 2 \cdot 10^{-3}$. We estimate the long-time averaged velocity field as

$$\langle u \rangle_{\mathrm{g}} = \frac{\Delta t}{T - T_0} \sum_{j=J_0+1}^{J} u(t_{\mathrm{g}}^j), \tag{2.29}$$

where $T_0 = t_{\mathrm{g}}^{J_0} = 500$, $T = t_{\mathrm{g}}^J = 1000$. Consequently, we estimate the instantaneous turbulent kinetic energy as

$$\mathrm{TKE}(t_{\mathrm{g}}^j) := \frac{1}{2} \int_\Omega \| u(t_{\mathrm{g}}^j) - \langle u \rangle_{\mathrm{g}} \|_2^2 \, dx. \tag{2.30}$$

In order to generate (and, later, assess) the ROM, we collect data at the sampling times $\{t_{\mathrm{s}}^k = T_0 + \Delta t_{\mathrm{s}} k\}_{k=1}^K$ with $\Delta t_{\mathrm{s}} = 1$. Note that, due to memory constraints, $\{t_{\mathrm{s}}^k\}_{k=1}^K \subset \{t_{\mathrm{g}}^j\}_{j=J_0}^J$, and $K \ll J$. We do not collect data in the transient region: this is motivated by the fact that we are here ultimately interested in the long-time dynamics. In the remainder of this section, I use the subscript "s" to indicate the sampling times, and the subscript "g" to indicate the time discretization. Furthermore, the symbol $\langle \cdot \rangle_{\mathrm{s}}$ indicates time averages performed based on the sampling times, and the symbol $\langle \cdot \rangle_{\mathrm{g}}$ denotes time averages performed based on the time grid $\{t_{\mathrm{g}}^j\}_{j=J_0}^J$. In particular, I define the truth estimate of the mean TKE as

$$\langle \mathrm{TKE} \rangle_{\mathrm{s}} = \frac{1}{2K} \sum_{k=1}^{K} \| u(t_{\mathrm{s}}^k) - \langle u \rangle_{\mathrm{g}} \|_{L^2(\Omega)}^2. \tag{2.31}$$

2.3.2 Methodology

We consider a velocity-only ROM. We denote by $\bar{u}$ the discrete solution to the Stokes equations with boundary datum g (cf. (2.28)); then, we consider the affine ansatz

$$\widehat{u}(t) = Z\widehat{\boldsymbol{\alpha}}(t) = \bar{u} + \sum_{i=1}^{n} \left(\widehat{\boldsymbol{\alpha}}(t) \right)_i \zeta_i, \tag{2.32}$$

where $\{\zeta_i\}_{i=1}^n$ are obtained by applying POD to the lifted snapshots $\{u(t_{\mathrm{s}}^{\mathrm{k}}) - \bar{u}\}_{k=1}^K$ based on the H^1 inner product. Note that the ansatz (2.32) satisfies the continuity equation and the boundary conditions for any $\boldsymbol{\alpha} \in \mathbb{R}^n$.

If we employ a semi-implicit time discretization, we obtain the discrete Galerkin ROM (to shorten notation, we set $\widehat{u}^j = \widehat{u}(t_{\mathrm{g}}^j)$):

$$\frac{1}{\Delta t} \int_\Omega (\widehat{u}^{j+1} - \widehat{u}^j) \cdot v \, dx + \int_\Omega \frac{1}{\mathrm{Re}} \nabla \widehat{u}^{j+1} : \nabla v + (\widehat{u}^j \cdot \nabla)\widehat{u}^{j+1} \cdot v \, dx = 0 \quad \forall\, v \in \mathcal{Z} = \mathrm{span}\{\zeta_i\}_{i=1}^n, \tag{2.33}$$

for $j = 1, 2, \ldots, J-1$. The Galerkin ROM (2.33) can be written in the following algebraic form

$$\mathbf{A}(\widehat{\boldsymbol{\alpha}}^j)\widehat{\boldsymbol{\alpha}}^{j+1} = \mathbf{F}(\widehat{\boldsymbol{\alpha}}^j), \quad \forall\, j = 1, 2, \ldots, J-1, \tag{2.34}$$

for proper choices of the matrix-valued function $\mathbf{A} : \mathbb{R}^n \to \mathbb{R}^{n \times n}$ and $\mathbf{F} : \mathbb{R}^n \to \mathbb{R}^n$.

The constrained formulation stems from the observation that in Galerkin ROMs the HF data are only used to build the POD basis; instead, we propose to further use the snapshot set to infer bounds for the generalized coordinates. Towards this end, we define

$$m_i^{\mathrm{u}} = \min_k \, (u(t_{\mathrm{s}}^{\mathrm{k}}) - \bar{u}, \zeta_i)_{H^1}, \quad M_i^{\mathrm{u}} = \max_k \, (u(t_{\mathrm{s}}^{\mathrm{k}}) - \bar{u}, \zeta_i)_{H^1}, \quad i = 1, \ldots, n \tag{2.35a}$$

and then we introduce the bounds for the generalized coordinates

$$\alpha_i^{\mathrm{LB}} := m_i^{\mathrm{u}} - \epsilon \left(M_i^{\mathrm{u}} - m_i^{\mathrm{u}} \right), \qquad \alpha_i^{\mathrm{UB}} := m_i^{\mathrm{u}} + \epsilon \left(M_i^{\mathrm{u}} - m_i^{\mathrm{u}} \right), \quad i = 1, \ldots, n; \tag{2.35b}$$

---

[2] The time step is required to ensure stability of the run and maintain CFL $\sim 0.5 - 0.6$.

where $\epsilon > 0$ takes into account the fact that the sample minima and the sample maxima associated with the snapshots $\{u(t_{\rm s}^{\rm k})\}_{k=1}^K$ are upper and lower bounds for the true minima and true maxima, respectively.

In conclusion, we obtain the formulation

$$\widehat{\boldsymbol{\alpha}}^{j+1} := \arg \min_{\boldsymbol{\alpha} \in \mathbb{R}^n} \| \mathbf{A}(\widehat{\boldsymbol{\alpha}}^j) \boldsymbol{\alpha} - \mathbf{F}(\widehat{\boldsymbol{\alpha}}^j) \|_2^2, \quad \text{s.t. } \alpha_i^{\rm LB} \le \alpha_i \le \alpha_i^{\rm UB}, \ \ i = 1, \ldots, n, \tag{2.36}$$

which reads as a quadratic programming problem and can be solved efficiently using interior point methods. We observe that $\widehat{\boldsymbol{\alpha}}^{j+1}$ coincides with the solution to the Galerkin ROM (2.34) if the latter satisfies the box constraints of (2.36). It can be shown that there exists $\Delta t^\star > 0$ and $C > 0$ such that for all $\Delta t < \Delta t^\star$, we have $\|\widehat{\boldsymbol{\alpha}}^{j+1} - \widehat{\boldsymbol{\alpha}}^j\|_2 \le C \Delta t$ (cf. [TT7, Appendix D]): this implies that the sequence $\{\widehat{\boldsymbol{\alpha}}^j\}_j$ interpolates a C-Lipschitz function $\widehat{\boldsymbol{\alpha}}^\infty : (0, T) \to \mathbb{R}^n$.

2.3.3 Numerical results

Figure 2.3 shows the performance of the POD-Galerkin ROM for Re = 15000. Figure 2.3 (a) shows the relative L^2 and H^1 errors in mean flow prediction for several values of the ROB size n; Figure 2.3 (b) compares the prediction of the mean TKE with the truth estimate (2.31); finally, Figures 2.3 (c)-(d)-(e) show the temporal behavior of the TKE for the ROM and for the HF model. I observe that the Galerkin ROM is extremely inaccurate for small values of n: I observe both false steady-state solutions and significant overestimations of the TKE. Interestingly, the behavior of the ROM observed here is qualitatively similar to the one observed for highly-truncated spectral approximations to turbulent flows [24].

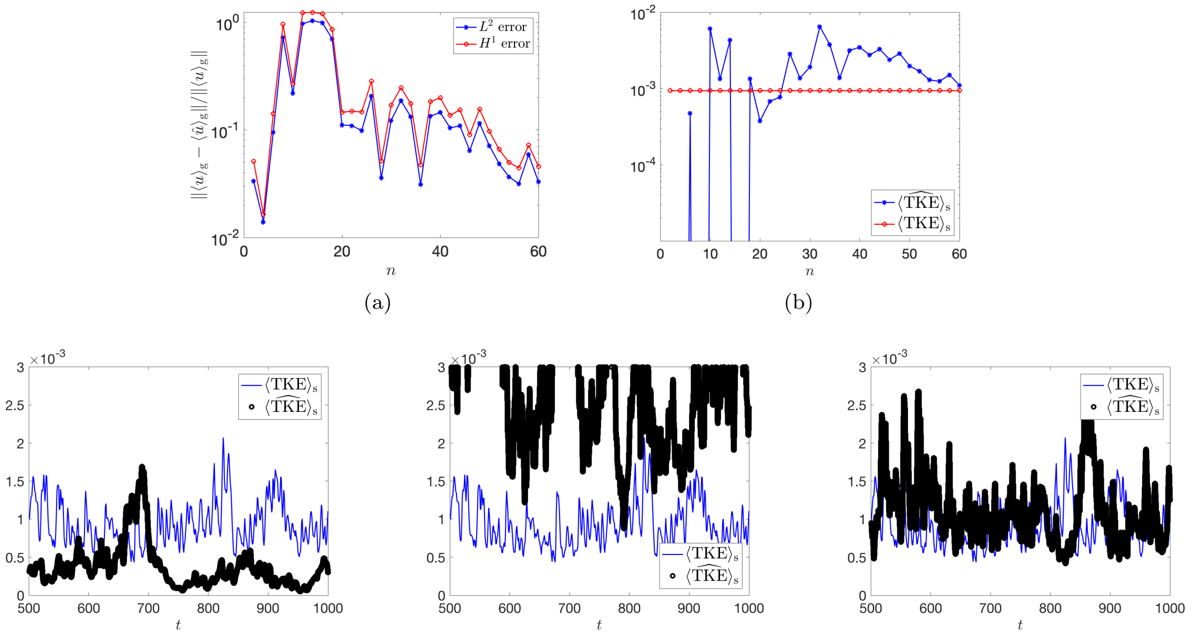

(a)

(b)

(c) $n = 20$

(d) $n = 40$

(e) $n = 60$

Figure 2.3: model reduction of turbulent flows. Performance of POD-Galerkin ROM for Re = 15000. (a) relative L^2 and H^1 errors in mean flow prediction with n. (b) TKE prediction $\widehat{\langle \rm TKE\rangle}_{\rm s}$ vs. truth estimate (2.31) for multiple values of n. (c)-(d)-(e) TKE temporal prediction for three values of n.

Figure 2.4 replicates the results of Figure 2.3 for the constrained Galerkin ROM for Re = 15000, for $\epsilon = 0.01$ (cf. (2.35)). The constrained formulation leads to a substantial improvement in performance compared to the standard POD-Galerkin method (cf. Figures 2.3(b) and 2.3(c)): for $n \gtrsim 40$ the relative error in the mean is less than 2%, while the predicted mean TKE is bounded from above by $\langle \rm TKE\rangle_{\rm s}$ for all values of n. Furthermore, the TKE of the constrained Galerkin formulation is larger than the one predicted by the Galerkin ROM for certain values of n, and is smaller for other values of n: this empirically proves that the approach does not necessarily add dissipation to the Galerkin ROM. This is in contrast with POD closure models, which effectively add dissipation to the reduced system. Finally, I observe a distinctly non-monotonic behavior around $n = 18$, which corresponds to a change in the temporal dynamics of the reduced system from chaotic ($n = 18$) to quasi-periodic ($n = 20$): since for $n \approx 20$ the flow is still extremely under-resolved, the constrained ROM does not provide a stable (with respect to n) representation of the dynamics.

Figure 2.5 illustrates the sensitivity with respect to the choice of the hyper-parameter ϵ in (2.35). In more detail, Figure 2.5 shows (a) the behavior of the relative error in mean flow prediction, (b) the TKE prediction

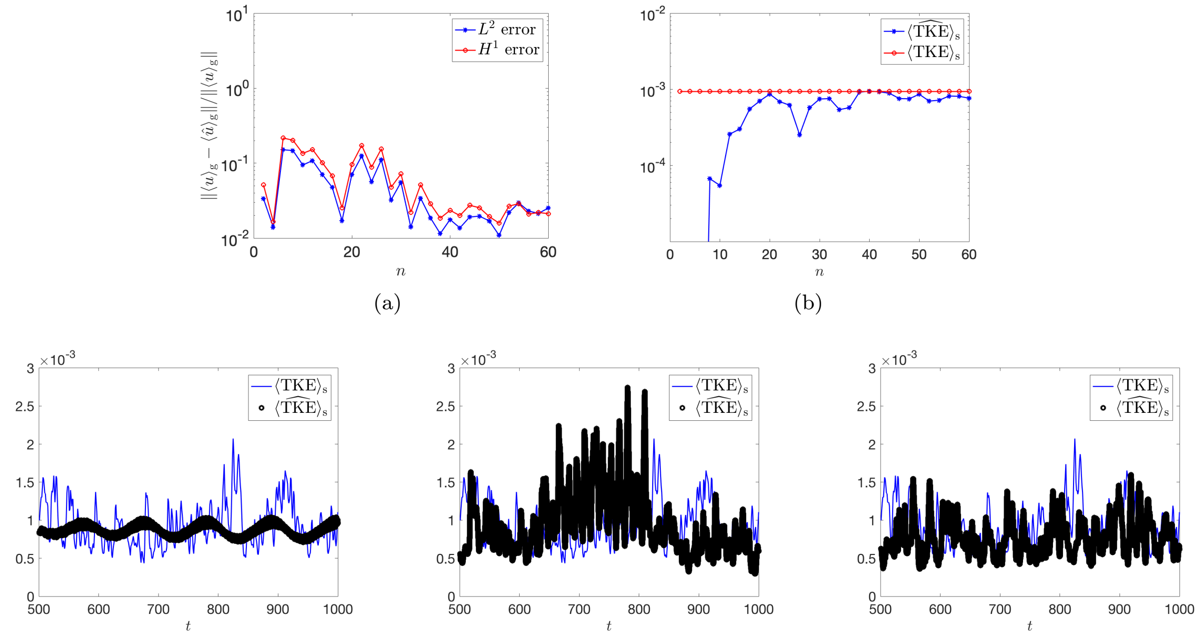

(a)

(b)

(c) $n = 20$

(d) $n = 40$

(e) $n = 60$

Figure 2.4: model reduction of turbulent flows. Performance of constrained POD-Galerkin ROM for Re = 15000. (a) relative L^2 and H^1 errors in mean flow prediction with n. (b) TKE prediction $\langle \widehat{\mathrm{TKE}}\rangle_{\rm s}$ vs. truth estimate (2.31) for multiple values of n. (c)-(d)-(e) TKE temporal prediction for three values of n.

and (c) the fraction of pure Galerkin solves

$$\#\mathrm{Gal} := \frac{1}{J - J_0} \sum_{j=J_0+1}^{J} \mathbb{1}\left(\boldsymbol{\alpha}_{\rm gal}^j \in [\boldsymbol{\alpha}^{\rm LB}, \boldsymbol{\alpha}^{\rm UB}] \right),$$

where $\boldsymbol{\alpha}_{\rm gal}^j$ corresponds to the Galerkin solution at time $t_{\rm g}^j$, for two values of n. Figure 2.5(a) shows that results are insensitive to the choice of ϵ for $\epsilon \lesssim 0.1$. I further observe that for all values of ϵ considered $\#\mathrm{Gal}(n = 40) \gtrsim 0.85$ and $\#\mathrm{Gal}(n = 60) \gtrsim 0.90$: our constrained formulation hence corrects the original formulation only for $10 - 15\%$ time steps. For this reason, I envision that efficient implementations of the constrained ROM might be nearly as inexpensive as the Galerkin ROM[3]. I further observe that #Gal increases as n increases: this can be explained by observing that the POD-Galerkin ROM becomes more and more accurate as n increases, and thus requires less corrections.

2.4 Treatment of parameterized geometries

The offline-online framework of Algorithm 1 relies on the assumption that the problem of interest is defined over a parameter-independent configuration Ω. Handling of geometric parameters requires the introduction of a reference domain Ω and a parametric mapping $\Phi_\mu : \Omega \to \Omega_\mu$ to recast the problem over a parameter-independent configuration. In [TT17], together with Lei Zhang, I developed and analyzed a general strategy to handle parameterized geometries in PMOR: the work provided the foundations for the integration of the registration techniques reviewed in Chapter 3 in the offline-online framework of Algorithm 1.

2.4.1 Methodology

We might distinguish between two approaches to deal with parameterized geometries: the Map-then-Discretize (MtD, [7, 55, 81, 82]) approach and the Discretize-then-Map (DtM, [26, 96] and [TT17]) approach. To clarify the differences between the two approaches, I consider the continuous FE discretization of the Laplace equation with homogeneous boundary conditions:

$$\begin{cases} -\Delta u_\mu = f_\mu & \text{in } \Omega_\mu, \\ u_\mu = 0 & \text{on } \partial\Omega_\mu. \end{cases} \tag{2.37}$$

---

[3] For $n = 60$, our implementation of the constrained formulation was found six times more expensive than the Galerkin ROM (cf. [TT7, Appendix H]).

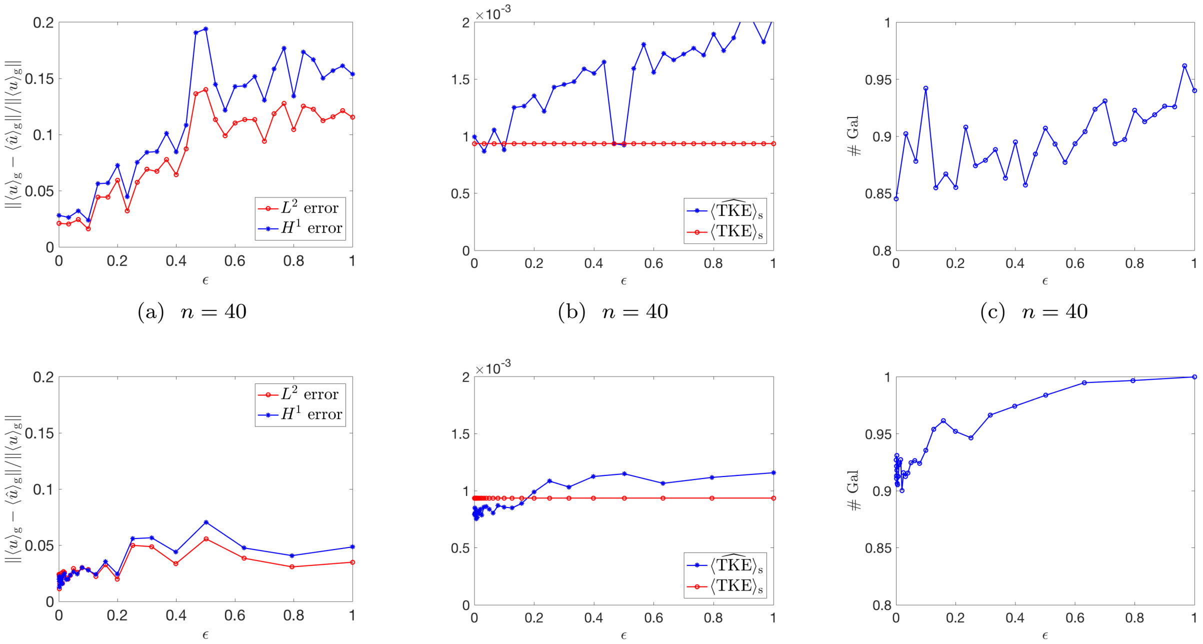

(a) $n = 40$ (b) $n = 40$ (c) $n = 40$

(d) $n = 60$ (e) $n = 60$ (f) $n = 60$

Figure 2.5: model reduction of turbulent flows. Sensitivity with respect to ϵ of constrained POD-Galerkin ROM for Re $= 15000$ and two values of n. (a) - (d): behavior of the relative L^2 and H^1 errors. (b) - (e): TKE prediction $\widehat{\langle \mathrm{TKE}\rangle}_{\mathrm{s}}$ vs. truth estimate (2.31). (c) - (f): fraction of pure Galerkin solves.

The point of departure of the MtD approach is the weak formulation of the mapped problem (2.37): find $\widetilde{u}_\mu = u_\mu \circ \Phi_\mu \in H_0^1(\Omega)$ such that

$$\int_\Omega \left(K_\mu \nabla \widetilde{u}_\mu \cdot \nabla v \, - \, \widetilde{f}_\mu v \right) dx \, = \, 0 \quad \forall \, v \in H_0^1(\Omega), \tag{2.38}$$

where $K_\mu = \det(\nabla \Phi_\mu) \, \nabla \Phi_\mu^{-1} \nabla \Phi_\mu^{-\top}$ and $\widetilde{f}_\mu = \det(\nabla \Phi_\mu) \, f_\mu \circ \Phi_\mu$. Then, the FE discretization of (2.38) is introduced: given the FE space $\mathcal{X}_{\mathrm{hf}} \subset H_0^1(\Omega)$, find $\widetilde{u}_\mu^{\mathrm{hf}} \in \mathcal{X}_{\mathrm{hf}}$ such that

$$\mathfrak{R}_\mu^{\mathrm{mtd}}(\widetilde{u}_\mu^{\mathrm{hf}}, v) = \sum_{k=1}^{N_{\mathrm{e}}} \underbrace{\int_{\mathtt{D}_k} \left(K_\mu \nabla \widetilde{u}_\mu^{\mathrm{hf}} \cdot \nabla v \, - \, \widetilde{f}_\mu v \right) dx}_{=: \mathfrak{r}_\mu^{\mathrm{mtd}}(E_k \widetilde{u}_\mu^{\mathrm{hf}}, E_k v; \mathtt{X}_k^{\mathrm{hf}})} \, = \, 0 \quad \forall \, v \in \mathcal{X}_{\mathrm{hf}}. \tag{2.39}$$

Note that the local operator $\mathfrak{r}_\mu^{\mathrm{mtd}}$ associated with the k-th element of the mesh depends on the local solution field and on the local mesh nodes $\mathtt{X}_k^{\mathrm{hf}}$. PMOR techniques are then applied to the discretized mapped problem (2.39).

In the DtM approach, given the mesh $\mathcal{T}_{\mathrm{hf}}$ of Ω, we introduce the deformed mesh $\Phi_\mu(\mathcal{T}_{\mathrm{hf}})$ with elements (see (2.3))

$$\mathtt{D}_{k,\mu} = \left\{ \Psi_{k,\mu}^{\mathrm{fe}}(\tilde{x}) = \sum_{i=1}^{n_{\mathrm{lp}}} \Phi_\mu(x_{\mathtt{T}_{k,i}}^{\mathrm{hf}}) \ell_i(\tilde{x}) : \tilde{x} \in \widehat{\mathtt{D}} \right\}, \quad k = 1, \ldots, N_{\mathrm{e}},$$

and the corresponding FE space $\mathcal{X}_{\mathrm{hf},\mu}$; then, we introduce the FE discretization: find $u_\mu^{\mathrm{hf}} \in \mathcal{X}_{\mathrm{hf},\mu}$ such that

$$\mathfrak{R}_\mu^{\mathrm{dtm}}(u_\mu^{\mathrm{hf}}, v) = \sum_{k=1}^{N_{\mathrm{e}}} \int_{\mathtt{D}_{k,\mu}} \left(\nabla u_\mu^{\mathrm{hf}} \cdot \nabla v \, - \, f_\mu v \right) dx \, = \, \sum_{k=1}^{N_{\mathrm{e}}} \mathfrak{r}_\mu^{\mathrm{dtm}}(E_k u_\mu^{\mathrm{hf}}, E_k v; \Phi_\mu(\mathtt{X}_k^{\mathrm{hf}})) \, = \, 0 \quad \forall \, v \in \mathcal{X}_{\mathrm{hf},\mu}. \tag{2.40}$$

Finally, we apply PMOR to (2.40).

In [TT17], together with Zhang, I present an extended comparison of the two approaches.

- MtD and DtM are equivalent if $\Psi_{k,\mu}^{\mathrm{fe}} = \Phi_\mu \circ \Psi_k^{\mathrm{fe}}$ for $k = 1, \ldots, N_{\mathrm{e}}$. A sufficient condition is that the maps $\{\Phi_\mu \circ \Psi_k^{\mathrm{fe}}\}_k$ are all polynomials of degree at most $\mathtt{p}$.
- MtD relies on the assumption that the mapping Φ_μ is bijective from Ω to Ω_μ; on the other hand, DtM requires that Φ_μ is such that the deformed mesh $\Phi_\mu(\mathcal{T}_{\mathrm{hf}})$ is a proper mesh of Ω_μ, that is the local FE maps

$\{\Psi^{\rm fe}_{k,\mu}\}_k$ are all bijective. In [TT17], we refer to the latter condition as *discrete bijectivity* to emphasize the fact that the property depends on the particular mesh that is used in the HF discretization. Bijectivity and discrete bijectivity are two independent properties of the mapping Φ in the sense that the former is neither sufficient nor necessary for the latter.

- In the MtD approach, the FE discretization is applied to the mapped problem (2.38); therefore, the convergence rate depends on the smoothness of $u_\mu \circ \Phi_\mu$. For high-order discretizations, it is hence necessary to consider smooth maps. On the other hand, in the DtM approach, the FE model (2.40) is a discretization of (2.37) in the deformed domain: therefore, convergence rates do not explicitly depend on the smoothness of the map.

- Since in the MtD framework PMOR is applied to the mapped problem (2.38), any hyper-reduction technique for parametric problems in fixed domains can be employed. In particular, in (2.39), we can resort to the empirical interpolation method (EIM, [11]) to determine parametrically-affine approximations of the parametric fields $K_\mu, \tilde{f}_\mu$. On the other hand, in the DtM framework, hyper-reduction should be applied to the discrete formulation: this implies that techniques based on the definition of a reduced integration domain (*mesh sampling*) are much more readily applicable than techniques based on the approximation of the differential operator such as EIM[4].

- MtD requires the evaluation of the derivatives of the mapping Φ_μ, which might not be available. On the other hand, the DtM approach — if combined with mesh-sampling techniques — simply requires the evaluation of the mapping Φ_μ to deform the nodes of the reduced mesh; furthermore, DtM enables the use of standard FE local integration routines and is thus considerably easier to implement.

Figure 2.6(a) illustrates the different convergence rates of the MtD and DtM approaches obtained for the Laplace problem

$$-\partial_{xx} u = \sin(\pi x) \quad x \in \Omega = (0,1), \quad u(0) = u(1) = 0, \tag{2.41a}$$

when the mapping

$$\Phi(x) = \begin{cases} \dfrac{1}{2} x & x \leq x_0, \\ \dfrac{1}{2}\left(x_0 + \dfrac{2 - x_0}{1 - x_0}(x - x_0) \right) & x \geq x_0; \end{cases} \qquad x_0 = \frac{1}{\sqrt{2}}, \tag{2.41b}$$

is applied. Clearly, Φ is a Lipschitz map from Ω in itself. I denote by $\mathcal{T}_{\rm hf}$ an uniform FE grid of Ω with $N_{\rm e}$ elements. Piecewise-smooth maps are broadly used in PMOR to model geometric deformations (see, e.g., [82] and the example of the next section). In Figure 2.6(a), I show the behavior of the L^2 error associated with three FE discretizations: a P3 isoparametric FE discretization of the problem associated with $\Phi(\mathcal{T}_{\rm hf})$ (`P3 DtM`); a P1 (for the mapping) P3 (for the state) subparametric FE discretization of the problem associated with $\Phi(\mathcal{T}_{\rm hf})$ (`P1-P3 DtM`); a P3 FE discretization of the mapped problem associated with $\mathcal{T}_{\rm hf}$ (`P3 MtD`). The MtD approach fails to recover the optimal convergence rate ($r = 4$) due to quadrature error and due to the fact that the MtD approach approximates the mapped field $u \circ \Phi$, which is considerably less smooth than u. The isoparametric discretization suffers due to stability issues: even if Φ is bijective, the local map of the deformed mesh that contains x_0 is not necessarily bijective and thus the deformed mesh might have inverted elements. On the other hand, the subparametric DtM approach recovers the optimal convergence rate as expected from standard FE theory (e.g., [79, Proposition 3.4.1]).

For FE P1 discretizations of one-dimensional domains, $\Phi(\mathcal{T}_{\rm hf})$ is guaranteed to not have inverted elements; however, the same result does not hold in higher dimensions. Consider the element depicted in Figure 2.6(b), the dashed line denotes the boundary of the domain: we can construct a mapping Φ that maps the point A in the point B in the picture. The deformed element thus reduces to a straight line— which implies that the corresponding elemental mapping of the deformed mesh is not bijective. Note that for the MtD approach well-posedness depends on the fact that K_μ in (2.38) is positive definite: the latter is independent of the underlying mesh and thus follows from the bijectivity of Φ. Unlike MtD, the DtM approach might hence fail for smooth but large deformations, particularly in the presence of anisotropic elements.

2.4.2 Numerical results

I review the results in [TT17] for a two-dimensional flow past a parameterized Ahmed body [1, 57], at moderate Reynolds number; a complete description of the model problem is provided in [TT17, Appendix A].

---

[4] I envision that continuous-based hyper-reduction techniques could also be applied in the DtM framework; however, their implementation is far more involved and, to the best of my knowledge, it has never been considered in the MOR literature.

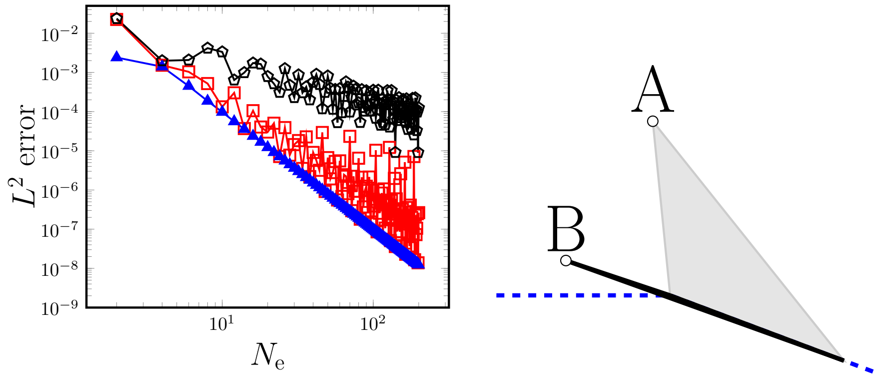

(a) (b)

Figure 2.6: optimal convergence and discrete bijectivity. (a) performance of three FE discretizations for a Laplace problem. Isoparametric P3 DtM —□—; subparametric P1-P3 DtM —▲—, P3 MtD —⬠—. (b) failure of the discretize-then-map approach for large deformations. The bijection Φ maps the point A in B; under this deformation, the select element (in gray) of the mesh reduces to a straight line; the deformed mesh is hence singular.

- We consider the incompressible Reynolds-averaged Navier-Stokes (RANS) equations with Spalart-Allmaras closure model (see [90, 2]). The geometry of the body is prescribed in Figure 2.7(a). The problem is parameterized with respect to the slant angle μ: we consider angles between 5^o and 50^o degrees, $\mathcal{P} = [5, 50]$. Reynolds number is defined as the ratio between horizontal inflow velocity times the height H_{c} of the body divided by kinematic viscosity; we consider $Re = 3 \cdot 10^3$. Figure 2.8 shows the behavior of the horizontal velocity for $\mu = 25^o$ and the behavior of the horizontal velocity profile for $x_1 = 1.1$ and $x_2 \in [0, 0.4]$ for three choices of the angle μ.

- To determine the geometric mapping, we partition the domain Ω_μ into the seven regions $\{\Omega_{i,\mu}\}_{i=1}^7$ depicted in Figure 2.7(b); then, we define parameterized Gordon-Hall maps in each of the seven regions. Note that Φ is the identity in the regions $1, 2, 6, 7$. I refer to [TT17, section 3.4] for the explicit expression of the mapping. Note that the mapping is a Lipschitz function with discontinuous derivatives.

- We discretize the problem using a streamline-upwind Petrov–Galerkin (SUPG) FE method, [91, 92] with pressure-stabilized Petrov-Galerkin (PSPG) term to eliminate spurious modes in the pressure solution when considering the same polynomial order for pressure and velocity; furthermore, we consider the least-squares incompressibility constraint (LSIC) stabilization term to improve accuracy and conditioning of the discrete problem, [35, 36, 16]. To compute the HF solution, we resort to a pseudo-transient continuation [53] procedure to solve the discrete nonlinear problem. Figure 2.7(b) shows the computational mesh used in the numerical experiments ($N_{\mathrm{e}} = 26602$): note that the mesh is not conforming with the coarse-grained partition that is used to define the geometric mapping.

The ROM relies on an affine ansatz for the state variables and on the LSPG formulation (2.20) to compute the generalized coordinates. We consider a single-field approximation to simultaneously approximate velocity, pressure and turbulent viscosity; we consider the affine ansatz (2.13) with $\bar{u}$ given by the flow for $\mu = 25^o$; the ROB Z is obtained using a POD of a dataset of $n_{\mathrm{train}} = 40$ snapshots in $\mathcal{P}$; the nonlinear least-square problem is solved using the Gauss-Newton method without line search with initial condition for the ROM chosen using nearest-neighbor regression; the test space $\mathcal{Y}_m$ is chosen using POD of a dataset of Riesz represents associated with the Fréchet derivative of the discrete residual (cf. section 2.1) with $m = \dim(\mathcal{Y}_m) = 2n$; hyper-reduction is performed using the mesh sampling and weighting (elementwise empirical quadrature) procedure of section 2.1. We assess performance based on $n_{\mathrm{test}} = 10$ randomly-selected out-of-sample parameters.

Figure 2.9(a) compares the average out-of-sample relative projection error with the average out-of-sample relative error E_{avg} for various choices of the size n of the reduced-order basis Z and for three different tolerances tol_{eq} for the empirical quadrature hyper-reduction procedure. I observe that the ROM guarantees near-optimal performance with respect to the projection error, for sufficiently tight tolerances. Figure 2.9(b) shows the percentage of sampled elements with respect to n for various tolerances: for all test cases considered, the number of sampled elements is less than 2% of the size N_{e} of the complete mesh. Speedups of the hyper-reduced ROM compared to the ROM with HF quadrature scale with the percentage of sampled elements and thus range from $\mathcal{O}(50)$ to $\mathcal{O}(300)$ for $n = 1, \ldots, 10$ and $tol_{\mathrm{eq}} = 10^{-10}$.

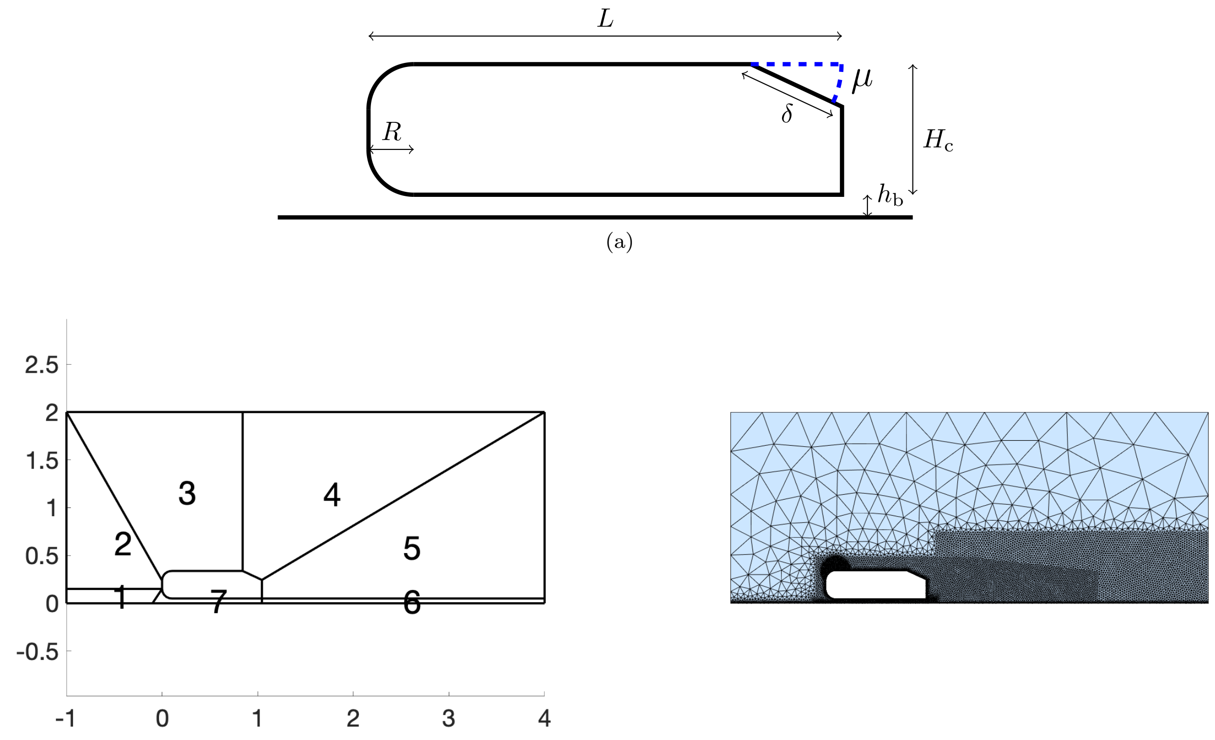

(a)

(b)

(c)

Figure 2.7: Ahmed's body. (a) description of the body geometry. (b) coarse-grained partition associated with Φ. (c) computational mesh. $L = 1.044$, $R = 0.1$, $h_\mathrm{b} = 0.05$, $H_\mathrm{c} = 0.288$, $\delta = 0.222$.

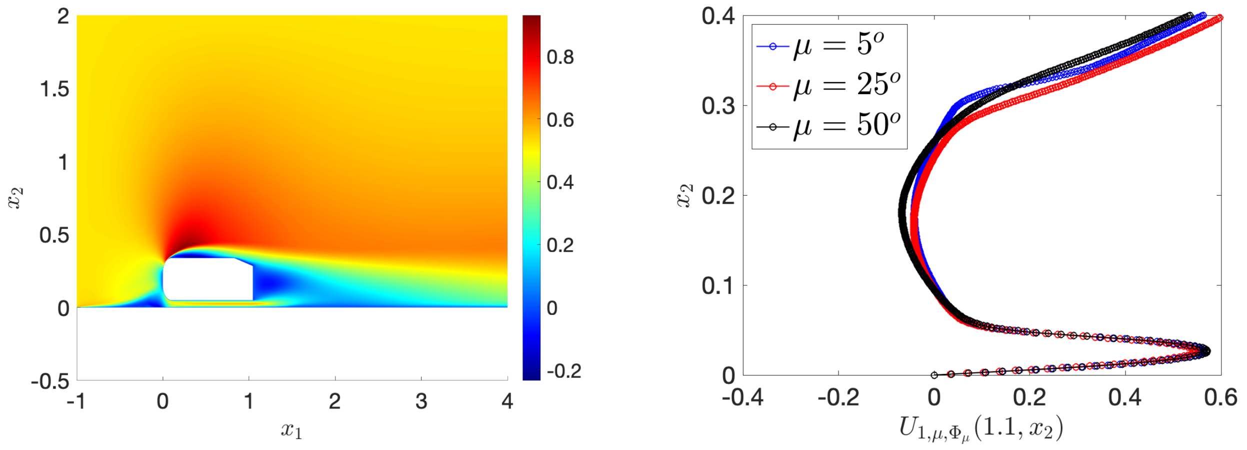

(a)

(b)

Figure 2.8: Ahmed's body. (a) behavior of the horizontal velocity for $\mu = 25^o$. (b) behavior of the horizontal velocity profile for $x_1 = 1.1$ and various x_2 for three choices of μ.

2.5 Research perspectives

Despite the many contributions to the field in the last two decades, the development of effective linear PMOR techniques for highly-nonlinear PDEs requires to address several fundamental challenges.

- *Extension to more complex engineering problems.* In the recent preprint [TT1], Agouzal extended the methodology developed in [TT2] to the simulation of the ageing of prestressed concrete structures. The problem involves the coupling of a three-dimensional mechanical model for the concrete with a one-dimensional model for the steel prestressing cables. The response of the three-dimensional material is modeled by a thermo-hydro-visco-elastic rheological model; the prestressing cables behave according to a one-dimensional linear thermo-elastic model. The numerical results further illustrate the ability of Galerkin ROMs — in combination with industrial-grade FE solvers — to estimate the parametric response of complex engineering systems.

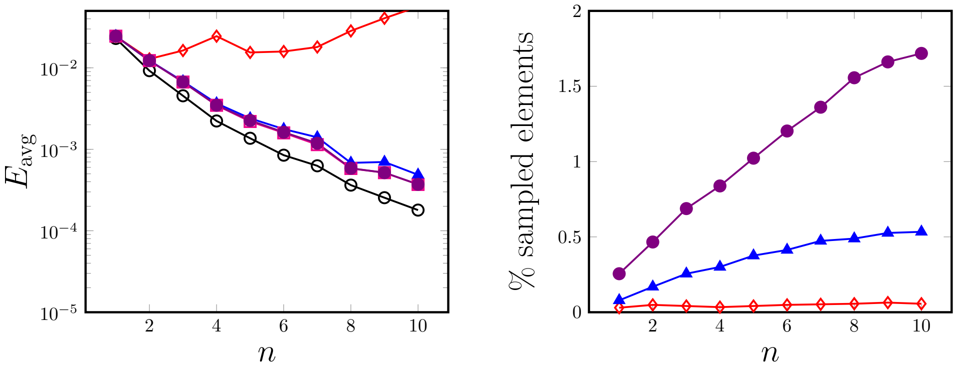

(a) (b)

Figure 2.9: Ahmed's body problem. Performance with respect to n and the EQ tolerance tol_{eq} ($m = 2n$). (a) average out-of-sample error E_{avg}: projection —○—, LSPG ROM with HF quadrature —□—, $tol_{\text{eq}} = 10^{-6}$ —◇—, $tol_{\text{eq}} = 10^{-10}$ —▲—, $tol_{\text{eq}} = 10^{-14}$ —●— (b) percentage of sampled elements for three choices of tol_{eq} (see (a)).

- *Incremental approaches.* For nonlinear and possibly unsteady problems, vanilla implementation of greedy strategies for ROM generation is expensive due to the need to construct the ROM and identify the new sampling parameter at each greedy iteration. In [TT3], together with Agouzal, I developed an incremental multi-fidelity approach to accelerate the construction of the ROM. Our approach exploits hierarchical approximate proper orthogonal decomposition to speed up the construction of the empirical test space for least-square Petrov-Galerkin formulations, a progressive construction of the empirical quadrature rule based on a warm start of the non-negative least-square algorithm, and a two-fidelity sampling strategy to reduce the number of expensive greedy iterations.

- *Choice of the test norm for LSPG formulations.* As discussed in section 2.1, the choice of the test norm plays a major role in the performance of LSPG ROMs. I collaborate with Charbel Farhat, Angelo Iollo, and Haysam Telib to investigate the impact of the choice of the norms in LSPG ROMs.

- *Application of PMOR to hydraulic flows.* In the industrial PhD project of Abdessamad Moussadak at EDF, in collaboration with Astrid Decoune, we plan to develop a projection-based ROM for the shallow water equations in the open-source software TELEMAC MASCARET (cf. [42]), for hydraulics applications. The project involves the treatment of wet-dry fronts that pose fundamental issues to the stability of ROMs; furthermore, we should also devise a ROM that copes with the underlying structure of the HF code, which is based on a two-step procedure for temporal discretization.

- *Stochastic closures for model reduction of turbulent flows.* As discussed in section 2.3, approximation of parametric turbulent flows is challenging due to the slow decay of the Kolmogorov n-width and due to the chaotic nature of the system dynamics. In the recently-funded ANR project RedLUM, following [80], I will investigate stochastic closure models of PROMs for incompressible turbulent flows: the distinctive feature of this approach is to approximate the deterministic chaotic dynamics through a system of stochastic ordinary differential equations for the dominant (high-energy) POD modes; the prediction of the solution is then obtained through a PROM ensemble forecast. The project is in collaboration with Valentin Resseguier, Dominique Heitz at Inrae Rennes, and with Giovanni Stabile at Sant'Anna School of Advanced Studies, and is scheduled to start in October 2024.

Chapter 3

Registration methods for model order reduction

Despite the many contributions to the field, MOR of advection-dominated PDEs remains a formidable task that requires major improvements of state-of-the-art procedures. First, linear-subspace MOR methods are fundamentally ill-suited to deal with parameter-dependent sharp gradients that naturally arise in the solutions to advection-dominated problems. Furthermore, traditional MOR methods rely on a single HF discretization to represent all the elements of the solution manifold: if parametric variations strongly affect the location of sharp-gradient regions, we are forced to refine the mesh over a vast portion of the computational domain, which leads to an HF discretization of intractable size. Effective MOR procedures for conservation laws should thus embed an effective parametric mesh adaptation (MA) strategy to track moving structures.

The provable inadequacy of linear or affine MOR approaches (cf. (2.13)) has motivated the development of several nonlinear approximation methods [3, 8, 56, 75]; a promising class of nonlinear approximations relies on coordinate transformations to track the location of coherent structures of the solution field and ultimately simplify the task of model reduction. The problem of finding the parametric mapping is referred to as *registration problem*.

Registration in MOR is tightly linked to the problem of non-rigid registration in image processing [46, 62]; in particular, point set registration (PSR, [63, 65, 71]) is the process of computing a spatial transformation that optimally aligns pairs of point sets. Registration is also linked to the implicit shock tracking method by Persson and Zahr [102] and related techniques for high-order approximations of compressible flows. Nevertheless, registration for MOR applications has several specificities that require innovative methodological solutions and motivate further research: first, in order to allow the correct enforcement of boundary conditions, the mapping should exactly preserve the boundary of the domain for all parameter values; second, the quality of the deformed mesh $\mu \mapsto \Phi_\mu(\mathcal{T}_{\rm hf})$ should be controlled; third, registration should rely on a moderate number of possibly low-fidelity snapshots to reduce the offline costs.

This chapter summarizes my contributions to nonlinear MOR based on coordinate transformations. In section 3.1, I introduce Lagrangian approximations for parametric systems: I discuss the link with r-adaptation and I introduce rigorous metrics to assess performance. In section 3.2, I review the problem of parametric registration in bounded domains: the presentation is mainly based on the recent preprint [TT15] and it builds upon the previous works [TT13, TT18, TT19, TT14]. In section 3.3, I present an integrated strategy, which I proposed in [TT4] together with Barral and Tifouti, to adaptively build the mesh, the parametric mapping, and the ROM: the approach in [TT4] extends the techniques discussed in [TT6, TT13, TT19]; in particular, it incorporates parametric mesh adaptation (MA) in the offline stage. In section 3.4, I present a non-intrusive nonlinear MOR technique dubbed *convex displacement interpolation* that I proposed in [TT10] with Iollo and further developed in [TT5] in collaboration with Cucchiara, Iollo and Telib.

3.1 Lagrangian approximations for parametric systems

In this chapter, I consider the nonlinear ansatz

$$\widehat{u}_\mu = \widetilde{u}_\mu \circ \Phi_\mu^{-1}, \quad \text{where } \widetilde{u}_\mu = Z\widehat{\boldsymbol{\alpha}}_\mu, \ \ \Phi_\mu = \mathtt{N}\left(\widehat{\mathbf{a}}_\mu\right). \tag{3.1}$$

As in (2.13), $Z : \mathbb{R}^n \to \mathcal{X}_{\rm hf}$ is a linear (or affine) operator, and $\widehat{\boldsymbol{\alpha}} : \mathcal{P} \to \mathbb{R}^n$ is a vector-valued function of generalized coordinates; on the other hand, $\mathtt{N} : \mathbb{R}^m \to {\rm Lip}(\Omega; \mathbb{R}^d)$ is a suitable, possibly nonlinear, operator that is informed by the domain Ω and $\widehat{\mathbf{a}} : \mathcal{P} \to \mathbb{R}^m$ is a vector-valued function of generalized coordinates for the mapping. The entries of $\widehat{\boldsymbol{\alpha}}_\mu$ are dubbed solution (generalized) coordinates, while the entries of $\widehat{\mathbf{a}}_\mu$ are dubbed mapping (generalized) coordinates. In the FE framework, or equivalently in the finite volume context, the ansatz (3.1) corresponds to considering approximations of the form

$$\mu \in \mathcal{P} \mapsto (\Phi_\mu(\mathcal{T}_{\rm hf}), \widehat{\mathbf{u}}_\mu = \mathbf{Z}\widehat{\boldsymbol{\alpha}}_\mu)\,, \tag{3.2}$$

for a given FE mesh $\mathcal{T}_{\rm hf}$ and for a given matrix $\mathbf{Z} \in \mathbb{R}^{N_{\rm hf}\times n}$. The method is hence linear with respect to the solution coordinates and highly nonlinear with respect to the mapping coordinates. Note also that the mesh used to approximate the infinite-dimensional PDE varies with the parameter through the mapping Φ: well-crafted mesh morphings $\mu \mapsto \Phi_\mu(\mathcal{T}_{\rm hf})$ have hence the potential to enhance the accuracy of the underlying HF discretization (*mesh r-adaptation*).

Lagrangian approximations are designed to approximate parametric fields with localized features that vary smoothly with the parameters; in this scenario, it is possible to find a smooth parametric mapping Φ that freezes the location of the coherent structures in the reference configuration and ultimately simplifies the tasks of model reduction and mesh adaptation. Given the solution manifold $\mathcal{M}$, we can rigorously measure the performance of Lagrangian approximations through the vehicle of a nonlinear Kolmogorov width: the nonlinear width enables to identify the class of problems that are well-suited for Lagrangian methods.

Following [TT13], I define the Banach space $\mathcal{X}$ over Ω such that $\mathcal{M} \subset \mathcal{X}$ and $u \circ \Phi \in \mathcal{X}$ for any $u \in \mathcal{X}$ for all Lipschitz isomorphisms Φ in Ω. Then, given the operator $\mathtt{N} : \mathbb{R}^m \to {\rm Lip}(\Omega;\mathbb{R}^d)$, I define the set of admissible maps

$$A(\mathtt{N},\epsilon) = \{\mathbf{a} \in \mathbb{R}^m \ : \ \mathtt{N}(\mathbf{a}) \text{ is an isomorphism}, \ \ \det(\nabla \mathtt{N}(\mathbf{a})) > \epsilon\}\,; \tag{3.3a}$$

then, I introduce the $n-m$ Kolmogorov width

$$\mathfrak{d}_{n,m,\epsilon}\left(\mathcal{M}, \|\cdot\|_{\mathcal{X}}\right) = \inf_{\substack{\mathtt{N}:\mathbb{R}^m\to{\rm Lip}(\Omega;\mathbb{R}^d) \\ \mathcal{Z}\subset\mathcal{X},\dim(\mathcal{Z})=n}} \ \sup_{w\in\mathcal{M}} \left(\inf_{\mathbf{a}\in A(\mathtt{N},\epsilon),\zeta\in\mathcal{Z}} \|w - \zeta\circ\mathtt{N}(\mathbf{a})^{-1}\|_{\mathcal{X}} \right). \tag{3.3b}$$

By construction, $\mathfrak{d}_{n,m,\epsilon}\left(\mathcal{M}, \|\cdot\|_{\mathcal{X}}\right)$ is monotonically decreasing in n and m; furthermore, for $m=0$ (3.3b) reduces to the standard Kolmogorov n-width,

$$\mathfrak{d}_{n}\left(\mathcal{M}, \|\cdot\|_{\mathcal{X}}\right) = \inf_{\mathcal{Z}\subset\mathcal{X},\dim(\mathcal{Z})=n} \ \sup_{w\in\mathcal{M}} \left(\inf_{\zeta\in\mathcal{Z}} \|w-\zeta\|_{\mathcal{X}} \right).$$

Lagrangian methods are hence well-suited for problems for which

$$\mathfrak{d}_{n,m,\epsilon}\left(\mathcal{M}, \|\cdot\|_{\mathcal{X}}\right) \ll \mathfrak{d}_{n}\left(\mathcal{M}, \|\cdot\|_{\mathcal{X}}\right) \quad \text{for } \ m = \mathcal{O}(n).$$

To provide a concrete example, consider the parametric field

$$u_\mu(x_1,x_2) = \left\{ \begin{array}{ll} 0 & \text{if } x_2 < f_\mu(x_1) \\ 1 & \text{if } x_2 \geq f_\mu(x_1) \end{array} \right. \qquad \text{where } f_\mu \in {\rm Lip}([0,1]) \text{ satisfies } f_\mu([0,1]) \subset \big[\delta, 1-\delta\big],$$

defined in $\Omega = (0,1)^2$. Then, for any $\epsilon < 2\delta$, it is possible to show that (cf. [TT13])

$$\mathfrak{d}_{n,m,\epsilon}\left(\mathcal{M}, \|\cdot\|_{L^1(\Omega)}\right) \lesssim \frac{\mathfrak{d}_{n}\left(\mathcal{M}_{\rm f}, \|\cdot\|_{\rm Lip}\right)}{\sqrt{n}}, \qquad \mathfrak{d}_{n}\left(\mathcal{M}, \|\cdot\|_{L^1(\Omega)}\right) \sim \frac{1}{\sqrt{n}}, \tag{3.4}$$

where $\mathcal{M}_{\rm f} = \{f_\mu : \mu \in \mathcal{P}\}$. Estimate (3.4) suggests that the introduction of the morphing does not affect the convergence rate with respect to the size n of the reduced space in the mapped configuration; furthermore, the estimate shows that Lagrangian approximations depend on the premise that the solution's discontinuities can be expressed as a low-rank deformation of a template discontinuity set.

3.2 Parametric registration in bounded domains

To properly contextualize my work on registration methods, I briefly review the problem of PSR. Given the point clouds $X = \{x_i\}_{i=1}^N, Y = \{y_j\}_{j=1}^M \subset \mathbb{R}^d$, the problem of PSR consists in finding a map $\Phi : \mathbb{R}^d \to \mathbb{R}^d$ that (approximately) minimizes the Hausdorff distance

$${\rm dist}_{\rm H}\left(Y, \Phi(X)\right) := \max\left\{{\rm dist}\left(Y,\Phi(X)\right),\ {\rm dist}\left(\Phi(X), Y\right)\right\}, \ \text{with} \ \ {\rm dist}\left(U,V\right) = \max_{u\in U}\left(\min_{v\in V}\|u-v\|_2\right) \tag{3.5}$$

in a suitable approximation set (or *model class*); the output of the algorithm is the deformed set of points $\Phi(X) = \{\Phi(x_i)\}_{i=1}^N$. A broad range of PSR methods relies on a probabilistic interpretation of the problem: these methods rely on the assumption that $\{x_i\}_{i=1}^N$ and $\{y_j\}_{j=1}^M$ are independent identically distributed (iid) samples from a given probability distribution with unknown parameters, and exploit tools from optimal transportation theory [40, 76].

The problem of aligning datasets of point clouds has obvious connections with the problem of aligning coherent structures of the solution to given PDEs; however, the latter problem poses several fundamental challenges that need to be addressed.

- *Feature selection.* Given the solution field $u_\mu : \Omega \to \mathbb{R}^D$, we should identify a suitable function of u_μ that can be used for registration. Following taxonomy introduced in [TT15], we might distinguish between *distributed sensors*, which associate u_μ to a scalar continuous field s_μ, and *point-set sensors*, which associate u_μ to a point cloud $X_\mu = \{x_{i,\mu}\}_{i=1}^{N_\mu} \subset \Omega$. The choice of the sensor requires a deep understanding of the underlying physical model and of the features we wish to track.

- *Bijectivity constraint.* In MOR, we seek mappings that are bijective from Ω in itself; furthermore, in PMOR the mapping should be bijective with respect to the computational mesh (cf. Chapter 2.4). The enforcement of the bijectivity constraint poses major challenges and requires a careful choice of the model class.

- *Parametric registration.* In MOR, we are primarily interested in determining a parameter-dependent low-rank isomorphism $\Phi : \Omega \times \mathcal{P} \to \Omega$. This involves the solution to multiple registration problems and the development of specialized data compression techniques to identify low-rank structures while preserving the structure of the map.

In [TT13], I proposed an optimization-based approach to the problem of registration in bounded domains. Given the domain $\Omega \subset \mathbb{R}^d$, I denote by $\mathfrak{B}$ the space of Lipschitz bijections from Ω in itself and by $\mathfrak{D} = \mathfrak{D}(\Omega)$ the space of diffeomorphisms from Ω in itself. Given the mapping Φ, I denote by $J(\Phi)$ the Jacobian determinant, and I denote by $\texttt{id} : \mathbb{R}^d \to \mathbb{R}^d$ the identity map in $\mathbb{R}^d$, $\texttt{id}(x) = x$ for all $x \in \mathbb{R}^d$. If we fix the value of $\mu \in \mathcal{P}$, our goal is to minimize a target function $\mathfrak{f}_\mu^{\rm tg}$ over all possible diffeomorphisms of Ω,

$$\min_{\Phi \in \mathfrak{D}} \mathfrak{f}_\mu^{\rm tg}(\Phi). \tag{3.6}$$

Problem (3.6) is computationally intractable due to the fact that $\mathfrak{D}$ is an highly non-convex subset of $C^1(\Omega; \mathbb{R}^d)$: research on registration hence focuses on the development of computational strategies to devise tractable counterparts of the statement (3.6).

3.2.1 Optimization-based registration

To devise a tractable registration procedure, I introduce an operator $\texttt{N} : \mathbb{R}^M \to {\rm Lip}(\Omega; \mathbb{R}^d)$ and a penalty function $\mathfrak{f}^{\rm pen} : \mathbb{R}^M \to \mathbb{R}_+$ such that

$$\begin{cases} \mathcal{B}_{\texttt{N}} = \{\texttt{N}(\mathbf{a}) \; : \; \mathfrak{f}^{\rm pen}(\mathbf{a}) \leq C\} \subset \mathcal{B}, & \text{for some } C > 0; \\ \texttt{N}(\mathbf{a} = 0) = \texttt{id}, \;\; \mathfrak{f}^{\rm pen}(\mathbf{a} = 0) < C; & \\ \texttt{N}, \; \mathfrak{f}^{\rm pen} \text{ are Lipschitz continuous.} & \end{cases} \tag{3.7}$$

Equations $(3.7)_1$ and $(3.7)_2$ imply that the set $\mathcal{B}_{\texttt{N}}$ is not empty; furthermore, exploiting $(3.7)_3$ we find that the interior of $\mathcal{B}_{\texttt{N}}$ is not empty — that is, bijectivity of the mapping $\texttt{N}(\mathbf{a})$ is preserved for small perturbations of the mapping coefficients $\mathbf{a}$. I further observe that, given the full rank matrix $\mathbf{W} \in \mathbb{R}^{M \times m}$, the pair $(\widetilde{\texttt{N}}, \widetilde{\mathfrak{f}^{\rm pen}})$ such that $\widetilde{\texttt{N}}(\cdot) = \texttt{N}(\mathbf{W}\cdot)$ and $\widetilde{\mathfrak{f}^{\rm pen}}(\cdot) = \mathfrak{f}^{\rm pen}(\mathbf{W}\cdot)$ satisfies (3.7): this implies that the application of linear dimensionality reduction methods such as POD preserves the structure of the map.

Exploiting the definitions of $\texttt{N}$ and $\mathfrak{f}^{\rm pen}$, I introduce the tractable surrogate of (3.6):

$$\min_{\mathbf{a} \in \mathbb{R}^M} \mathfrak{f}_\mu^{\rm tg}(\texttt{N}(\mathbf{a})) \quad \text{subject to} \quad \mathfrak{f}^{\rm pen}(\mathbf{a}) \leq C,$$

which reads as a nonlinear non-convex constrained optimization statement. I also introduce the corresponding unconstrained formulation:

$$\min_{\mathbf{a} \in \mathbb{R}^M} \mathfrak{f}_\mu^{\rm obj}(\mathbf{a}) := \mathfrak{f}_\mu^{\rm tg}(\texttt{N}(\mathbf{a})) \; + \xi \; \mathfrak{f}^{\rm pen}(\mathbf{a}). \tag{3.8}$$

Provided that ξ is sufficiently large, solutions $\mathbf{a}^\star$ to (3.8) also satisfy the condition $\mathfrak{f}^{\rm pen}(\mathbf{a}^\star) \leq C$. Note that (3.8) reads as a nonlinear non-convex unconstrained optimization problem that can be tackled using standard gradient-descent optimization algorithms. In the next sections, I discuss the choice of the operator $\texttt{N}$ and its approximation properties in the space of diffeomorphisms of Ω, the choice of the penalty term $\mathfrak{f}^{\rm pen}$, the choice of the target function $\mathfrak{f}^{\rm tg}$, and the extension to the parametric setting.

The previous discussion highlights the two major questions in registration methods: (i) how to construct $(\mathtt{N}, \mathfrak{f}_{\rm pen})$ that satisfy (3.7) for a given domain Ω; (ii) how to establish a rigorous relation between the solutions to (3.6) and to (3.8) in the limit $M \to \infty$. Note that the second question concerns the ability of approximating arbitrary elements of $\mathfrak{D}$ using operators $\mathtt{N}$ that satisfy (3.7). I notice that even if we focus on the approximation of diffeomorphisms we allow ourselves to consider approximations in a less regular space: this choice is justified by the particular discretization method (the finite element (FE) method) employed in this work to represent the operator $\mathtt{N}$ and, more fundamentally, by the strategy proposed here to define $\mathtt{N}$.

3.2.2 Choice of the operator $\mathtt{N}$

In order to find $\mathtt{N}$ and $\mathfrak{f}^{\rm pen}$ that satisfy (3.7) for an arbitrary domain Ω, I introduce the sets

$$A := \{\mathbf{a} \in \mathbb{R}^M \, : \, \mathtt{N}(\mathbf{a}) \in \mathfrak{B}\}, \quad A_{\rm jac} := \{\mathbf{a} \in \mathbb{R}^M \, : \, \inf_{x\in\Omega} J(\mathtt{N}(\mathbf{a})) > 0\}. \tag{3.9}$$

Then, I require that the condition $\inf_{x\in\Omega} J(\Phi) > 0$ implies bijectivity in Ω for any mapping Φ spanned by $\mathtt{N}$, that is

$$A_{\rm jac} \subset A. \tag{3.10}$$

Note that the pointwise condition $J(\mathtt{N}(\mathbf{a}))(x) > 0$ for all $x \in \Omega$ cannot be directly translated into a penalty term for (3.8): to simplify the presentation, I address the construction of the penalty term in the next section. It is possible to construct maps Φ that are bijective in Ω for which $\inf_{x\in\Omega} J(\Phi) = 0$ (cf. [83, Theorem 1.1]); however, bijections Φ which satisfy $\inf_{x\in\Omega} J(\Phi) = 0$ are of little practical interest for scientific computing applications and in particular for (projection-based) MOR.

Affine maps in polytopal domains

I first consider the case of polytopal domains. The domain $\Omega_{\rm p} \subset \mathbb{R}^2$ is said a polytope if the boundary of $\Omega_{\rm p}$, $\partial\Omega_{\rm p}$, consists of a finite number of flat sides (*faces*); I denote by $\mathbf{n}(x)$ the outward normal to $\Omega_{\rm p}$ at $x \in \partial\Omega_{\rm p}$; I further denote by $V = \{x_i^{\rm v}\}_{i=1}^{N_{\rm v}}$ the points of $\partial\Omega_{\rm p}$ where two consecutive edges meet (*vertices*). The polytope $\Omega_{\rm p}$ is said to be regular if if there exist $N+1$ bounded polytopes $\Omega_{{\rm int},1}, \ldots, \Omega_{{\rm int},N}, \Omega_{\rm ext}$ such that (i) $\Omega_{\rm p} = \Omega_{\rm ext} \setminus \bigcup_{i=1}^N \Omega_{{\rm int},i}$, (ii) $\Omega_{{\rm int},1}, \ldots, \Omega_{{\rm int},N}$ are pairwise disjoint polytopes that are compactly embedded in $\Omega_{\rm ext}$ and (iii) $\Omega_{\rm ext}, \Omega_{{\rm int},1}, \ldots, \Omega_{{\rm int},N}$ are isomorphic to the unit ball (cf. [TT15, Definition 2.1]). Proposition 3.2.1 summarizes key results for two-dimensional polytopal domains.

Proposition 3.2.1. *(cf. [TT15]) Let $\Omega_{\rm p}$ be a regular bounded polytope. Define the space $\mathfrak{U}_{\rm p} = \{\varphi \in C^1(\overline{\Omega}_{\rm p}; \mathbb{R}^2) \, : \, \varphi \cdot \mathbf{n}|_{\partial\Omega_{\rm p}} = 0\}$. Then, the following hold.*

1. *Let $\mathcal{U}_{\rm p}$ be an M-dimensional space spanned by $\{\varphi_i\}_{i=1}^M \subset \mathfrak{U}_{\rm p}$ and set $\mathcal{W}_{\rm p} := \boldsymbol{id} + \mathcal{U}_{\rm p}$. Then, the affine operator $\mathtt{N}_{\rm p} : \mathbb{R}^M \to \mathcal{W}_{\rm p}$ such that $\mathtt{N}_{\rm p}(\mathbf{a}) = \boldsymbol{id} + \sum_{i=1}^M (\mathbf{a})_i \varphi_i$ satisfies (i) $A_{\rm jac} \subset A$, (ii) $\mathtt{N}_{\rm p} \in {\rm Lip}(\mathbb{R}^M; \mathcal{W}_{\rm p})$, and (iii) $\mathtt{N}_{\rm p}(0) = \boldsymbol{id}$.*

2. *Let $\Phi : \Omega_{\rm p} \times \mathcal{P} \to \Omega_{\rm p}$ be a continuous function of the parameter $\mu \in \mathcal{P}$ and let Φ_μ be a diffeomorphism for all $\mu \in \mathcal{P}$. Assume that $\Phi_{\mu'} = \boldsymbol{id}$ for some $\mu' \in \mathcal{P}$. Then, $\Phi_\mu = \boldsymbol{id} + \varphi_\mu$ with $\varphi_\mu \in \mathfrak{U}_{\rm p}$ for all $\mu \in \mathcal{P}$.*

The first statement of Proposition 3.2.1 provides a constructive way of building approximation spaces for registration in polytopes; the second statement shows that the image of $\mathtt{N}_{\rm p}$ $\mathcal{W}_{\rm p} = \mathtt{N}_{\rm p}(\mathbb{R}^M)$ is dense (in the limit $M \to \infty$) in a representative subset of diffeomorphisms in Ω. In the setting of MOR, we are interested in parametric maps that are smooth deformations of the identity map: since registration is applied with respect to an element of the solution manifold $\mathcal{M} = \{u_\mu : \mu \in \mathcal{P}\}$, we can indeed assume that there exists $\mu \in \mathcal{P}$ such that $\Phi_\mu = \mathtt{id}$.

In [TT15], I also discuss the extension of the analysis to Lipschitz maps. The proof of the first statement of Proposition 3.2.1 exploits the Hadamard's global inverse function theorem (cf. [54, Theorem 6.2.8]); it hence relies on the assumption that Φ is of class C^1. Numerical investigations suggest that a similar result — possibly with further conditions — might hold for piecewise-smooth maps such as FE fields. On the other hand, the second statement of Proposition 3.2.1 does not hold for general Lipschitz mappings (cf. [TT15, section 2.4]).

Compositional maps in arbitrary domains

Affine maps are fundamentally ill-suited to deal with domains with curved boundaries (cf. [TT18, Lemma 2.1] and [TT15, Lemma 3.1]); this motivates the development of nonlinear ansatzs for registration in curved domains. In [TT15], I proposed to resort to compositional maps of the form

$$\mathtt{N}(\mathbf{a}) = \Psi \circ \mathtt{N}_{\rm p}(\mathbf{a}) \circ \Psi^{-1}, \tag{3.11}$$

where $\Psi : \Omega_{\rm p} \to \Omega$ is a bijection from the polytope $\Omega_{\rm p}$ to Ω and $\texttt{N}_{\rm p}(\mathbf{a}) : \Omega_{\rm p} \to \Omega_{\rm p}$ is affine in $\mathbf{a}$, that is $\texttt{N}_{\rm p}(\mathbf{a}) = \texttt{id} + \sum_{i=1}^M (\mathbf{a})_i \varphi_i$ for suitably chosen functions $\{\varphi_i\}_i$ whose normal components vanish on $\partial\Omega_{\rm p}$, $\varphi_i \cdot \mathbf{n}|_{\partial\Omega_{\rm p}} = 0$ for $i = 1, \ldots, M$. I also discussed the multi-layer generalization of (3.11)

$$\texttt{N}\left(\mathbf{a} = [\mathbf{a}_1, \ldots, \mathbf{a}_\ell]\right) = \texttt{N}_1\left(\mathbf{a}_1\right) \circ \ldots \circ \texttt{N}_\ell\left(\mathbf{a}_\ell\right), \tag{3.12}$$

where $\texttt{N}_i\left(\mathbf{a}_i\right) = \Psi_i \circ \texttt{N}_{{\rm p},i}(\mathbf{a}_i) \circ \Psi_i^{-1}$ with $\Psi_i : \Omega_{{\rm p},i} \to \Omega$ is a Lipschitz bijection and $\Omega_{{\rm p},i}$ is a suitable polytope, for $i = 1, \ldots, \ell$.

The problem of finding the polytope $\Omega_{\rm p}$ and the mapping Ψ can be recast as the problem of building a high-order curved mesh $\mathcal{T}_{\rm rg}$ of the domain Ω. I refer to [TT15, section 4] for the construction of $\Omega_{\rm p}$ and the mapping Ψ; Figure 3.1(a) shows the curved mesh $\mathcal{T}_{\rm rg}$ of the domain Ω considered in the numerical examples of [TT15] and Figure 3.1(b) shows the corresponding linear mesh; the polytope $\Omega_{\rm p}$ is the union of the elements of the linear mesh $\mathcal{T}_{\rm p}$.

If we denote by $V \subset \partial\Omega_{\rm p}$ the vertices of $\Omega_{\rm p}$ and by $W = \Psi(V) \subset \partial\Omega$ the corresponding mapped vertices, it is possible to show that maps (3.11) satisfy $\texttt{N}(\mathbf{a})|_W = \texttt{id}$ for all $\mathbf{a} \in \mathbb{R}^M$; therefore, the model class (3.11) is not dense in the space of diffeomorphisms in Ω. On the other hand, the multi-layer generalization (3.12) can be used to approximate arbitrary diffeomorphisms in Ω, under the hypothesis of small deformations (cf. [TT15, Lemma 3.3]). In more detail, the analysis shows that multi-layer maps provide much more approximation power, even for moderate numbers of layers ℓ. However, multi-layer maps are considerably more challenging to implement and might also be significantly more expensive to evaluate: the solution to (3.8) requires indeed many evaluations of the mapping $\texttt{N}(\mathbf{a})$ and its gradient, which involve the evaluation of the bijections $\{\Psi_i\}_{i=1}^\ell$ and their inverses. For this reason, so far I exclusively focused on the implementation of registration strategies based on the more elementary ansatz (3.11).

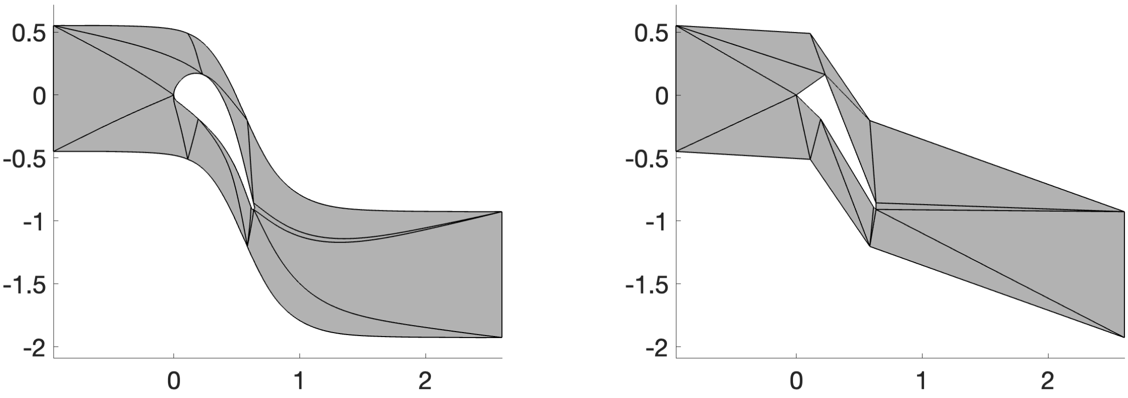

(a) (b)

Figure 3.1: inviscid flow past an array of LS89 turbine blades. (a) curved mesh $\mathcal{T}_{\rm rg}$ for registration. (b) coarse-grained linear mesh $\mathcal{T}_{\rm p}$.

3.2.3 Choice of the penalty function

I denote by $\mathcal{U}_{\rm p}$ a vector-valued FE space of order $\kappa > 1$ defined in the linear mesh $\mathcal{T}_{\rm p}$ of the polytope $\Omega_{\rm p}$, whose elements have vanishing normal component on $\partial\Omega_{\rm p}$. I denote by $\{\varphi_i\}_{i=1}^M$ a basis of $\mathcal{U}_{\rm p}$. I introduce the HF mesh $\mathcal{T}_{\rm hf}$ of Ω used for full-order calculations — which is independent of the mesh $\mathcal{T}_{\rm rg}$ used to define the mapping space (cf. Figure 3.1). I denote by $\{\texttt{D}_k^{\rm hf}\}_{k=1}^{N_{\rm e}}$ and $\{\Psi_k^{\rm hf}\}_{k=1}^{N_{\rm e}}$ the elements and the elemental mappings of $\mathcal{T}_{\rm hf}$ (cf. (2.3)); I use notation $\{\Psi_{\Phi,k}^{\rm hf}\}_{k=1}^{N_{\rm e}}$ to refer to the elemental mappings of the deformed mesh. I further introduce the elements $\{\texttt{D}_{k,{\rm p}}\}_{k=1}^{N_{\rm e,p}}$ and the facets $\{\texttt{F}_{j,{\rm p}}\}_{j=1}^{N_{\rm f,p}}$ of the linear mesh $\mathcal{T}_{\rm p}$ of $\Omega_{\rm p}$. In view of the discussion, I denote by $H(\Phi)$ the Hessian of the function Φ and I denote by $\|\cdot\|_{\rm F}$ the Frobenius norm.

Given the polytope $\Omega_{\rm p}$, the constants $\epsilon > 0$ and $C_{\rm exp}$ such that $C_{\rm exp} \ll \epsilon$, I introduce the function

$$\mathfrak{f}_{\rm pen}^{(1)}(\Phi) = \frac{1}{|\Omega_{\rm p}|} \int_{\Omega_{\rm p}} \exp\left(\frac{\epsilon - J(\Phi)}{C_{\rm exp}}\right) dx \; + \; \|\nabla J(\Phi)\|_{L^\infty(\Omega_{\rm p})}. \tag{3.13}$$

By tedious but straightforward calculations, it is possible to verify that there exist constants $C, C_{\rm exp}$ such that the condition $\mathfrak{f}_{\rm pen}^{(1)}(\Phi) \leq C$ implies that $J(\Phi) \geq \epsilon/2$ for all $x \in \Omega_{\rm p}$ (cf. [TT13, section 2.2]). Recalling Jacobi's formula, we find that $\|\nabla J(\Phi)\|_2 \leq C \|\nabla\Phi\|_{\rm F} \|H(\Phi)\|_{\rm F}$, for some constant C that is independent of $\nabla\Phi$; therefore, we can replace $\|\nabla J(\Phi)\|_{L^\infty(\Omega_{\rm p})}$ with $\|H(\Phi)\|_{L^\infty(\Omega_{\rm p})}$ (3.13). Finally, exploiting the fact that the operator $\mathtt{N}_{\rm p}$ is finite-dimensional, we replace the L^∞ norm with the L^2 norm in (3.13) to obtain

$$\mathfrak{f}_{\rm pen}^{(2)}(\Phi) = \frac{1}{|\Omega_{\rm p}|}\int_{\Omega_{\rm p}} \exp\left(\frac{\epsilon - J(\Phi)}{C_{\rm exp}}\right) dx \; + \; \|H(\Phi)\|_{L^2(\Omega_{\rm p})}^2. \tag{3.14}$$

The penalty term (3.14) can be extended to the ansatz (3.11) for registration in general domains: since Ψ and Ψ^{-1} do not depend on the mapping coefficients $\mathbf{a}$, it suffices to ensure that $\mathtt{N}_{\rm p}(\mathbf{a})$ is bijective in the polytope $\Omega_{\rm p}$. We conclude that the penalty (3.14) and the operator $\mathtt{N}$ in (3.11) satisfy the desiderata (3.7).

Even if the penalty $\mathfrak{f}_{\rm pen}^{(2)}$ satisfies (3.7), it is not tailored to the discrete representation of the FE fields $\{\varphi_i\}_{i=1}^M$ that are not H^2-conforming; furthermore, the penalty does not ensure that the deformed mesh $\Phi(\mathcal{T}_{\rm hf})$ is well-behaved. For this reason, in [TT15] I proposed the following penalty term:

$$\mathfrak{f}^{\rm pen}(\mathbf{a}) = \mathfrak{f}_{\rm jac}(\mathtt{N}_{\rm p}(\mathbf{a})) + \mathfrak{f}_{\rm msh}(\mathtt{N}(\mathbf{a})) + \mathfrak{P}\left(\mathtt{N}_{\rm p}(\mathbf{a})\right). \tag{3.15a}$$

Here, the function $\mathfrak{f}_{\rm jac}$ is designed to ensure that the selected map is non-singular,

$$\mathfrak{f}_{\rm jac}(\Phi_{\rm p}) = \frac{1}{|\Omega_{\rm p}|}\int_{\Omega_{\rm p}} \exp\left(\frac{\epsilon - J(\Phi_{\rm p})}{C_{\rm exp}}\right) dx, \quad \text{with } \epsilon \in (0,1), \;\; C_{\rm exp} \ll \epsilon; \tag{3.15b}$$

the function $\mathfrak{f}_{\rm msh}$ controls the quality of the deformed mesh

$$\mathfrak{f}_{\rm msh}(\Phi) = \frac{1}{|\Omega|}\sum_{k=1}^{N_{\rm e}^{\rm pb}} |\mathtt{D}_k^{\rm pb}| \int_{\widehat{\mathtt{D}}} \exp\left(\frac{q_k^{\rm msh}(\Phi)}{q_k^{\rm msh}(\mathtt{id})} - \kappa_{\rm msh}\right) dx, \;\; \text{with } \kappa_{\rm msh} > 1, \tag{3.15c}$$

where

$$q_k^{\rm msh}(\Phi) := \frac{1}{d^2}\left(\frac{\|\nabla \Psi_{\Phi,k}^{\rm hf}\|_{\rm F}^2}{(\det(\nabla \Psi_{\Phi,k}^{\rm hf}))_+^{2/d}}\right)^2, \quad d = 2,3. \tag{3.15d}$$

Finally, the penalty $\mathfrak{P}$ is a FE counterpart of the H^2 seminorm

$$\begin{aligned} \mathfrak{P}\left(\varphi\right) = & \sum_{k=1}^{N_{\rm e,p}} \int_{\mathtt{D}_{k,\rm p}} \left(H(\varphi) : H(\varphi)\right) dx \\ + & \sum_{j \in \mathtt{I}_{\rm int}} \int_{\mathtt{F}_{j,\rm p}} \left(\beta_j [\![\nabla\varphi]\!] \cdot [\![\nabla\varphi]\!] + \frac{1}{\beta_j}\{H(\varphi)\} : \{H(\varphi)\}\right) dx; \end{aligned} \tag{3.15e}$$

where $[\![\cdot]\!]$ and $\{\cdot\}$ are the standard jump and average terms, $\mathtt{I}_{\rm int} \subset \{1, \ldots, N_{\rm f,p}\}$ are the indices of internal facets of the mesh $\mathcal{T}_{\rm p}$, $\beta_j = 10\kappa^2 |\mathtt{F}_{j,\rm p}|^{-1}$;

Some comments are in order. The penalty (3.15e) satisfies $\mathfrak{P}\left(\Phi\right) = 0$ for any linear map $\Phi(x) = \mathbf{b} + \mathbf{A}x$; in particular, $\mathfrak{P}\left(\mathtt{id}\right) = 0$; the jump and average terms are justified by the fact that we rely on a H^2-nonconforming discretization; the particular choice of the inner product is inspired by the analysis in [70, section 4] for the biharmonic equation. The ratio $q_k^{\rm msh}$ measures the degree of anisotropy of the mesh and it can thus be interpreted as a measure of the quality of the deformed mesh — the indicator $q_k^{\rm msh}$ was used in [103] in the framework of DG methods. The decision to activate the penalty terms $\mathfrak{f}_{\rm jac}$ and/or $\mathfrak{f}_{\rm msh}$ depends on the particular way we treat parameterized geometries — map-then-discretize or discretize-then-map (cf. Chapter 2.4).

3.2.4 Target function

The target $\mathfrak{f}_\mu^{\rm tg}$ measures the degree of similarity between the available estimate of the solution field u_μ to the problem of interest and a suitable template solution or template reduced space; $\mathfrak{f}_\mu^{\rm tg}$ relies on the introduction of a sensor $s_\mu := \mathfrak{s}_\mu(u_\mu)$ which should highlight the coherent structures we wish to track. Below, I distinguish between *point-set sensors* and *distributed sensors.*

Target function based on point-set sensors

Point-set sensors are based on the introduction of a scalar testing function that selects the points of the mesh $\{x_{\mu,j}^\star\}_{j=1}^{N_\mu^\star}$ where the solution u_μ satisfies a suitable user-defined criterion (cf. [TT10]), for any $\mu \in \mathcal{P}$. Given the template point cloud $\{\bar{x}_j^\star\}_{j=1}^{\overline{N}^\star}$ — which can be prescribed *a priori* or be chosen based on one specific value of the parameters — and the parameter value $\mu \in \mathcal{P}$, we first rely on a standard point-set registration (PSR) procedure (e.g., [71]) that takes as inputs the point clouds $\{\bar{x}_j^\star\}_{j=1}^{\overline{N}^\star}$ and $\{x_{\mu,j}^\star\}_{j=1}^{N_\mu^\star}$, to determine the deformed points $\{\widehat{x}_{j,\mu}^\star\}_{j=1}^{\overline{N}^\star}$ that approximates $\{x_{\mu,j}^\star\}_{j=1}^{N_\mu^\star}$ in the sense of (3.5); then, we solve the optimization problem (3.8) with

$$\mathfrak{f}_\mu^{\rm tg}\left(\Phi\right) = \frac{1}{\overline{N}^\star}\sum_{i=1}^{\overline{N}^\star}\|\Phi(\bar{x}_i^\star) - \widehat{x}_{i,\mu}^\star\|_2^2. \tag{3.16}$$

As discussed in [TT10] and also [TT14], we can interpret the solution to (3.8) with objective (3.15) -(3.16) as an approximate projection of the mapping returned by the PSR procedure — since the latter is neither guaranteed to map the boundary of the domain Ω in itself nor to be globally bijective — onto the space of admissible bijections in Ω.

Target function based on distributed sensors

A distributed sensor is a function of the solution field u_μ that highlights the features of u_μ that we wish to track. Given the reduced n-dimensional space $\mathcal{Z}_n$ embedded in a Hilbert space $\mathcal{X}$ defined over Ω, in model reduction the parametric mapping Φ should minimize the target

$$\mathfrak{f}_\mu^{\rm tg,opt}\left(\Phi\right) := \min_{\zeta\in\mathcal{Z}_n}\int_\Omega \|u_\mu\circ\Phi - \zeta\|_2^2\,dx, \tag{3.17}$$

over all values of μ in $\mathcal{P}$: $\mathfrak{f}_\mu^{\rm tg,opt}\left(\Phi\right)$ is the projection error in the mapped configuration. Note that $\mathfrak{f}_\mu^{\rm tg,opt}$ depends on the choice of the reduced space $\mathcal{Z}_n$ whose selection is inherently coupled with the problem of finding Φ: I postpone the procedure for the construction of the reduced space to the next section.

The explicit use of the solution u_μ in the optimization statement (3.8) is computationally unfeasible and prone to instabilities: first, the solution u_μ is typically defined over an unstructured grid for which function evaluation at the deformed quadrature points $\{\Phi(x_q^{\rm qd})\}_{q=1}^{N_{\rm qd}}$ is extremely expensive; second, we might exploit prior knowledge about the problem of interest to identify a scalar function of u_μ that better isolates the features we wish to track (e.g., shocks) using registration, from the features we expect to be able to approximate through a linear expansion of (mapped) snapshots.

Exploiting the form of Φ, and the change-of-variable $x = \Psi(\xi)$, we find

$$\int_\Omega \|u_\mu\circ\Phi - \zeta\|_2^2\,dx = \int_{\Omega_{\rm p}} \|u_\mu\circ\Psi\circ\Phi_{\rm p} - \zeta\circ\Psi^{-1}\|_2^2\,J(\Psi)d\xi.$$

If we replace $u_\mu\circ\Psi$ with a scalar sensor s_μ defined over the domain $\Omega_{\rm p}$ and the reduced space $\mathcal{Z}_n$ for the solution with a space (dubbed *template space*) $\mathcal{S}_n\subset L^2(\Omega_{\rm p})$ for the sensor, we obtain

$$\mathfrak{f}_\mu^{\rm tg}\left(\Phi\right) := \min_{\nu\in\mathcal{S}_n}\int_{\Omega_{\rm p}} \left|s_\mu\circ\Phi_{\rm p} - \nu\right|^2 J(\Psi)\,dx, \tag{3.18}$$

which is the target function employed in the numerical experiments.

From the definition (3.18), I deduce that computation of $\mathfrak{f}_\mu^{\rm tg}(\Phi)$ requires to evaluate s_μ in the deformed quadrature points $\{\Phi_{\rm p}(x_q^{\rm qd,p})\}_q$ of the mesh $\mathcal{T}_{\rm p}$ at each iteration of the optimization algorithm for (3.8). Since the solution is discontinuous, I consider a P1 discretization of the sensor s_μ over a linear mesh $\mathcal{T}_{\rm p,s}$ of $\Omega_{\rm p}$, which is generated independently of $\mathcal{T}_{\rm p}$. Following [61], I rely on KD-trees to speed up mesh interpolation (cf. Matlab function `KDTreeSearcher`): since $\mathcal{T}_{\rm p}$ is a linear mesh with a modest number of elements, the evaluation of the sensor s_μ in the deformed quadrature points is still affordable. Notice that the same fast mesh interpolation routine should also be used to evaluate the FE mapping Ψ in (3.15c).

3.2.5 Parametric problem

The target function (3.18) depends on the template space $\mathcal{S}_n\subset L^2(\Omega_{\rm p})$. In [TT19], together with Zhang, I proposed an iterative procedure that, given a set of sensor snapshots $\{s_\mu : \mu\in\mathcal{P}_{\rm train}\}$ with $\mathcal{P}_{\rm train} = \{\mu^k\}_{k=1}^{n_{\rm train}}$, performs registration over the entire training set and then exploits the results to update the template space $\mathcal{S}_n$ in a greedy fashion. The procedure also returns the mapping Φ for all parameters in the training set $\{\Phi_\mu : \mu\in\mathcal{P}_{\rm train}\}$. In the remainder, I assume that $\{\varphi_i\}_{i=1}^M$ is a $\|\cdot\|$-orthonormal basis of the displacement space $\mathcal{U}_{\rm p}$ (cf. (3.11)), where the norm $\|\cdot\|$ is induced by the inner product

$$\begin{aligned}(w,v) = \;& \sum_{k=1}^{N_{\rm e}}\int_{\mathtt{D}_{k,\rm p}} \left(H(w):H(v) + w\cdot v\right)dx\\ + \;& \sum_{j\in\mathtt{I}_{\rm int}}\int_{\mathtt{F}_{j,\rm p}} \left(\beta_j[\![\nabla w]\!]\cdot[\![\nabla v]\!] + \frac{1}{\beta_j}\{H(w)\}:\{H(v)\}\right)dx.\end{aligned} \tag{3.19}$$

Algorithm 2 summarizes the computational procedure.

Algorithm 2 Registration algorithm

```
Inputs: $\{s_\mu : \mu \in \mathcal{P}_{\rm train}\}$ snapshot set, $\mathcal{S}_{n_0} = {\rm span}\{s_{\mu^{\star,(i)}}\}_{i=1}^{n_0}$ initial template space; $\mathcal{T}_{\rm hf}$ mesh for HF computations.
Outputs: $\mathcal{S}_n$ template space, $\mathbf{W} \in \mathbf{R}^{M\times m}$ mapping space, $\{\mathbf{a}^\star_{\mu^k}\}_k \subset \mathbb{R}^m$ optimal mapping coefficients.

 1: Initialization: $\mathcal{S}_{n=n_0} = \mathcal{S}_{n_0}$, $\Xi_\star = \{\mu^{\star,(i)}\}_{i=1}^{n_0}$, $\mathbf{W} = \mathbb{1}_M$.
 2: for $n = n_0, \ldots, n_{\rm max}-1$ do
 3:     $\left[\mathbf{a}^\star_\mu, \mathfrak{f}^\star_\mu\right] = \texttt{registration}\left(s_\mu, \mathcal{S}_n, \mathbf{W}, \mathcal{T}_{\rm hf}, \Psi, \mathbf{a}^0_\mu\right)$ for all $\mu \in \mathcal{P}_{\rm train}$.
                                                    see Remark 3.2.1 for definition of $\mathbf{a}^0_\mu$
 4:     $[\mathbf{W}, \{\mathbf{a}^{\rm proj}_\mu\}_{\mu\in\mathcal{P}_{\rm train}}] = \texttt{POD}\left(\{\mathbf{a}^\star_\mu\}_{\mu\in\mathcal{P}_{\rm train}}, tol_{\rm pod}, (\cdot,\cdot)_2\right)$.
 5:     if $\max_{\mu\in\mathcal{P}_{\rm train}} \mathfrak{f}^\star_\mu < \texttt{tol}$ then
 6:         break
 7:     else
 8:         $\Xi_\star = \Xi_\star \cup \{\mu^{\star,(n+1)}\}$ with $\mu^{\star,(n+1)} = \arg\max_{\mu\in\mathcal{P}_{\rm train}} \mathfrak{f}^\star_\mu$.
 9:         $\mathcal{S}_{n+1} = {\rm span}\{s_{\mu^{\star,(i)}} \circ \texttt{N}_{\rm p}(\mathbf{a}^{\rm proj}_{\mu^{\star,(i)}})\}_{i=1}^{n+1}$.
10:     end if
11: end for
```

Given the operator $\texttt{N}$, I define the orthogonal matrix $\mathbf{W} \in \mathbb{R}^{M\times m}$ and the low-rank map $\widehat{\texttt{N}}(\mathbf{a}) := \texttt{N}(\mathbf{W}\mathbf{a})$; by construction, we have $\|\mathbf{a}\|_2 = \|\sum_i (\mathbf{W}\mathbf{a})\varphi_i\|$ for any $\mathbf{a} \in \mathbb{R}^m$. Then, I introduce notation:

$$\left[\mathbf{a}^\star_\mu, \mathfrak{f}^\star_\mu\right] = \texttt{registration}\left(s_\mu, \mathcal{S}_n, \mathbf{W}, \mathcal{T}_{\rm pb}, \Psi, \mathbf{a}^0_\mu\right)$$

to refer to the function that takes as inputs (i) the target sensor $s_\mu : \Omega_{\rm p} \to \mathbb{R}$, (ii) the template space $\mathcal{S}_n$, (iii) the orthogonal matrix $\mathbf{W}$, (iv) the mesh $\mathcal{T}_{\rm pb}$, (v) the geometric mapping $\Psi : \Omega_{\rm p} \to \Omega$ and (vi) the initial guess $\mathbf{a}^0_\mu \in \mathbb{R}^m$ for the optimizer, and returns (I) the mapping coefficients $\mathbf{a}^\star_\mu$ that minimize the (reduced) objective $\mathbf{a} \mapsto \mathfrak{f}^{\rm obj}_\mu(\mathbf{W}\mathbf{a}^\star_\mu)$, and (II) the value of the target function $\mathfrak{f}^\star_\mu = \mathfrak{f}^{\rm tg}_\mu(\mathbf{W}\mathbf{a})$. Note that the objective $\mathfrak{f}^{\rm obj}_\mu : \mathbb{R}^M \to \mathbb{R}_+$ of (3.8) depends on the mesh $\mathcal{T}_{\rm hf}$ through the term $\mathfrak{f}_{\rm msh}$ in (3.15c). I also introduce the function

$$[\mathbf{W}_{\rm new}, \{\mathbf{a}^{\rm proj}_\mu\}_{\mu\in\mathcal{P}_{\rm train}}] = \texttt{POD}\left(\{\mathbf{W}_{\rm old}\mathbf{a}^\star_\mu\}_{\mu\in\mathcal{P}_{\rm train}}, tol_{\rm pod}, (\cdot,\cdot)_2\right),$$

which implements POD based on the method of snapshots with Euclidean inner product $(\cdot,\cdot)_2$: the tolerance $tol_{\rm pod} > 0$ drives the selection of the number of modes m based on the energy criterion

$$m := \min\left\{ m' : \sum_{j=1}^{m'} \lambda_j \geq (1 - tol_{\rm pod}) \sum_{i=1}^{n_{\rm train}} \lambda_i \right\}, \tag{3.20}$$

where $\lambda_1 \geq \ldots \geq \lambda_{n_{\rm train}} \geq 0$ are the eigenvalues of the Gramian matrix $\mathbf{C} \in \mathbb{R}^{n_{\rm train}\times n_{\rm train}}$ such that $(\mathbf{C})_{k,k'} = \mathbf{a}^\star_{\mu^k} \cdot \mathbf{a}^\star_{\mu^{k'}}$. The function $\texttt{POD}$ returns also the mapping coefficients associated with the projected displacements $\mathbf{a}^{\rm proj}_\mu = \mathbf{W}^\top_{\rm new}\mathbf{W}_{\rm old}\mathbf{a}^\star_\mu$; the latter are used to initialize the iterative method for the optimization problem for the subsequent iterations.

Remark 3.2.1. ***Further implementation details.*** *Since the optimization problem is highly non-convex, the choice of the initial condition is extremely important to avoid convergence to unsatisfactory local minima. For* $n = n_0+1, n_0+2, \ldots, n_{\rm max}-1$, *I simply use* $\mathbf{a}^0_\mu = \mathbf{a}^{\rm proj}_\mu$ *(cf. Line 4). On the other hand, for the first iteration, I first reorder the parameters in* $\mathcal{P}_{\rm train}$ *so that* $\mu^{(1)} = \arg\min_{\mu\in\mathcal{P}_{\rm train}} \|\mu - \mu^{\star,(1)}\|_2$ *and*

$$\mu^{(k)} = \arg \min_{\mu\in\mathcal{P}_{\rm train}\setminus\{\mu^{(i)}\}_{i=1}^{k-1}} \left(\min_{\mu'\in\{\mu^{(i)}\}_{i=1}^{k-1}} \|\mu - \mu'\|_2 \right), \quad k = 2, \ldots, n_{\rm train};$$

then, I choose the initial condition as follows:

$$\mathbf{a}^0_{\mu^{(1)}} = 0, \quad \mathbf{a}^0_{\mu^{(k)}} = \mathbf{a}^\star_{\mu^{({\rm ne}_k)}} \ \text{ with } \ {\rm ne}_k = \arg\min_{j=1,\ldots,k-1} \|\mu^{(j)} - \mu^{(k)}\|_2,$$

for $k = 2, \ldots, n_{\rm train}$. *In a previous implementation of the procedure, I also included box constraints in the optimization statement (cf. [TT13, section 3.1.2]) to control the sensitivity of the mapping coefficients to parameter variations;*

$$\|\mathbf{a}^\star_{\mu^{(k)}} - \mathbf{a}^0_{\mu^{(k)}}\|_\infty \leq C_\infty \|\mu^{(k)} - \mu^{({\rm ne}_k)}\|_2, \quad \text{with} \quad C_\infty = 10; \tag{3.21}$$

however, in the numerical experiments of the present work, I found that the solution to the unconstrained problem satisfied the constraints (3.21) *for all the experiments considered. I further observe that Algorithm 2 depends on several hyper-parameters. In our tests, I set* $\mathcal{S}_{n_0=1} = \mathrm{span}\{s_{\bar{\mu}}\}$, *where* $\bar{\mu}$ *is the centroid of* $\mathcal{P}$; *furthermore, I set* $n_{\max} = 6$, $tol_{\mathrm{pod}} = 5 \cdot 10^{-3}$ *and* $\texttt{tol} = 10^{-4}$.

Remark 3.2.2. ***Generalization.*** *Given the dataset* $\{(\mu^k, \mathbf{a}^{\star}_{\mu^k})\}_{k=1}^{n_{\mathrm{train}}}$ *as provided by Algorithm 2, we resort to a multi-target regression algorithm to learn a regressor* $\mu \mapsto \widehat{\mathbf{a}}_{\mu}$ *for the mapping coefficients, and ultimately define the parametric mapping*

$$\Phi : \Omega \times \mathcal{P} \to \Omega, \quad \Phi_{\mu} := \mathcal{N}(\mathbf{W}\widehat{\mathbf{a}}_{\mu}). \tag{3.22}$$

We here resort to radial basis function (RBF, [97]) approximation: other regression algorithms could also be considered. Similarly to [TT13, TT19], to avoid overfitting, we verify the statistical significance of the RBF estimators. We randomly split the dataset $\{(\mu^k, \mathbf{a}^{\star}_{\mu^k})\}_{k=1}^{n_{\mathrm{train}}}$ *into the learning and test sets* $\{(\mu^k, \mathbf{a}^{\star}_{\mu^k})\}_{k \in D_{\mathrm{learn}}}$ *and* $\{(\mu^j, \mathbf{a}^{\star}_{\mu^j})\}_{j \in D_{\mathrm{test}}}$ *with* $D_{\mathrm{learn}} \cap D_{\mathrm{test}} = \emptyset$ *and* $D_{\mathrm{learn}} \cup D_{\mathrm{test}} = \{1, \ldots, n_{\mathrm{train}}\}$ *(we here consider a* 80%-20% *learning/test split); we compute the RBF approximation* $\widehat{\mathbf{a}} : \mathcal{P} \to \mathbb{R}^m$ *based on the learning set and we compute the out-of-sample R-squared coefficient for each component:*

$$R_i^2 = 1 - \frac{\sum_{j \in D_{\mathrm{test}}} \left(\mathbf{a}^{\star}_{\mu^j} - \widehat{\mathbf{a}}_{\mu^j}\right)_i^2}{\sum_{j \in D_{\mathrm{test}}} \left(\mathbf{a}^{\star}_{\mu^j} - \bar{\mathbf{a}}\right)_i^2}, \quad \bar{\mathbf{a}} = \frac{1}{|D_{\mathrm{learn}}|} \sum_{k \in D_{\mathrm{learn}}} \mathbf{a}^{\star}_{\mu^k}, \quad i = 1, \ldots, m. \tag{3.23}$$

Then, we retain exclusively modes for which R_i^2 *is above the threshold* $R_{\min} = 0.70$.

Remark 3.2.3. ***Parametric registration based on point-set sensors.*** *The greedy procedure in Algorithm 2 is motivated by the need to construct the template space* $\mathcal{S}_n$. *If we rely on point-set sensors, we do not have to perform multiple iterations. However, we empirically found that performing two iterations of the for loop in Algorithm 2 does not hinder computational efficiency — since the cost is dominated by the high-dimensional registration problems solved during the first iteration — and has a beneficial effect on generalization outside the training set.*

3.2.6 Numerical results

I review the results presented in [TT15] for a parametric inviscid flow past an array of LS89 turbine blades.

Model problem

I consider the computational domain depicted in Figure 3.4(a); I prescribe total temperature, total pressure and flow direction at the inflow, static pressure at the outflow, non-penetration condition on the blade and periodic boundary conditions on the lower and upper boundaries. I study the sensitivity of the solution with respect to two parameters: the free-stream Mach number Ma_{∞} and the height of the channel H, $\mu = [H, \mathrm{Ma}_{\infty}]$ in the parameter domain $\mathcal{P} = [0.95, 1.05] \times [0.9, 0.95]$. I refer to [TT4] for a detailed presentation of the employed nondimensionalization, HF discontinuous Galerkin formulation and pseudo-transient continuation strategy.

Figure 3.2 shows the distribution of the Mach field for $\mu_{\min} = [0.95, 0.9]$ and $\mu_{\max} = [1.05, 0.95]$; Figure 3.3(a) shows the behavior of the Mach number on the upper side of the blade for four parameter values, while Figure 3.3(b) shows the behavior of the entropy profile $\mathrm{E} = \log(p) - \gamma \log(\rho)$ where p is the pressure field, $\gamma = 1.4$ is the ratio of specific heats, and ρ is the density field. The solution develops a normal shock on the upper side of the blade for sufficiently large values of Ma_{∞} and H; furthermore, the entropy E exhibits several peaks that correspond to the blade wakes. The solution develops two shocks at the trailing edge, which are highly undesirable for turbomachinery applications: I expect that at the trailing edge viscous effects might not be negligible; for this reason, a more thorough investigation should rely on a model that accounts for viscous effects. Note that the shock location and the entropy peaks are sensitive to the value of the parameter: this justifies the application of registration procedures.

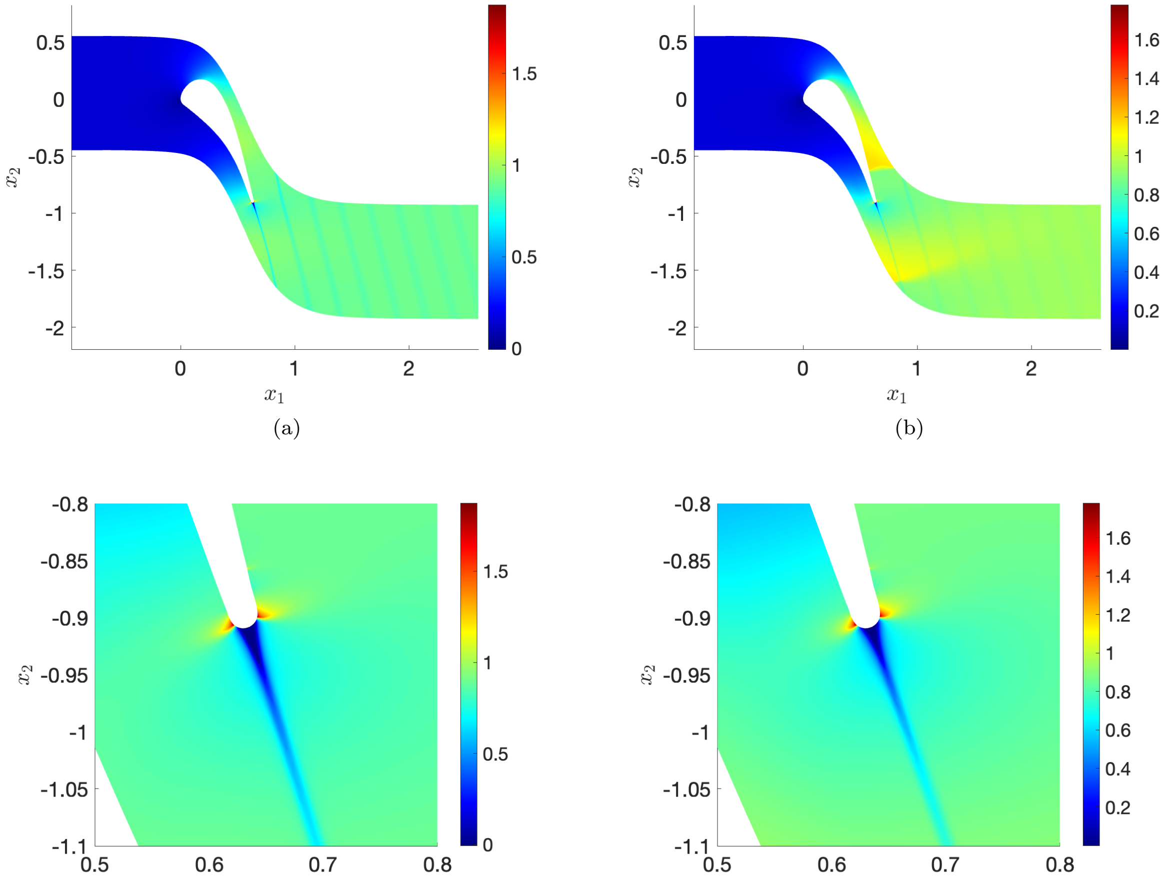

(a) (b)

(c) (d)

Figure 3.2: inviscid flow past an array of LS89 turbine blades. (a)-(b) Mach field for $\mu = [0.95, 0.9]$ and $\mu = [1.05, 0.95]$. (c)-(d) behavior in the proximity of the trailing edge.

Definition of the mapping ansatz

I consider a piecewise-smooth mapping associated with the partition in Figure 3.4(b) to deal with geometry variations . I set $H_{\rm ref} = 1$ and I define the curve $x_1 \mapsto f_{\rm btm}(x_1)$ that describes the lower boundary $\Gamma_{\rm btm}$ of the domain $\Omega = \Omega(H = 1)$; then, I define $\widetilde{H} > 0$ such that $x_1 \mapsto f_{\rm btm}(x_1) + \widetilde{H}$ and $x_1 \mapsto f_{\rm btm}(x_1) + H - \widetilde{H}$ do not intersect the blade for any $H \in [0.95, 1.05]$; finally, I define the geometric mapping

$$\Psi_H^{\rm geo}(x = [x_1, x_2]) = \left[\begin{array}{c} x_1 \\ \psi_H^{\rm geo}(x) \end{array} \right], \tag{3.24a}$$

where

$$\psi_H^{\rm geo}(x) = \begin{cases} o_1(x_1) + C(H)\,(x_2 - o_1(x_1)) & x_2 < o_1(x_1), \\ o_2(x_1) + C(H)\,(x_2 - o_2(x_1)) & x_2 > o_2(x_1), \\ x_2 & \text{otherwise}, \end{cases} \tag{3.24b}$$

with $o_1(x_1) = f_{\rm btm}(x_1) + \widetilde{H}$, $o_2(x_1) = f_{\rm btm}(x_1) + H_{\rm ref} - \widetilde{H}$ and $C(H) = \frac{H - H_{\rm ref}}{2\widetilde{H}} + 1$. Then, I consider computational maps (3.11) from the domain $\Omega = \Omega(H = H_{\rm ref})$ to $\Omega_\mu = \Omega(H)$ such that

$$\mathtt{N}(x, \mathbf{a}, \mu) = \Psi_H^{\rm geo} \circ \Psi \circ \mathtt{N}_{\rm p}(\mathbf{a}) \circ \Psi^{-1}(x), \tag{3.25}$$

for a proper choice of the mapping Ψ and the polytope $\Omega_{\rm p}$. Note that $\widetilde{\mathtt{N}}(\mathbf{a}) = \Psi \circ \mathtt{N}_{\rm p}(\mathbf{a}) \circ \Psi^{-1}$ defines a map from Ω in itself.

The polytope $\Omega_{\rm p}$ and the mapping $\Psi : \Omega_{\rm p} \to \Omega$ should be designed to ensure the periodicity constraint

$$\mathtt{N}(x + [0, H_{\rm ref}], \mathbf{a}, \mu) = \mathtt{N}(x, \mathbf{a}, \mu) + [0, H], \quad \forall\, x \in \Gamma_{\rm btm}. \tag{3.26}$$

The geometric mapping $\Psi^{\rm geo}$ satisfies the periodicity constraint; it is thus sufficient to enforce that $\widetilde{\mathtt{N}}(x + [0, H_{\rm ref}], \mathbf{a}, \mu) = \widetilde{\mathtt{N}}(x, \mathbf{a}, \mu) + [0, H_{\rm ref}]$ for all $x \in \Gamma_{\rm btm}$. Towards this end, (i) I define the polytope $\Omega_{\rm p}$ with vertices V such that $V \cap \Gamma_{\rm btm,p} = V \cap \Gamma_{\rm top,p} + [0, H_{\rm ref}]$, where $\Gamma_{\rm btm,p}, \Gamma_{\rm top,p}$ denote the lower and upper boundaries of the polytope; (ii) I define the linear mesh $\mathcal{T}_{\rm p}$ in Figure 3.4(c) with matching nodes on the periodic boundaries[1]; (iii) I define the mapping Ψ by solving a suitable optimization problem in the affine space $\widetilde{\mathcal{W}}_{\rm p} = \left\{ \texttt{id} + \varphi \in [\mathcal{X}_{\rm hf,p}]^2 : \varphi \cdot \mathbf{n}\big|_{\partial\Omega_{\rm p}\cap\partial\Omega} = 0, \;\; \varphi|_{\Gamma_{\rm btm,p}} = \varphi|_{\Gamma_{\rm top,p}} \right\}$ and I set the displacement space $\mathcal{U}_{\rm p} = \left\{ \varphi \in [\mathcal{X}_{\rm hf,p}]^2 : \varphi \cdot \mathbf{n}\big|_{\partial\Omega_{\rm p}} = 0, \;\; \varphi|_{\Gamma_{\rm btm,p}} = \varphi|_{\Gamma_{\rm top,p}} \right\}$, where $\mathcal{X}_{\rm hf,p}$ is the FE space associated with the linear mesh $\mathcal{T}_{\rm p}$ (cf. Figure 3.1(b)). The resulting curved mesh is provided in Figure 3.4(d); in the experiments, I consider polynomials of degree ten, which implies $M = 1359$. Note that, since $\widetilde{\mathcal{W}}_{\rm p}$ and $\mathcal{U}_{\rm p}$ are spaces of piecewise polynomials, it suffices to enforce the periodicity constraint at mesh nodes.

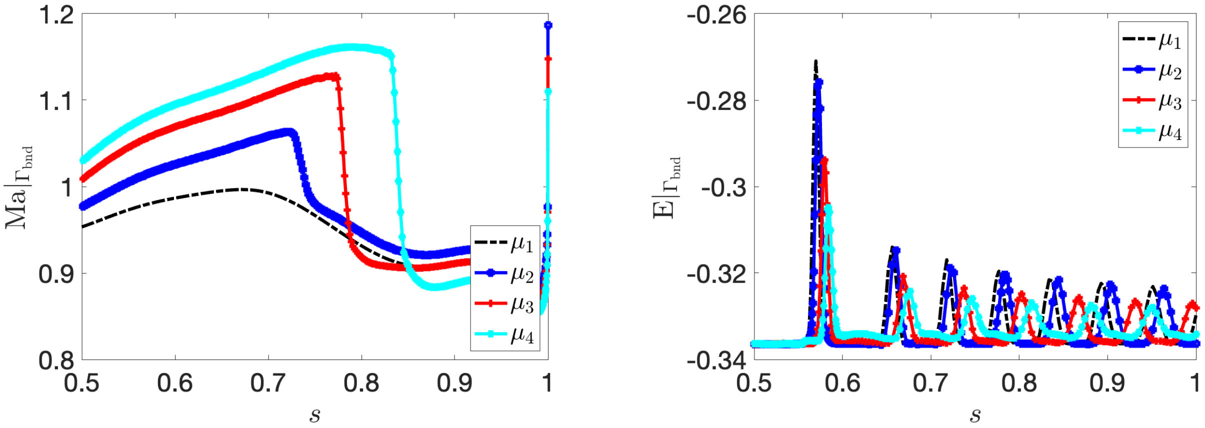

(a) (b)

Figure 3.3: inviscid flow past an array of LS89 turbine blades. (a) Mach profile over the upper side of the blade for four values of the parameter in $\mathcal{P}$. (b) entropy profile on the bottom boundary for four values of the parameter in $\mathcal{P}$. The parameter s denotes the normalized curvilinear coordinate, $s \in [0,1]$.

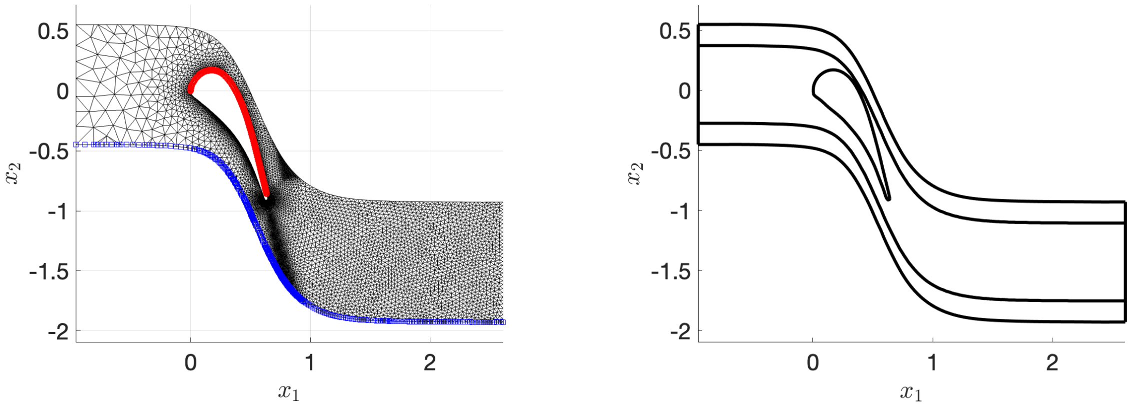

(a) (b)

Figure 3.4: inviscid flow past an array of LS89 turbine blades. (a) computational mesh $\mathcal{T}_{\rm pb}$ for DG calculations; red dots denote the nodes on the upper blade side; blue squares denote the nodes on the lower boundary. (b) partition associated with the geometric map (3.24).

Definition of the sensor

I consider a target function $\mathfrak{f}^{\rm tg}$ that combines a point-set sensor and a distributed sensor

$$\mathfrak{f}_\mu^{\rm tg} = \frac{1}{4}\sum_{i=1}^{4} \|\texttt{N}(\bar{x}_i, \mathbf{a}, \mu) - \widehat{x}_{i,\mu}\|_2^2 + \min_{\nu \in \mathcal{S}_n} \int_{\Omega_{\rm p}} \left| s_\mu \circ \texttt{N}_{\rm p}(\mathbf{a}) - \nu \right|^2 J(\Psi)\, dx, \tag{3.27}$$

where the distributed sensor s_μ is obtained from the Mach field, the template space $\mathcal{S}_n$ is built adaptively using Algorithm 2, and the salient points $\{\widehat{x}_{i,\mu}\}_i$ correspond to the first three peaks of the entropy profile on the lower boundary (cf. Figure 3.3(b)) and the shock location on the upper boundary (cf. Figure 3.3(a)).

---

[1] The same condition is enforced in the HF mesh.

I identify the entropy peaks by computing the local maxima of the entropy profile on $\Gamma_{\mathrm{btm},\mu}$. I detect the shock location on the upper blade side using the following procedure: first, I compute the mean values $\{\overline{\mathrm{Ma}}_j\}_j$ and $\{\overline{d\mathrm{Ma}}_j\}_j$ of the Mach number and its tangential derivative on each facet $\{\mathtt{F}_j\}_j$ of the select boundary; second, I find the index $j^\star$ such that $\overline{\mathrm{Ma}}_{j^\star} > 1 > \overline{\mathrm{Ma}}_{j^\star+1}$ and $\overline{d\mathrm{Ma}}_{j^\star} < -\frac{10^{-2}}{|\mathtt{F}_{j^\star}|}$ and I return the estimate $x_{\mathrm{shk},\mu}^{\mathrm{raw}}$ equal to the midpoint of the selected facet.

Given the raw estimates $\{x_{i,\mu}^{\mathrm{raw}} : i = 1, \ldots, 4, \mu \in \mathcal{P}_{\mathrm{train}}\}$ of the point sensors, I apply radial basis function (RBF) regression to find smoother estimates that facilitate the generalization step (cf. Remark 3.2.2); in order to ensure that the points are on the boundary, I apply RBF to the curvilinear coordinates of the points. As shown in Figure 3.3(a), the solution does not exhibit any shock for several parameter values; I do not consider these points to train the RBF surrogate, and I rely on the surrogate itself to find a fictitious estimate of $\widehat{x}_{\mathrm{shk},\mu}$ for all $\mu \in \mathcal{P}$.

Performance of the registration procedure

I apply Algorithm 2 based on a regular 11×6 grid of parameters $\mathcal{P}_{\mathrm{train}}$. Figure 3.5 compares the location of the sensors $\{\widetilde{x}_{i,\mu} = (\Psi_H^{\mathrm{geo}})^{-1}(\widehat{x}_{i,\mu}) : i = 1, \ldots, 4, \mu \in \mathcal{P}_{\mathrm{train}}\}$ and their mapped counterparts $\{\widetilde{x}_{i,\mu}' = \Phi_\mu^{-1}(\widetilde{x}_{i,\mu}) : i = 1, \ldots, 4, \mu \in \mathcal{P}_{\mathrm{train}}\}$; similarly, Figure 3.6 reproduces the results in Figure 3.3 for the mapped solution field. I observe that the peaks of the mapped entropy field on Γ_{btm} and the shock on the upper side of the blade are nearly insensitive to the parameter value. For all in-sample and out-of-sample configurations considered, the quality of the deformed mesh — which is measured by (3.15d) — is comparable with the one of the original mesh.

Model reduction

I rely on POD+regression to estimate the solution field. POD solution coefficients are estimated using the same RBF regression method that is employed for the mapping coefficients (cf. Remark 3.2.2). To assess performance, I consider a dataset of $n_{\mathrm{test}} = 20$ randomly-selected parameters $\mathcal{P}_{\mathrm{test}}$ and I compute the L^2 maximum relative errors

$$E_{\max} = \max_{\mu \in \mathcal{P}_{\mathrm{test}}} \frac{\|\widehat{u}_\mu - u_\mu^{\mathrm{hf}}\|_{L^2(\Omega_\mu)}}{\|u_\mu^{\mathrm{hf}}\|_{L^2(\Omega_\mu)}}, \quad E_{\max}^{\mathrm{bnd}} = \max_{\mu \in \mathcal{P}_{\mathrm{test}}} \frac{\|\widehat{u}_\mu - u_\mu^{\mathrm{hf}}\|_{L^2(\Gamma_{\mathrm{bld}})}}{\|u_\mu^{\mathrm{hf}}\|_{L^2(\Gamma_{\mathrm{bld}})}}, \tag{3.28}$$

where Γ_{bld} denotes the boundary of the blade. Figure 3.7 shows the results for the "linear" ROM and the "registered" ROM — both approaches involve the application of a geometric mapping; the difference is that for the linear ROM the mapping is chosen a priori and corresponds to Ψ^{geo} (3.24), while for the registered ROM the mapping is chosen through the registration procedure discussed above. Both linear and registered ROMs reach a plateau for $n \approx 10$ due to the limited amount of datapoints. I observe that registration improves performance by a factor 2.04 for the global error and a factor 8.04 for the error on the blade, for the same amount of HF data.

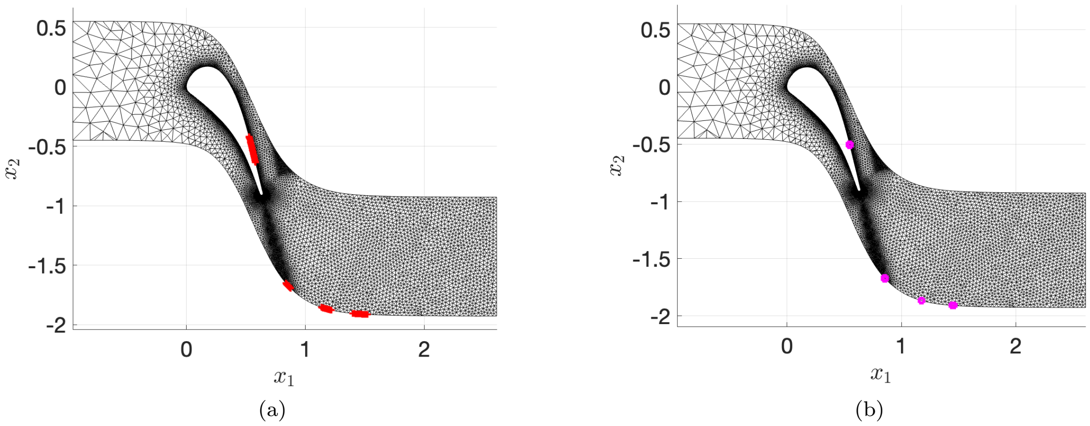

Figure 3.5: inviscid flow past an array of LS89 turbine blades. (a) sensor points used in the registration procedure for $n_{\mathrm{train}} = 66$ configurations. (b) mapped sensor points.

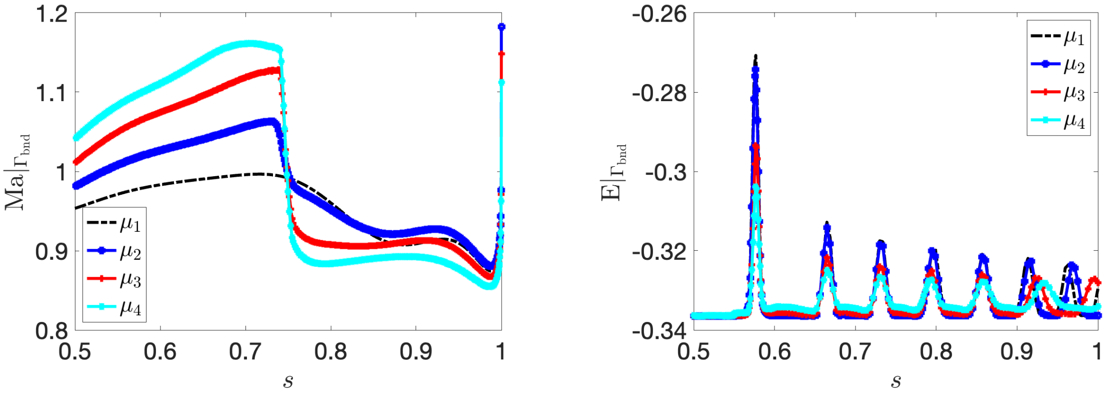

(a) (b)

Figure 3.6: inviscid flow past an array of LS89 turbine blades. (a) mapped Mach profile over the upper side of the blade for four values of the parameter in $\mathcal{P}$. (b) mapped entropy profile on the bottom boundary for four values of the parameter in $\mathcal{P}$. Unmapped profiles are shown in Figure 3.3.

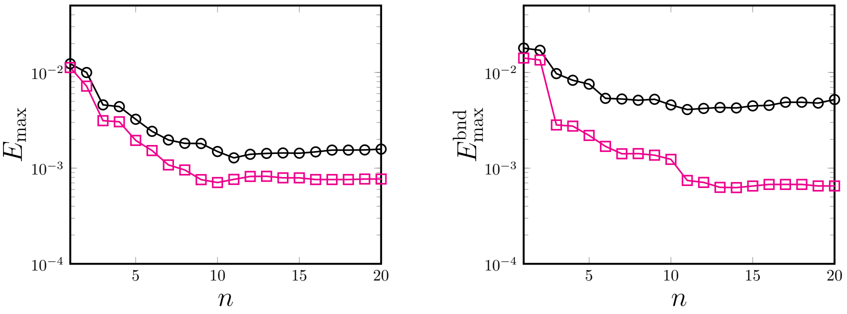

(a) (b)

Figure 3.7: inviscid flow past an array of LS89 turbine blades; model reduction. Behavior of the out-of-sample errors (3.28) for the linear ROM ─○─ and the registered ROM ─□─ for $n_{\mathrm{train}} = 66$ and several values of n.

3.3 Application to projection-based model reduction

In order to devise effective ROMs for advection-dominated parametric problems, we should integrate the registration procedure of section 3.2 into the MOR offline-online framework outlined in Algorithm 1. In [TT4], I recently proposed, in collaboration with Barral and Tifouti, a general procedure to adaptively build the HF mesh, the parametric mapping, and the ROM. The Journal article [TT4] is the first scientific output of the Inria Exploratory Action "*Adaptive meshes for model order reduction*" (AM2OR); the project, which is led by Dr. Barral and me, aims to combine mesh adaptation (MA) and projection-based MOR for parametric problems.

3.3.1 Methodology

The Lagrangian approximation (3.1) is constructed using the procedure described in Algorithm 3. Given an initial mesh $\mathcal{T}_{\mathrm{hf}}^{(0)}$ of Ω and the training set $\mathcal{P}_{\mathrm{train}} = \{\mu^k\}_{k=1}^{n_{\mathrm{train}}} \subset \mathcal{P}$, the method returns an HF mesh $\mathcal{T}_{\mathrm{hf}}$, a low-rank mapping Φ, a ROB Z and a ROM for the generalized coordinates $\widehat{\boldsymbol{\alpha}}$ (cf. (3.1)) based on an iterative procedure that comprises four distinct steps.

1. Snapshot generation: $(\mathcal{T}_{\mathrm{hf}}, \Phi, \mathcal{P}_{\mathrm{train}}) \to \left\{u_\mu^{\mathrm{hf}} \, : \, \mu \in \mathcal{P}_{\mathrm{train}}\right\}$. We generate snapshots of the solution field for all values of the parameter μ in $\mathcal{P}_{\mathrm{train}}$ based on the parametric mesh $\mu \mapsto \Phi_\mu(\mathcal{T}_{\mathrm{hf}})$.
2. Mesh adaptation: $\left\{u_\mu^{\mathrm{hf}} \circ \Phi_\mu : \mu \in \mathcal{P}_{\mathrm{train}}\right\} \to \mathcal{T}_{\mathrm{hf}}$. We exploit the available set of snapshots to generate an accurate yet parsimonious mesh for the elements of the mapped manifold $\widetilde{\mathcal{M}}$.
3. Registration: $\left(\left\{u_\mu^{\mathrm{hf}} \, : \, \mu \in \mathcal{P}_{\mathrm{train}}\right\}, \ \mathcal{T}_{\mathrm{hf}}\right) \to \Phi$. We exploit the available set of snapshots to find a parametric mapping Φ that tracks coherent, parameter-dependent structures of the solution field. The method should ensure that the deformed mesh $\Phi_\mu(\mathcal{T}_{\mathrm{hf}})$ is a proper mesh of Ω for all $\mu \in \mathcal{P}$.

4. Linear-subspace model reduction: $(\mathcal{T}_{\rm hf}, \Phi, \mathcal{P}_{\rm train}) \to (Z, {\rm ROM})$. We apply linear-subspace MOR to determine the low-rank expansion $\mu \mapsto \widetilde{u}_\mu$, that is we build the ROB Z and the ROM for $\mu \mapsto \widehat{\boldsymbol{\alpha}}_\mu$.

Algorithm 3 : adaptive training procedure.

```
1: Initialization: define the mesh $\mathcal{T}_{\rm hf}^{(0)} = \mathcal{T}_{\rm hf}^{(1)}$, the mapping $\Phi^{(0)} = {\tt id}$ (identity map), and the training set $\mathcal{P}_{\rm train} = \{\mu^k\}_{k=1}^{n_{\rm train}} \subset \mathcal{P}$.
2: for $k = 1, \ldots, N_{\rm it}$ do
3:     Snapshot generation    $\left(\mathcal{T}_{\rm hf}^{(k-1)}, \Phi^{(k-1)}, \mathcal{P}_{\rm train}\right) \to \left\{u_\mu^{{\rm hf},(k)} \, : \, \mu \in \mathcal{P}_{\rm train}\right\}$.
4:     if $k > 1$ then
5:         Mesh adaptation    $\left\{u_\mu^{{\rm hf},(k)} \circ \Phi_\mu^{(k-1)} : \mu \in \mathcal{P}_{\rm train}\right\} \to \mathcal{T}_{\rm hf}^{(k)}$.
6:     end if
7:     Registration    $\left(\left\{u_\mu^{{\rm hf},(k)} \, : \, \mu \in \mathcal{P}_{\rm train}\right\}, \ \mathcal{T}_{\rm hf}^{(k)}\right) \to \Phi^{(k)}$.
8:     Linear-subspace model reduction    $\left(\mathcal{T}_{\rm hf}^{(k)}, \, \Phi^{(k)}, \, \mathcal{P}_{\rm train}\right) \ \to \left(Z^{(k)}, {\rm ROM}^{(k)}\right)$.
9: end for
```

In [TT4], we rely on a previous implementation of the parametric registration procedure discussed in section 3.2, and on LSPG projection and empirical quadrature to devise the ROM (cf. Chapter 2); finally, we rely on metric-based mesh adaptation [59, 60]. Metric-based MA aims to generate a *unit mesh* [59] with respect to a suitable metric field associated with the solution. For one-dimensional problems, we consider the standard de Boor's algorithm (see, e.g., [47, Chapter 2]); for two-dimensional problems, we consider two different strategies: a standard isotropic *mark-then-refine* MA strategy driven by the total enthalpy error, and an Hessian-based approach based on the Mach number and on metric intersection [9, 10] to devise a common metric for the entire snapshot set. For two-dimensional problems we rely on the open-source mesh adaptation toolkit `mmg2d` ([5, 27]) to generate adapted meshes from a (possibly anisotropic) metric $\mathfrak{M}$.

3.3.2 Acceleration

Each iteration of Algorithm 3 generates a large amount of data about the parametric problem, which can be used to speed up offline computations. In [TT4], we identified computational bottlenecks of the training phase and we discussed actionable strategies to reduce the computational burden. The acceleration strategy was further developed and extended in [TT3].

- The construction of the snapshot set for registration (cf. Line 3, Algorithm 3) based on the HF model is prohibitively expensive. Instead, we propose to rely on the ROM built at the previous iteration; for the first iteration, we first execute the weak-greedy algorithm [94] and then we use the ROM to generate the dataset of simulations.

- The GNM for (2.20) is sensitive to the choice of the initial condition. In our implementation, we initialize GNM based on nearest-neighbor regression which is clearly highly inaccurate for modest values of n. To face this issue, we propose to rely on a large dataset of initial conditions defined as follows:

$$\left\{\widehat{\boldsymbol{\alpha}}_\mu^0 : \mu \in \mathcal{P}_{\rm train}\right\} \quad \text{where} \ \ \widehat{\boldsymbol{\alpha}}_\mu^0 = \arg \min_{\boldsymbol{\alpha} \in \mathbb{R}^n} \ \| Z\boldsymbol{\alpha} - \widehat{u}_\mu^{\rm old} \circ \Phi_\mu^{-1} \|. \tag{3.29}$$

  Note that the fields $\{\widehat{u}_\mu^{\rm old} : \mu \in \mathcal{P}_{\rm train}\}$ are generated for registration (cf. Line 3, Algorithm 3); nevertheless, cost of (3.29) is significant due to the need to compute the composition of $\widehat{u}_\mu^{\rm old}$ with Φ_μ^{-1} — which requires mesh interpolation. In practice, we estimate the L^2 norm $\|\cdot\|$ in (3.29) using 10^3 randomly-sampled points in Ω to reduce offline costs.

- The pseudo-transient continuation (PTC) strategy employed to solve the HF problem might require many iterations to reach convergence. To reduce the computational burden, we initialize the PTC solver with the reduced-order solution $\widehat{u}_\mu$ from the previous iteration, as opposed to the free-stream solution. Thanks to this choice, we can consider a much larger initial CFL number[2] without experiencing any stability issue.

- The registration procedure discussed in section 3.2 relies on multiple solutions to a nonlinear non-convex optimization problem of size $m = \mathcal{O}(10^3)$ that is sensitive to the initial condition. In our experience, the initialization strategy reviewed in section 3.2 (cf. Remark 3.2.1) leads to accurate performance; however, it

---

[2] In the numerical experiments, we set ${\rm CFL}_0 = 100$ instead of ${\rm CFL}_0 = 1$; see [100, section II.B].

requires a sufficiently dense discretization of $\mathcal{P}$ and is not parallelizable. To address this issue, we propose to store the mapping coefficients $\{\widehat{\mathbf{a}}_\mu : \mu \in \mathcal{P}_{\rm train}\}$ obtained during the first iteration of the registration method and then use them as initial conditions for the registration algorithm in the subsequent outer-loop iteration: note that for this choice of the initialization the solution to the problems (3.8) in Algorithm 2 can be trivially parallelized; in addition, we can potentially cope with much coarser discretizations of $\mathcal{P}$.

- The weak-greedy algorithm requires multiple constructions of the ROM and might hence be expensive; in addition, it cannot be efficiently parallelized. To address this issue, we initialize the greedy method with the parameters $\{\mu^{\star,i}\}_{i=1}^{n_0}$ obtained by applying the strong-greedy algorithm (see, e.g., [78, section 7.3]) to the snapshot set generated for registration (cf. Line 3, Algorithm 3). Since the snapshot set is generated using the ROM, the strong-greedy algorithm can be applied to the generalized coordinates.

3.3.3 Numerical results

In [TT4], we considered the application of Algorithm 3 to a quasi-1D nozzle problem and a two-dimensional transonic inviscid flow past a bump. We assess performance based on $n_{\rm test} = 20$ out-of-sample parameters $\mathcal{P}_{\rm test} = \{\mu_{\rm test}^j\}_{j=1}^{n_{\rm test}}$ with $\mu_{\rm test}^1, \ldots, \mu_{\rm test}^{n_{\rm test}} \overset{\rm iid}{\sim} {\rm Uniform}(\mathcal{P})$; for each $\mu \in \mathcal{P}_{\rm test}$, we report the HF L^2 error $E_\mu^{\rm hf}$, the sub-optimality index $\eta_\mu^{\rm hf}$ and the total enthalpy error E_μ^∞ such that

$$E_\mu^{\rm hf} = \frac{\| u_\mu^{\rm hf} - \widehat{u}_\mu^{\rm hf} \|_{L^2(\Omega_\mu)}}{\| q_\mu^{\rm hf} \|_{L^2(\Omega_\mu)}}, \tag{3.30}$$

$$\eta_\mu^{\rm hf} = \frac{\| u_\mu^{\rm hf} - \widehat{u}_\mu^{\rm hf} \|_{L^2(\Omega_\mu)}}{\min_{\zeta \in \mathcal{Z}} \| u_\mu^{\rm hf} - \zeta \circ \Phi_\mu^{-1} \|_{L^2(\Omega_\mu)}}, \tag{3.31}$$

$$E_\mu^{\infty} = \frac{\| H_{{\rm tot},\mu}^{\rm true} - \widehat{H}_{{\rm tot},\mu} \|_{L^2(\Omega_\mu)}}{\| H_{{\rm tot},\mu}^{\infty} \|_{L^2(\Omega_\mu)}}, \tag{3.32}$$

where $H_{\rm tot}$ denotes the total enthalpy, which is constant over all the domain. The relative error $E_\mu^{\rm hf}$ measures the accuracy of the reduced-order estimate with respect to the HF model employed for training — it is hence a measure of the overall ability of the MOR procedure to approximate the truth model of the PDE. The suboptimality index $\eta_\mu^{\rm hf}$ measures the extent to which the LSPG projection scheme is suboptimal compared to the best-fit error: it hence allows to directly evaluate the effectiveness of the ROM, which encompasses the choice of the test space, initialization, and hyper-reduction. Finally, the total enthalpy error (3.32) measures the accuracy of the state estimate with respect to the exact solution to the PDE, in terms of enthalpy preservation. Simulations are performed in Matlab 2022a [66] based on an in-house code, and executed over a commodity Linux workstation (RAM 32 GB, Intel i7 CPU 3.20 GHz x 12).

Figure 3.8 illustrates the performance of the ROM over the test set for $N_{\rm it} = 3$ iterations of Algorithm 3 without acceleration, for the nozzle flow test case. We initialize the algorithm using an uniform HF grid with $N_{\rm e} = 60$ triangles and quadratic ($\mathtt{p} = 2$) polynomials; then, we increase the size of the mesh by a factor 1.5 at each iteration: this implies that the generated HF meshes have $N_{\rm e} = 60$, $N_{\rm e} = 90$ and $N_{\rm e} = 135$ elements at iterations one, two and three, respectively. I refer to [TT4] for a detailed description of the test. Figure 3.8 shows the performance of the ROM. Figure 3.8(a) shows the relative error over the test set, which mildly depends on the size of the mesh. Figure 3.8(b) shows the suboptimality index: interestingly, we observe that the performance of the projection scheme deteriorates as we increase the size of the mesh: we plan to investigate this behavior in a subsequent work; nevertheless, we observe that $\eta_\mu^{\rm hf} \lesssim 10$ for all numerical experiments. Figure 3.8(c) shows the total enthalpy error: as expected, the error decreases as we increase the size of the mesh. Figure 3.8(d) shows the wall-clock online cost: thanks to hyper-reduction, results do not depend on the size of the underlying mesh but they clearly depend on the size n of the ROB.

Figure 3.9 replicates the results in Figure 3.8 for the transonic bump problem; we here study the performance of the standard (without acceleration) approach based on isotropic mesh adaptation based on a mark-then-refine paradigm driven by the total enthalpy error. The ROM achieves accurate performance over the test set with respect to the HF estimate for all three iterations: results are hence in good agreement with the selected tolerance ($\mathtt{tol} = 10^{-3}$) of the weak-greedy algorithm. The suboptimality index ranges from one to three for all experiments: this indicates that our projection scheme is extremely effective for this model problem. The total enthalpy error decreases as we increase the size of the mesh, while the computational cost is nearly the same for all iterations.

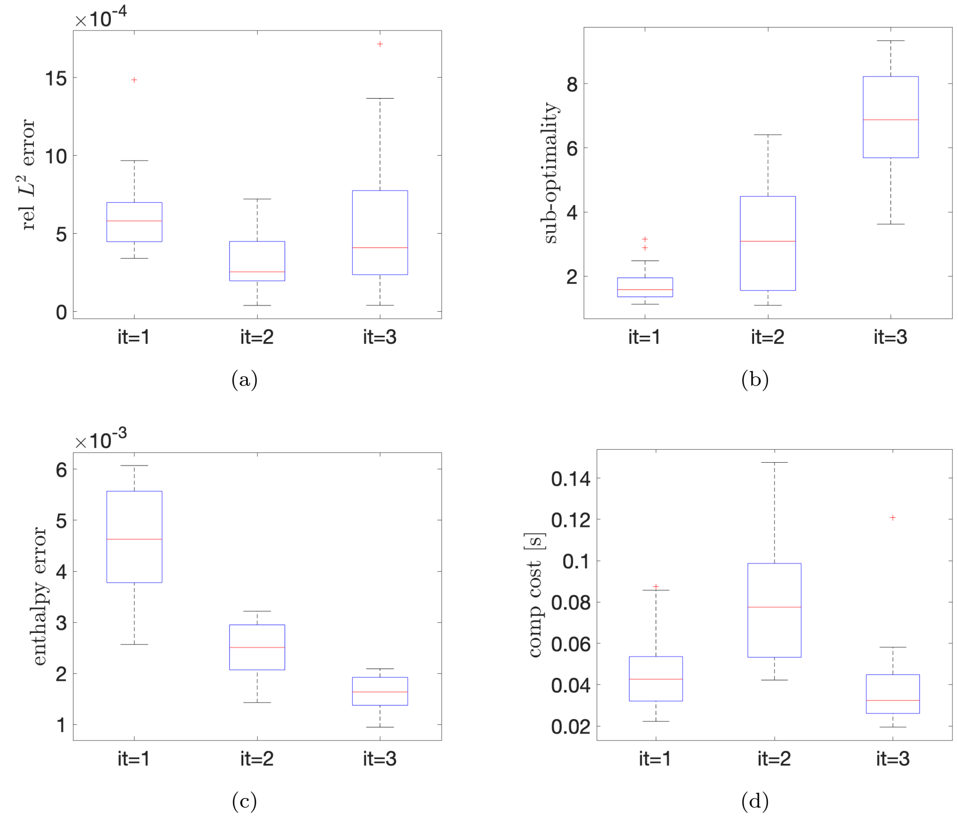

(a) (b)

(c) (d)

Figure 3.8: nozzle flow. Performance of the ROM for three iterations of the adaptive (basic) procedure.

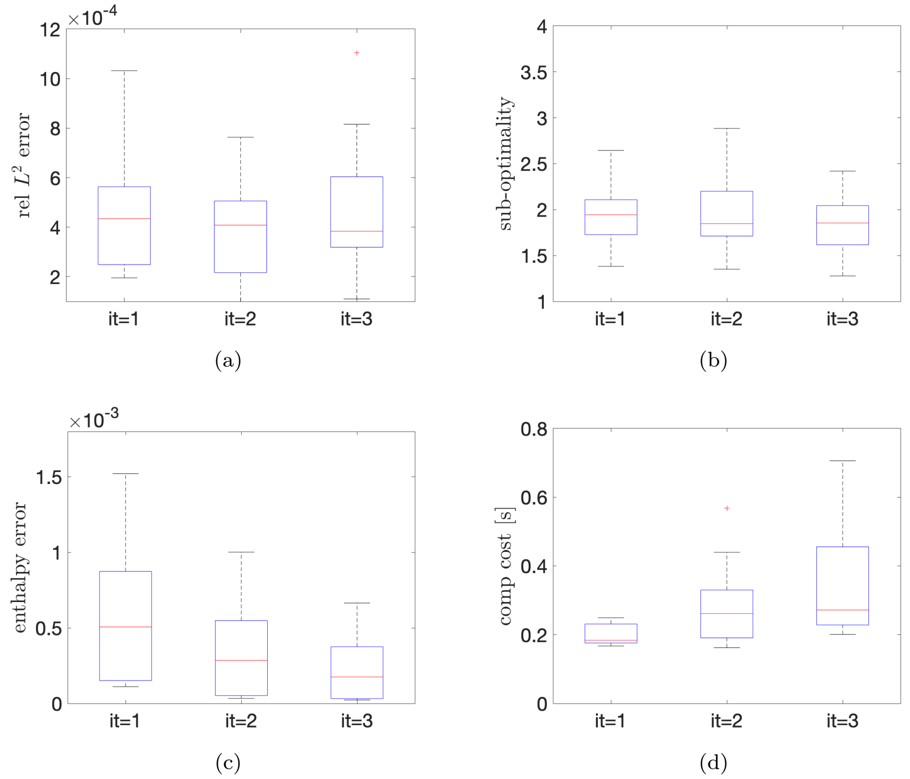

(a) (b)

(c) (d)

Figure 3.9: transonic bump. Performance of the ROM for three iterations of the adaptive (basic) procedure.

In Figure 3.10, we investigate the effect of registration on solution manifold compressibility and mesh adaptation for the nozzle flow test case. Towards this end, we consider the adaptive reduced-order and HF models associated with the third iteration of Algorithm 3, with a HF model defined over a Cartesian "static" mesh with the same number of elements, $N_{\rm e} = 135$. First, in Figure 3.10(a), we compare the behavior of the normalized

POD eigenvalues associated with the snapshot set in physical ("unreg") and reference ("reg") configurations. We observe that registration significantly improves the convergence of the POD eigenvalues that can be regarded as a "proxy" of the linear complexity of the corresponding solution manifold. Figure 3.10(b) shows the behavior of the error in total enthalpy for the final registered ROM and the static HF model based on an uniform mesh: we clearly notice that the HF model — which has the same number of degrees of freedom as the HF model used to generate the ROM — is significantly less accurate than the adapted ROM. Finally, Figure 3.10(c) shows the behavior of the mesh density $h : \Omega \to \mathbb{R}_+$ such that $h|_{\mathtt{D}_k} = |\mathtt{D}_k|$ for the sequence of meshes generated during Algorithm 3: we observe that registration allows us to refine the mesh over a very narrow portion of the computational domain and hence enables significant computational savings.

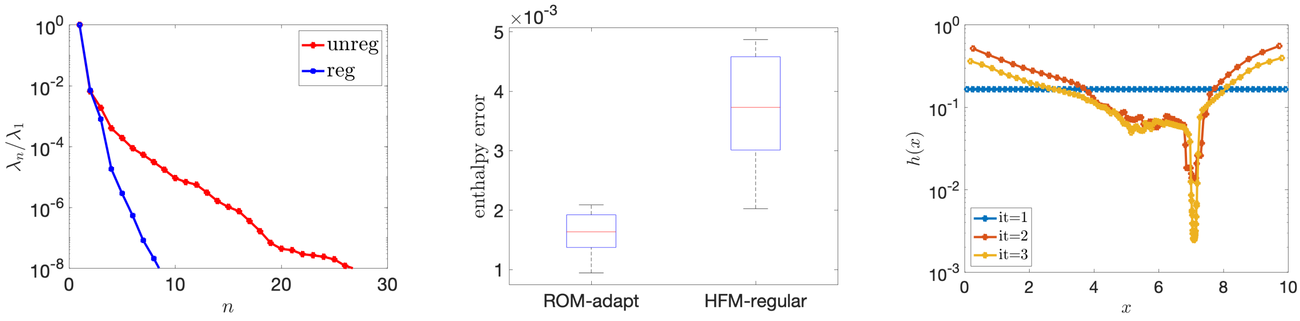

(a) (b) (c)

Figure 3.10: nozzle flow. Effect of registration on compressibility and mesh adaptation. (a) POD eigenvalues in reference and physical configurations. (b) total enthalpy error for registered ROM and unregistered HFM on regular mesh with $N_{\rm e} = 135$ elements. (c) mesh density $h : \Omega \to \mathbb{R}_+$, $h|_{\mathtt{D}_k} = |\mathtt{D}_k|$ for the sequence of considered meshes.

For the transonic bump problem, we execute three iterations of Algorithm 3 with metric-based anisotropic mesh adaptation based on the Hessian of the Mach number. As discussed in detail in [TT4], we initially set the parameter N that controls the number of nodes equal to 750 and we increase it at each iteration by a factor 1.5: we obtain meshes with $N_{\rm e} = 3448$, $N_{\rm e} = 4440$, $N_{\rm e} = 6389$ for the first, second and third iteration of Algorithm 3, respectively. Figure 3.11 shows the sequence of meshes generated by Algorithm 3. We observe that the meshes are nearly isotropic in the proximity of the shock while they exhibit elongated elements in the downstream region (the minimum radius ratio is roughly 0.05). We notice that the adapted mesh for a single field is significantly more anisotropic in the proximity of the shock, but it becomes less and less anisotropic as we combine metrics associated with different parameters. This is likely due to the fact that the shock is not sharply tracked in the reference configuration.

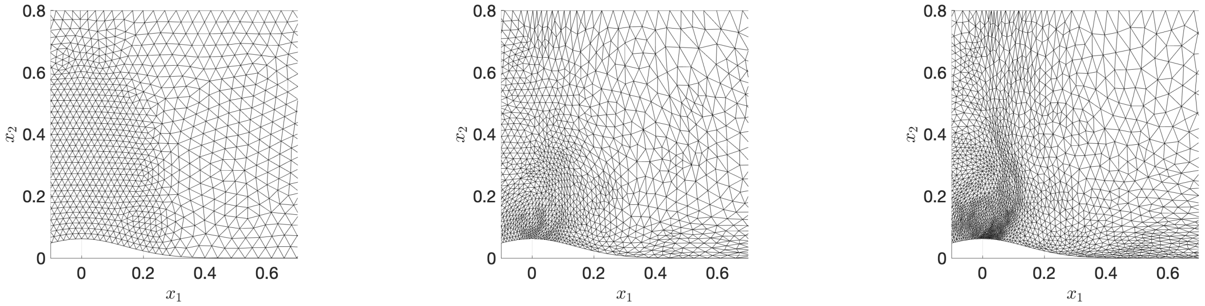

(a) $it = 1$ (b) $it = 2$ (c) $it = 3$

Figure 3.11: transonic bump. Visualization of the reference mesh in the proximity of the bump, for three iterations of the adaptive algorithm (accelerated) with anisotropic mesh adaptation ($N_{\rm e} = 3448$, $N_{\rm e} = 4440$, $N_{\rm e} = 6389$).

Table 3.1 provides an overview of the performance of the adaptive procedure for the transonic bump test case, with and without acceleration and for both isotropic and anisotropic mesh adaptation. I observe that the three approaches lead to ROMs of comparable accuracy; however, the acceleration strategy is able to reduce the offline costs by a factor 1/3.

	L^2 error (avg)			enthalpy error (avg)		
	1	2	3	1	2	3
Basic (Isotropic MA)	$0.53 \cdot 10^{-3}$	$0.44 \cdot 10^{-3}$	$0.48 \cdot 10^{-3}$	$0.58 \cdot 10^{-3}$	$0.35 \cdot 10^{-3}$	$0.23 \cdot 10^{-3}$
Accelerated (Isotropic MA)	$0.29 \cdot 10^{-3}$	$0.31 \cdot 10^{-3}$	$0.49 \cdot 10^{-3}$	$0.59 \cdot 10^{-3}$	$0.37 \cdot 10^{-3}$	$0.23 \cdot 10^{-3}$
Accelerated (Anisotropic MA)	$0.29 \cdot 10^{-3}$	$0.36 \cdot 10^{-3}$	$0.50 \cdot 10^{-3}$	$0.59 \cdot 10^{-3}$	$0.36 \cdot 10^{-3}$	$0.26 \cdot 10^{-3}$

	ROB size			online cost (avg)			offline cost
	1	2	3	1	2	3	
Basic (Isotropic MA)	14	17	19	0.20	0.28	0.36	03:24:13
Accelerated (Isotropic MA)	18	17	21	0.25	0.25	0.36	02:11:47
Accelerated (Anisotropic MA)	18	17	16	0.26	0.26	0.24	01:58:48

Table 3.1: comparison of the performance of the basic accelerated adaptive procedures with isotropic and anisotropic mesh adaptation.

3.4 Application to non-intrusive model reduction

In [TT10], Iollo and I developed a non-intrusive nonlinear MOR technique dubbed *convex displacement interpolation* (CDI) that relies on coordinate transformation to devise accurate state predictions for parametric fields with compactly-supported features. Similarly to Lagrangian approaches, CDI relies on the assumption that the location of coherent features of the solution field depends smoothly on the parameter; however, unlike in (3.1), it does not rely on the definition of a reference configuration where the location of the coherent features is (approximately) freezed. The approach of [TT10] was proposed for databases of two snapshots and one-dimensional parameter domains; in [TT5] we extended with Cucchiara and Telib the approach to deal with multiple snapshots and higher-dimensional parameter domains.

3.4.1 Methodology

CDI exploits the standard offline/online decomposition to predict the state map $\mu \in \mathcal{P} \mapsto u_\mu \in \mathcal{M}$; Algorithm 4 summarizes the general procedure and highlights the key steps of the methodology. Given the solution manifold $\mathcal{M}$, we introduce the training set $\mathcal{P}_{\rm train} = \{\mu^k\}_{k=1}^{n_{\rm train}} \subset \mathcal{P}$ and the dataset of solutions $\mathcal{D}_{\rm train} = \{u_\mu : \mu \in \mathcal{P}_{\rm train}\}$. During the offline stage, for each element of $\mathcal{D}_{\rm train}$, we determine a set of points $X_\mu^{\rm raw} = \{x_{i,\mu}^{\rm raw}\}_{i=1}^{N_\mu} \subset \overline{\Omega}$ that describe local features of the solution field that we wish to track: note that the sets $\{X_\mu^{\rm raw} : \mu \in \mathcal{P}_{\rm train}\}$ do not necessarily have the same number of elements and are not matched with each other. Then, we define the reference points $X^{\rm ref} := \{x_i^{\rm ref}\}_{i=1}^N$ and the new sensors $X_\mu := \{x_{i,\mu} = x_i^{\rm ref} + v_{i,\mu}\}_{i=1}^N$ such that the set X_μ approximates (cf. (3.5)) $X_\mu^{\rm raw}$ for all $\mu \in \mathcal{P}_{\rm train}$ — here $\{v_{i,\mu}\}_{i=1}^N$ denote a set of properly-chosen displacements of the reference points. During the online stage, given the new parameter value $\mu \notin \mathcal{P}_{\rm train}$, first, we apply a regression method to predict the new sensor locations $\widehat{X}_\mu = \{\widehat{x}_{i,\mu} = x_i^{\rm ref} + \widehat{v}_{i,\mu}\}_{i=1}^N$; second, we identify a set of κ nearest neighbors $\mathcal{P}_{\rm nn}^\mu = \{\nu^i\}_{i=1}^\kappa \subset \mathcal{P}_{\rm train}$; third, we define the mappings $\{\Phi_\nu : \nu \in \mathcal{P}_{\rm nn}^\mu\}$ such that each mapping Φ_ν is bijective in Ω and $\Phi_\nu(\widehat{x}_{i,\mu}) \approx \widehat{x}_{i,\nu}$ for $i = 1, \ldots, N$ and $\nu \in \mathcal{P}_{\rm nn}^\mu$; fourth, we return the (generalized) CDI as

$$\widehat{u}_\mu = \sum_{\nu \in \mathcal{P}_{\rm nn}^\mu} \omega_\mu^\nu \widetilde{u}_\nu, \quad \text{where } \widetilde{u}_\nu = u_\nu \circ \Phi_\nu, \tag{3.33}$$

for a proper choice of the weights $\{\omega_\mu^\nu : \nu \in \mathcal{P}_{\rm nn}^\mu\}$. Figure 3.12 illustrates the computational procedure for a simple one-dimensional problem.

Algorithm 4 : offline/online decomposition.

```
Offline stage                                                         performed once
  1: Generate the dataset $\mathcal{D}_{\rm train} = \{u_\mu : \mu \in \mathcal{P}_{\rm train}\}$.
  2: Identify the point clouds $\{X_\mu^{\rm raw} : \mu \in \mathcal{P}_{\rm train}\}$.
  3: Define the template set $X^{\rm ref}$ and the sorted point clouds $\{X_\mu : \mu \in \mathcal{P}_{\rm train}\}$.
Online stage                                                 performed for any $\mu \in \mathcal{P}$
  1: Estimate the new points $\widehat{X}_\mu = \{\widehat{x}_{i,\mu}\}_{i=1}^N$.
  2: Select the neighboring parameters $\mathcal{P}_{\rm nn}^\mu = \{\nu^i\}_{i=1}^\kappa \subset \mathcal{P}_{\rm train}$.
  3: Compute the mappings $\Phi_\nu$ based on $\widehat{X}_\mu$ and $\widehat{X}_\nu$ for all $\nu \in \mathcal{P}_{\rm nn}^\mu$.
  4: Compute the weights $\{\omega_\mu^\nu : \nu \in \mathcal{P}_{\rm nn}^\mu\}$ and return the estimate (3.33).
```

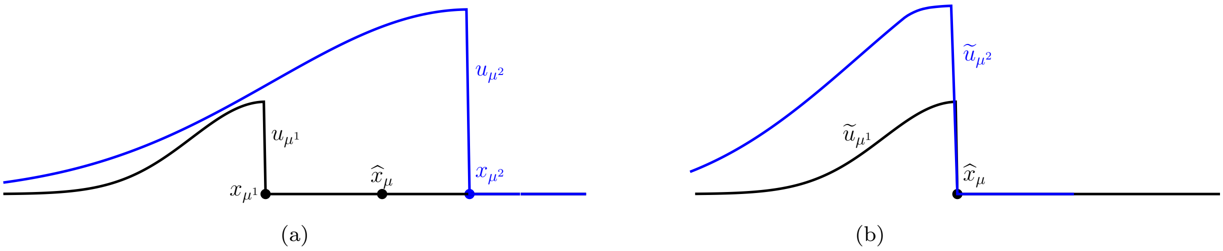

Figure 3.12: schematic of the CDI procedure. (a) dataset of snapshots $\{u_{\mu^1}, u_{\mu^2}\}$ and corresponding sensors (shock location), $\widehat{x}_\mu$ denotes the predicted shock location for the parameter μ. (b) mapped snapshots $\{\widetilde{u}_{\mu^1}, \widetilde{u}_{\mu^2}\}$ in (3.33).

The CDI procedure outlined in Algorithm 4 generalizes the method in [TT10]: in more detail, if we consider $\mathcal{P}_{\rm train} = \mathcal{P}_{\rm nn}^\mu = \{\mu^0, \mu^1\}$, $\omega_\mu^{\mu^0} = 1 - \frac{\|\mu-\mu^i\|_2}{\|\mu^1-\mu^0\|_2}$, $\omega_\mu^{\mu^1} = \frac{\|\mu-\mu^i\|_2}{\|\mu^1-\mu^0\|_2}$, and a proper choice of the mappings $\Phi_{\mu^0}, \Phi_{\mu^1}$, the estimate (3.33) reduces to the original CDI approach. I observe that, similarly to Lagrangian approximations, CDI relies on geometric mappings to track local features of the solution field and ultimately improve state predictions; on the other hand, CDI does not rely on the definition of a reference domain and the estimate is inherently Eulerian. I note that the definition of the template $X^{\rm ref}$ is instrumental to the construction of the sorted point clouds $\{X_\mu : \mu \in \mathcal{P}_{\rm train}\}$, which enable the application of standard regression algorithms during the online stage for the prediction of $\widehat{X}_\mu$. I also observe that during the online stage each mapping Φ_ν is computed based on the point clouds $\widehat{X}_\mu$ and $\widehat{X}_\nu$ (in lieu of X_ν): thanks to this choice, we prove that CDI is an interpolation method.

Technical details. Algorithm 4 relies on several elementary building blocks that need to be specified.

- *Sensor (or feature) selection:* we rely on the definition of a problem-dependent *scalar testing function* $\mathcal{T}$ to identify salient points of the solution field. For transonic and supersonic compressible flows, we relied on the *Ducros sensor* [69, 72] to detect shocks; for two-dimensional incompressible flows we considered the zero-isoline of the stream function to detect recirculation zones. The choice of the sensor is highly problem-dependent and requires a deep understanding of the underlying physical phenomenon of interest.
- *Regression:* in all our numerical experiments we consider radial basis function (RBF, [97]) approximation, with holdout validation to select the hyper-parameters (kernel width, and penalty coefficient). As in non-intrusive MOR methods (e.g., [37]), we first apply POD to determine a low-rank representation of the sorted point clouds and then we apply RBF to the POD coefficients.
- *Choice of the nearest neighbors:* we rely on the Euclidean distance in parameter to identify the neighbors of a given parameter.
- *Construction of the mappings:* we rely on the registration method outlined in section 3.2 to determine the mappings; in the numerical experiments of [TT5], we also consider an elasticity-based registration method.

- *Choice of the weights:* we determine the weights $\{\omega_{\mu}^{\nu} : \nu \in \mathcal{P}_{\rm nn}^{\mu}\}$ using the inverse distance weighting (IDW, [87]) method based on Euclidean distance in parameter.

Properties of convex displacement interpolation. The CDI (3.33) with the choice of the weights based on IDW has four noteworthy properties that are of interest for interpolation of fluid mechanics fields; I refer to [TT5] for the proofs.

1. *Interpolation.* Let $\mu \in \mathcal{P}_{\rm train}$. Then, $\widehat{u}_{\mu} = u_{\mu}$.
2. *Maximum principle.* Let $b \in \mathbb{R}^D$; then, $\sup_{x\in\Omega} \left| b \cdot \widehat{u}_{\mu}(x) \right| \leq \sup_{x \in \Omega, \nu \in \mathcal{P}} \left| b \cdot u_{\nu}(x) \right|$ for all $\mu \in \mathcal{P}$.
3. *Minimum principle.* Let $b \in \mathbb{R}^D$; then, $\inf_{x\in\Omega} b \cdot \widehat{u}_{\mu}(x) \geq \inf_{x \in \Omega, \nu \in \mathcal{P}} b \cdot u_{\nu}(x)$ for all $\mu \in \mathcal{P}$.
4. *Frame indifference.* Given the parametric field $\mu \mapsto u_{\mu}$, consider the rototranslation $p(\mu) = R\mu + b$ for some rotation matrix R and vector $b \in \mathbb{R}^P$, and the parametric field $p \mapsto v_p = u_{\mu(p)}$. Then, $\widehat{u}_{p(\mu)} = \widehat{u}_{\mu}$ for all $\mu \in \mathcal{P}$.

The maximum and minimum principles can be used to ensure that the CDI prediction is physically meaningful for out-of-sample parameters. To provide a concrete reference, if we apply CDI to the solution to the Euler or Navier-Stokes equations in primitive variables, we can guarantee that density and pressure are strictly positive and do not exceed the maximum value attained in the training set. Similarly, since the mappings $\{\Phi_{\nu}\}_{\nu}$ in (3.33) are bijective in Ω, if the far-field conditions are parameter-independent and constant on $\partial\Omega$, we can exploit the same argument to prove that CDI is consistent with the far-field conditions.

3.4.2 Data augmentation

In this manuscript, I review the application of CDI to data augmentation for a transonic flow past a Gaussian bump; in [TT5], we also apply the method to nonlinear interpolation. I denote by $\mathcal{P}_{\rm train} = \{\mu^i\}_{i=1}^{n_{\rm train}} \subset \mathcal{P}$ the training set of parameters for which HF simulations are available and by $\mathcal{P}_{\rm train,cdi} = \{\nu^i\}_{i=1}^{n_{\rm train,cdi}} \subset \mathcal{P}$ an additional set of parameters. We first define the Lagrangian space $\mathcal{Z}_0 = {\rm span}\{u_{\mu^i}^{\rm hf}\}_{i=1}^{n_{\rm train}}$ and the projection operator $\Pi_{\mathcal{Z}_0} : [L^2(\Omega)]^4 \to \mathcal{Z}_0$; then, we define the POD space

$$\mathcal{Z}_n = \mathcal{Z}_0 \oplus \mathcal{Z}_{\rm lf}, \quad \mathcal{Z}_{\rm lf} = \texttt{POD}\left(\mathcal{D}_{\rm train,lf}, n - n_{\rm train}, (\cdot,\cdot)\right), \tag{3.34}$$

where $\oplus$ indicates the direct sum of orthogonal spaces, $\mathcal{D}_{\rm train,lf} = \{\widehat{u}_{\mu} - \Pi_{\mathcal{Z}_0}\widehat{u}_{\mu} : \mu \in \mathcal{P}_{\rm train,cdi}\}$ and $\mathcal{Z}_{\rm lf}$ is the POD space of size $n - n_{\rm train}$ associated with the snapshots $\mathcal{D}_{\rm train,lf}$ and the inner product $(\cdot,\cdot)$. Note that the space $\mathcal{Z}_n$ contains the HF training set: potential inaccuracies of the CDI estimates do not pollute the performance of the reduced space for $\mu \in \mathcal{P}_{\rm train}$.

Figure 3.13 illustrates the performance for $n_{\rm train} = 9$, $n_{\rm train,cdi} = 20$. We consider a tensorized 3×3 grid for $\mathcal{P}_{\rm train}$ and we generate $\mathcal{P}_{\rm train,cdi}$ using latin hyper-cube sampling [67]. We consider a POD space in (3.34) of dimension $n = 29$; we assess performance based on a dataset of $n_{\rm test} = 20$ out-of-sample parameters. Figure 3.13(a) shows boxplots of the relative $L^2(\Omega)$ error for LSPG ROM, CDI and LSPG ROM based on $n = 9$ modes (i.e., without data augmentation) (LSPG-0). I observe that CDI is not as accurate as LSPG-0; however, it can be used to augment the dataset of simulations and ultimately contribute to reduce the prediction error. Figure 3.13(b) shows the projection error over the test set for the POD space built using (3.34) ("mixed training"), the POD space based on $n_{\rm train} + n_{\rm train,cdi}$ HF simulations ("HF training") and the POD space based $n_{\rm train}$ HF simulations ("HF training ($n_{\rm train} = 9$)"): I observe that the mixed training strategy based on CDI is not as accurate as HF training, particularly for large values of n; however, it enables significant reduction of the projection error without resorting to new simulations.

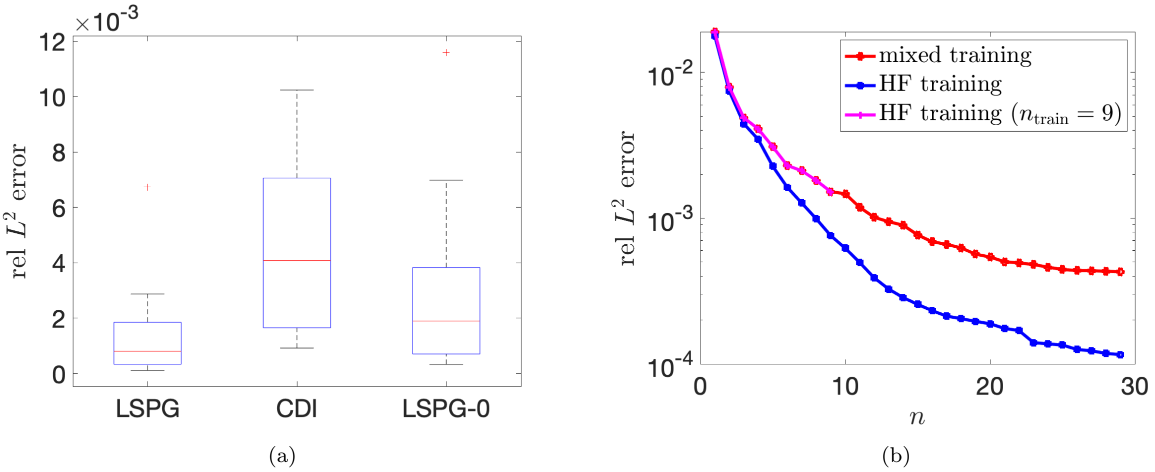

(a) (b)

Figure 3.13: data augmentation $n_{\mathrm{train}} = 9$, $n_{\mathrm{train,cdi}} = 20$. Behavior of LSPG ROM with CDI-based data augmentation. (a) boxplots of relative L^2 error for LSPG ROM, CDI and projection error ($n = 29$). (b) projection error.

Figure 3.14 replicates the results of Figure 3.13 for $n_{\mathrm{train}} = 4$, $n_{\mathrm{train,cdi}} = 25$. Interestingly, CDI is more accurate than LSPG-0: this can be explained by observing that, unlike the LSPG ROM, CDI provides estimates that do not belong to the span of the dataset of HF simulations; for small values of n_{train}, CDI can hence compensate the fact that it does not exploit the knowledge of the PDE model for prediction.

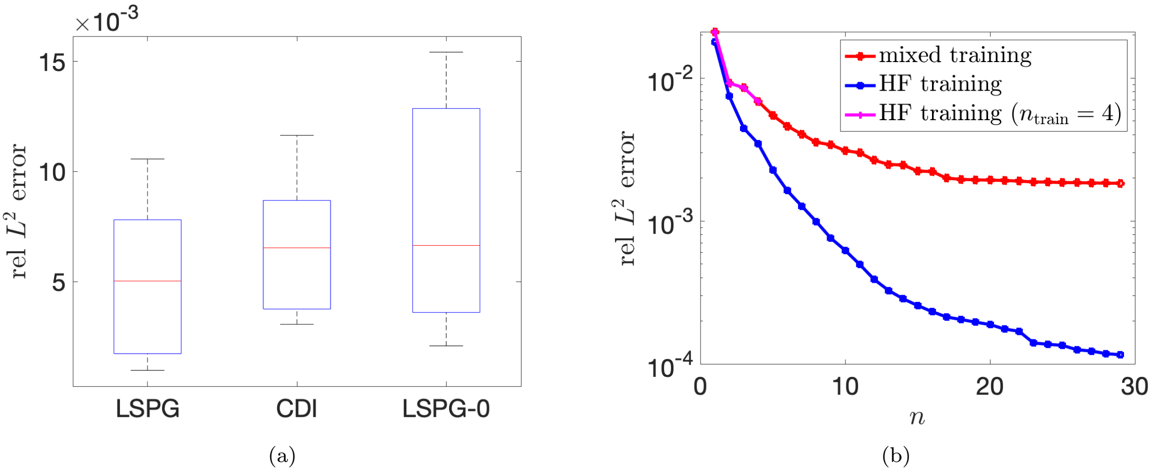

(a) (b)

Figure 3.14: data augmentation $n_{\mathrm{train}} = 4$, $n_{\mathrm{train,cdi}} = 25$. Behavior of LSPG ROM with CDI-based data augmentation. (a) boxplots of relative L^2 error for LSPG ROM, CDI and projection error ($n = 29$). (b) projection error.

Table 3.2 provides an overview of the computational costs; here, we consider a mesh with $N_e = 12748$. The HF solver is roughly 14 times slower than CDI and 625 times slower than the LSPG ROM; the construction of the LSPG ROM, which comprises the construction of the trial and test spaces and hyper-reduction, is roughly as expensive as a single full-order solve. I remark that 99% of the total cost of CDI is associated with mesh interpolation: we hence envision that more sophisticated implementations of this step (see, e.g., [61]) might lead to a significant reduction of the overall CDI cost.

	cost [s]
HF solver (avg)	481.21
ROM generation (data compression+hyperreduction)	431.24
Convex displacement interpolation (avg)	33.49
LSPG ROM ($n = 29$, avg)	0.77

Table 3.2: data augmentation. Wall-clock costs of HF and MOR procedures ($n_{\mathrm{train}} = 9, n_{\mathrm{train,cdi}} = 20$).

3.5 Research perspectives

The development and the analysis of registration methods for parametric PDEs and their integration in the MOR framework represent a main axis of my research at Inria that I plan to further pursue in the near future.

- In the PhD project of Ishak Tifouti, in collaboration with Nicolas Barral, we are currently working on the development of clustering techniques in the framework of Algorithm 3, to deal with shock topology changes that cannot be captured by a single geometry deformation.
- In the PhD project of Jon Labatut, in collaboration with Angelo Iollo, Denis Sipp, and Jean-Baptiste Chapelier, we plan to develop an alternative class of registration methods that rely on a variant of the ansatz (3.12).
- In the framework of the Inria Exploratory Action AM2OR, together with Nicolas Barral, I also plan to extend the adaptive methodology of Algorithm 3 to a broader class of PDE problems in nonlinear mechanics and CFD; towards this end, we shall extend the registration method of section 3.2 to three-dimensional geometries, and to two-dimensional and three-dimensional unsteady PDEs. This project will also benefit from the collaboration with Alberto Remigi (Safran Tech).

Chapter 4

Component-based model reduction for nonlinear systems of equations

MOR methods rely on the solution to the full-order model for several values of the parameters during the offline stage, and on the assumption that the solution field is defined over a parameter-independent domain Ω. For large-scale problems, full-order solutions might not be computable in reasonable time frame; furthermore, in many computational mechanics applications, parametric variations induce topology changes that prevent the definition of a common HF discretization that is valid for all parameters. This limitation justifies the development of component-based (CB) MOR approaches [49]: CB MOR methods combine the monolithic PMOR strategies discussed in Chapter 2 with component mode synthesis (CMS) and substructing techniques [23, 48] first appeared in the structural dynamics literature.

CB-MOR techniques rely on the introduction of a library of archetype components for which a local reduced-order approximation and a local ROM are built during an offline stage; given a new configuration, we first instantiate components from the library to form the global system and then we estimate the global solution by gluing together the local ROMs. The deployment of an effective CB-ROM for a given problem class hence relies on two distinct building blocks: first, a data compression strategy for the construction of local reduced-order approximations for each archetype component; second, a rapid and reliable domain decomposition (DD) strategy for online global predictions. The training of the local reduced-order approximations and local ROMs should not rely on expensive global solves (*localized training*); the domain decomposition strategy should enable the effective coupling between local ROMs and should be equipped with efficient hyper-reduction strategies [85] to speed up computations.

This chapter reviews my contributions to CB-MOR of nonlinear PDEs. First, in section 4.1, I present the key elements of CB MOR techniques; then, in section 4.2 I present the work with Smetana on localized training and adaptive enrichment methods [TT11]; in section 4.3, I discuss the joint work with Iollo and Sambataro on the one-shot overlapping Schwartz (OS2) method for CB-MOR of nonlinear PDEs [TT9]. Section 4.4 draws some conclusions and discusses future research directions.

4.1 Basic elements of component-based model reduction

Consider the example of Figure 4.1(a), which depicts the computational domain associated with the THM problem of [86] and suppose that (one of) the parameter of interest is the number of intervals (in red) $Q_{\rm a}$, where we prescribe the incoming thermal flux; in the remainder of the bottom boundary, we prescribe Dirichlet conditions. Since the primary goal of simulations is to assess the behavior of the geological medium for different numbers of alveoli (cf. Chapter 2), it is indeed of paramount importance to simulate different configurations for various designs of the array of alveoli. Clearly, changing the number of alveoli induces a *topology change*[1] in the system: it is hence impossible to consider the same approximation space for all parametric configurations of interest; therefore, standard monolithic MOR techniques are fundamentally ill-suited to deal with this problem. CB-MOR methods involve the definition of a library of so-called archetype components and their instantiation to define the global system.

Each *archetype component* $\bullet$ is characterized by (i) a reference domain $\Omega_\bullet^{\rm a}$ and a reference port $\Gamma_\bullet^{\rm a} \subset \partial\Omega_\bullet^{\rm a}$ where the solution is unknown, (ii) a port-to-solution map that returns the field u in $\Omega_\bullet^{\rm a}$ for any datum on $\Gamma_\bullet^{\rm a}$, (iii) a parametric mapping $\Phi_\bullet^{\rm a} : \Omega_\bullet^{\rm a} \to \mathbb{R}^d$ that deforms the reference domain $\Omega_\bullet^{\rm a}$ into the instantiated component, and (iv) a set of parameters $\mu_\bullet$ in the parameter region $\mathcal{P}_\bullet^{\rm a}$ that include both geometric parameters, which are

---

[1] A formal definition of topology change is involved and is not provided in this manuscript: in this work, I informally say that parameter variations induce a topology change if it is not possible to define a reference configuration Ω and a smooth parametric mapping Φ such that $\Omega_\mu = \Phi_\mu(\Omega)$ and $\Gamma_{{\rm dir},\mu} = \Phi_\mu(\Gamma_{\rm dir})$ for all $\mu \in \mathcal{P}$.

associated with the mapping, and model parameters, which are associated with the port-to-solution map. I denote by $\mathcal{L}$ the library of archetype components; I denote by $\mathcal{X}_\bullet^{\rm a}$ the HF space associated with the domain $\Omega_\bullet^{\rm a}$ and by $\mathcal{U}_\bullet^{\rm a}$ the trace of the elements of $\mathcal{X}_\bullet^{\rm a}$ on the port $\Gamma_\bullet^{\rm a}$. Then, the *instantiated system* is uniquely described by the set of $N_{\rm dd}$ labels $\{\mathtt{L}_i\}_{i=1}^{N_{\rm dd}} \subset \mathcal{L}$ and the set of parameters $\mu = (\mu_{\mathtt{L}_1}, \ldots, \mu_{\mathtt{L}_{N_{\rm dd}}}) \in \mathcal{P} := \bigotimes_{i=1}^{N_{\rm dd}} \mathcal{P}_{\mathtt{L}_i}^{\rm a}$. Given $i = 1, \ldots, N_{\rm dd}$, I denote by $\Phi_i := \Phi_{\mu_{\mathtt{L}_i}}^{\rm a}$ the geometric mapping, by $\{\omega_i = \Phi_i(\Omega_{\mathtt{L}_i}^{\rm a})\}_{i=1}^{N_{\rm dd}}$ the partition of the global domain Ω, by $\mathcal{X}_i := \{v \circ \Phi_i^{-1} : v \in \mathcal{X}_{\mathtt{L}_i}^{\rm a}\}$ the instantiated HF space and by $\mathcal{U}_i := \{v \circ \Phi_i^{-1} : v \in \mathcal{U}_{\mathtt{L}_i}^{\rm a}\}$ the instantiated port space.

Exploiting the previous definitions, I can formalize the two tasks of CB-MOR, localized training and domain decomposition. *Localized training* aims to speed up the evaluation of the instantiated port-to-solution maps $\mathfrak{F}_i : \mathcal{U}_i \to \mathcal{X}_i$ for $i = 1, \ldots, N_{\rm dd}$, or equivalently of the corresponding archetype maps $\mathfrak{F}_\bullet^{\rm a} : \mathcal{U}_\bullet^{\rm a} \times \mathcal{P}_\bullet^{\rm a} \to \mathcal{X}_\bullet^{\rm a}$ for all $\bullet \in \mathcal{L}$. Note that the problem of localized training can be decoupled into two subproblems: (i) the problem of *port reduction* [30], which consists in determining a low-dimensional approximation $\widehat{\mathcal{U}}_\bullet^{\rm a}$ of the port space $\mathcal{U}_\bullet^{\rm a}$, and (ii) the problem of determining an effective surrogate of the restricted map $\mathfrak{F}_\bullet^{\rm a} : \widehat{\mathcal{U}}_\bullet^{\rm a} \times \mathcal{P}_\bullet^{\rm a} \to \mathcal{X}_\bullet^{\rm a}$. Since $\widehat{\mathcal{U}}_\bullet^{\rm a}$ and $\mathcal{P}_\bullet^{\rm a}$ are low-dimensional, the latter problem fits into the framework of monolithic MOR. *Domain decomposition* addresses the coupling of the local ROMs to determine the port solution $u^{\rm p} = (u_1^{\rm p}, \ldots, u_{N_{\rm dd}}^{\rm p}) \in \widehat{\mathcal{U}}_\bullet^{\rm a} = \bigotimes_{i=1}^{N_{\rm dd}} \widehat{\mathcal{U}}_{\mathtt{L}_i}^{\rm a}$ for a given parameter $\mu \in \mathcal{P}$. After having estimated the port solution $u^{\rm p}$, we can resort to the local port-to-solution maps to obtain the full estimate.

Some comments are in order. As discussed in section 4.3, the introduction of the port space enables static condensation of the internal degrees of freedom and is convenient for computations. Nevertheless, several DD approaches (e.g., [52, 68]) do not explicitly rely on the introduction of a port space; for these approaches, localized training directly tackles the construction of a ROB for the full solution in $\mathcal{X}_\bullet^{\rm a}$. The local models $\{\mathfrak{F}_\bullet^{\rm a} : \bullet \in \mathcal{L}\}$ might not be consistent with each other: to provide a concrete reference, we might be interested in combining linear and nonlinear elasticity models in different regions of the global domain to model local phenomena such as fracture or contact [6]. It is indeed of prominent importance to devise DD methods that can cope with different and possibly inconsistent local models. Finally, hyper-reduction of CB-ROMs involves both the hyper-reduction of the local ROMs, which can exploit the standard techniques developed for monolithic ROMs, and hyper-reduction of the coupling equation; similarly, rigorous *a posteriori* error estimators should include inter-component and intra-component errors [73, 89].

For the problem depicted in Figure 4.1(a), we consider two archetype components (cf. Figure 4.1(b)): the former is dubbed "internal" ($\bullet = {\rm int}$), it is associated with a single alveolus, the parameters include the horizontal size, which allow us to vary the distance between consecutive alveoli, the intensity of the source term, and the Young's modulus of the elastic medium; the latter is dubbed "external" ($\bullet = {\rm ext}$), it is associated with the far-field region, the parameters include a shape parameter and the Young's modulus. The ports $\Gamma_{\rm int}^{\rm a}$ and $\Gamma_{\rm ext}^{\rm a}$ correspond to the portions of the boundary that belongs to the interior of the domain. I observe that the partition is overlapping; in [TT9] and [TT11] we consider overlapping partitions: the analysis of non-overlapping DD methods and the combination of different models is the subject of ongoing research (see [TT16]). A thorough review of the recent contributions to CB-MOR is beyond the scope of this manuscript and can be found in [TT9, TT11].

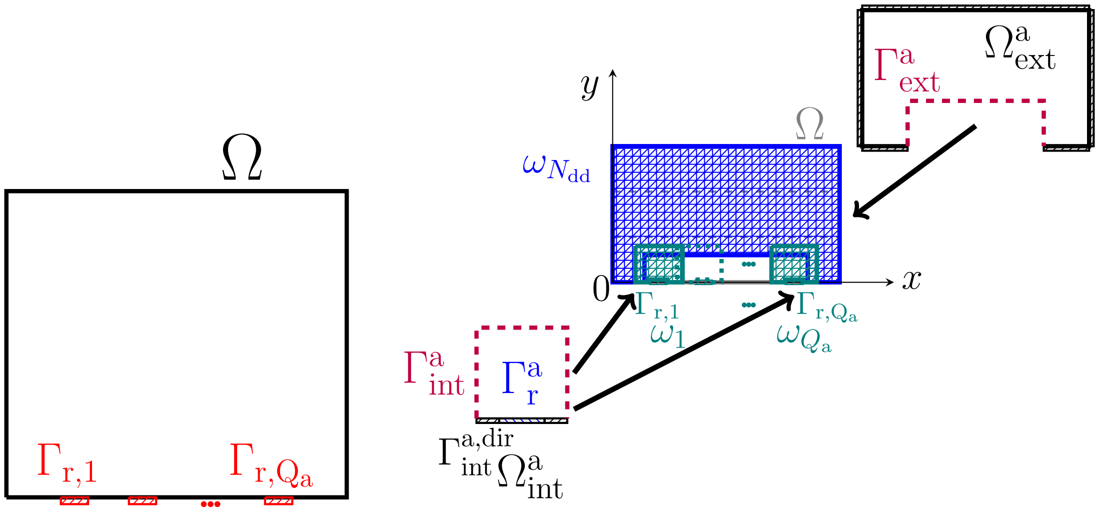

(a) (b)

Figure 4.1: (a) domain Ω and boundaries $\Gamma_{\rm r,1}, \ldots, \Gamma_{\rm r,Q_a}$ that can vary in number and position. (b) domain partition and archetype components.

4.2 Training of archetype components via localized random sampling and adaptive enrichment

Together with Smetana, I developed a randomized localized training strategy based on *oversampling* and *adaptive enrichment* to devise local approximation spaces for nonlinear elliptic PDEs [TT11]. We considered a nonlinear diffusion problem of the form

$$-\nabla \cdot (\kappa_\mu(u_\mu)\nabla u_\mu) = f_\mu \quad \text{in } \Omega; \quad u_\mu = 0 \ \text{ on } \partial\Omega, \tag{4.1}$$

where the diffusion coefficient κ_μ is a nonlinear function of the state u_μ and of two parameters that are constant in each element of the grid of Figure 4.2(a); the source term is active only in one element of the grid. The parameters of the problem are the number of grid elements, the values of the two parameters associated with the diffusion coefficient in each element of the grid, and the index of the element of the grid where the source term is active. Figures 4.2(b) and (c) show two snapshots of the solution for a 10 × 10 grid and two choices of the parameters. In order to approximate the problem using CB-MOR, we consider an overlapping partition based on three archetype components (cf. Figure 4.2(a)); furthermore, we rely on the partition-of-unity method (PUM, [68]) for DD.

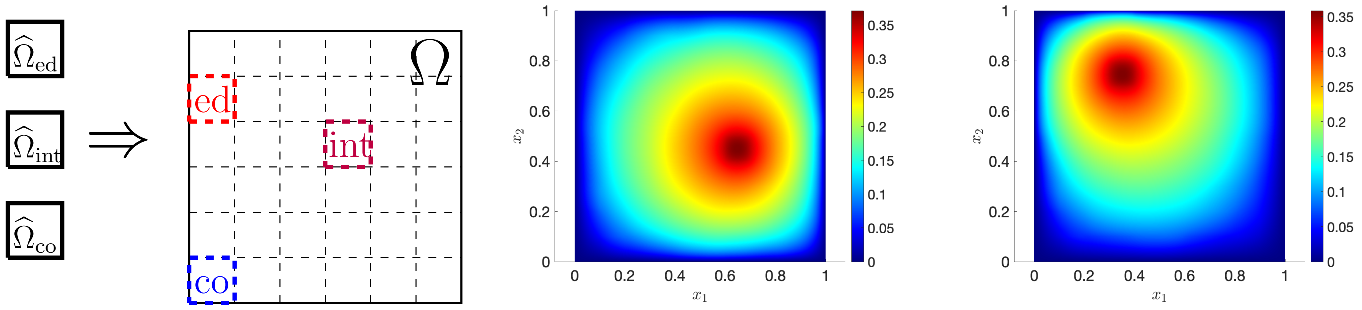

(a) (b) (c)

Figure 4.2: nonlinear diffusion. (a) description of the system based on three archetype components. (b)-(c) solution fields for $N_{\rm dd} = 100$ and two choices of the parameters.

4.2.1 Methodology

In order to avoid global solves to generate the ROBs for the three archetype components, we introduce the oversampling domains of Figure 4.3. The dashed boundaries correspond to the region where we impose Dirichlet conditions; note that the edge (resp., internal, corner) component includes six (resp., nine, four) elements of the grid. Then, we collect snapshots of the local solution manifolds by repeatedly solving the PDE in the oversampling domain for random choices of the boundary condition g on the boundary $\Gamma_{\rm in}^{\bullet}$; finally, we apply POD to determine a low-dimensional approximation space. Oversampling methods have been first proposed in the multiscale/generalized finite element literature [41], and then extensively considered in CB-MOR (e.g., [19]). For nonlinear problems, we show that the effectiveness of oversampling heavily relies on the choice of the sampling distribution. In our work, we propose a randomized sampling strategy that controls (in a probabilistic sense) the smoothness of the boundary datum through the vehicle of a user-defined parameter α.

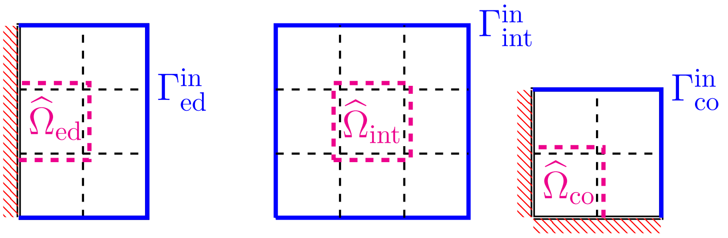

(a)

Figure 4.3: oversampling domains for each component; $\Gamma_{\bullet}^{\rm in}$ denotes the subset of the boundary where we prescribe random boundary conditions. The dashed boundaries correspond to the region where we impose Dirichlet conditions.

The need for enrichment strategies stems from the observation that the choice of the distribution for oversampling is extremely challenging and might lead to suboptimal results. On the other hand, it is typically much easier to identify a proper sampling strategy to generate global configurations. For the problem of [TT11], we generate random configurations based on grids of variable size and we randomly choose the location of the source term. We propose an enrichment strategy based on a *mark-then-refine* paradigm: first, we generate a CB-ROM through oversampling; second, we estimate the solution to $n_{\rm train}$ global systems using the CB-ROM; third, we estimate the local error in each element of the partition using a residual-based error indicator and we mark the instantiated elements where the error is the largest; fourth, we solve the PDE using the HF solver in each marked subdomain and we update the ROBs. I observe that adaptive enrichment strategies driven by error indicators have been proposed for linear steady problems in [73] and further studied in the multiscale FE context [18, 22]; the major difference between the approaches in [18, 73] and our approach in [TT11] is that we perform enrichment at training stage at the component level as opposed to during the online stage on the deployed structure. I refer to [TT11, Algorithm 6.1] for a detailed presentation of the method, and to [TT11, Proposition 6.6] for the convergence analysis for linear coercive problems.

4.2.2 Numerical results

I review the numerical results in [TT11] for a nonlinear diffusion problem. We discretize the problem using a Q3 spectral element method based on a structured grid with 961 degrees of freedom in each element of the grid (cf. Figure 4.2(a)). We generate $n_{\rm train} = 200$ random samples using oversampling based on the random distribution discussed in [TT11, Algorithm 5.2] ("smooth sampling"). To assess the performance, we also introduce the "Gaussian" random field

$$\begin{aligned} & g^\bullet(x;\mathbf{c}) := \sum_{i\in \mathtt{I}^\bullet_{\rm dir}} \mathfrak{f}(c_i,\bar{u}_{\max})\phi_i^{{\rm fe},\bullet}(x), \quad c_i \overset{\rm iid}{\sim} \mathcal{N}\left(\frac{\bar{u}_{\max}}{2},\frac{\bar{u}_{\max}^2}{4}\right), \\ & \mathfrak{f}(c,u) = \max\{\min\{c,u\},0\}, \end{aligned} \tag{4.2}$$

where $\bar{u}_{\max} \in (0,1)$ is a threshold parameter[2], $\{\mathtt{I}^\bullet_{\rm dir}\}_\bullet$ denote the set of indices of the mesh on the patch input boundaries and $\{\phi_i^{{\rm fe},\bullet}\}_\bullet$ are the Lagrangian bases associated with the HF discretization of the component $\bullet$. Furthermore, we compute $n_{\rm test} = 30$ global solutions for $N_{\rm dd} = 100$ components (10×10 grid); then, we define the test datasets $\{\mathcal{D}^\bullet\}_{\bullet\in\{\mathtt{co},\mathtt{ed},\mathtt{int}\}}$ by extracting the solution in each element of the partition — ${\rm card}(\mathcal{D}^\bullet) = 1920$ (resp., $120, 960$) for the internal (resp., corner, edge) component. Finally, we introduce the localized error indicators

$$E^\bullet_{\rm avg,rel}(\mathcal{Z}^\bullet) = \frac{1}{{\rm card}(\mathcal{D}^\bullet)} \sum_{w\in\mathcal{D}^\bullet} \frac{\|w - \Pi_{\mathcal{Z}^\bullet} w\|_\bullet}{\|w\|_\bullet}, \quad \bullet \in \mathfrak{L}, \tag{4.3}$$

which are used to assess performance.

Figure 4.4 shows the behavior of the relative errors (4.3) for the three components, for smooth sampling for three choices of the parameter α, and for Gaussian sampling (4.2). Larger values of α correspond to smoother boundary conditions. To provide a reference, we also show performance of the POD spaces based on the datasets $\{\mathcal{D}^\bullet_{\rm test}\}_{\bullet\in\{\mathtt{co},\mathtt{ed},\mathtt{int}\}}$ ("bench") generated using 30 additional global simulations with $N_{\rm dd} = 100$ components. I observe that smooth sampling outperforms Gaussian sampling for the boundary components: we believe that this is due to the presence of strong Dirichlet conditions on $\partial\widehat{\Omega}^\bullet_{\rm ovr} \setminus \widehat{\Gamma}^\bullet_{\rm in}$. I further observe that results weakly depend on the choice of α.

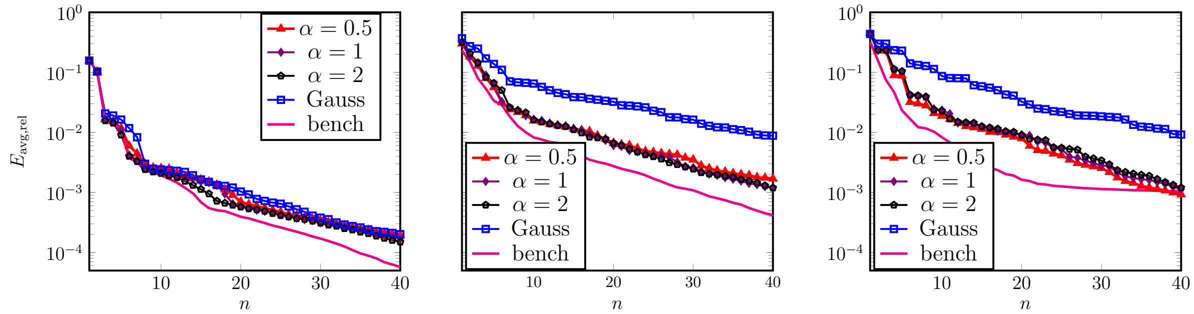

(a) internal component (b) edge component (c) corner component

Figure 4.4: nonlinear problem. Local approximation errors (4.3) for three choices of α, and for Gaussian sampling (4.2). Comparison with POD spaces based on the datasets $\{\mathcal{D}^\bullet_{\rm test}\}_{\bullet\in\{\mathtt{co},\mathtt{ed},\mathtt{int}\}}$ generated using 30 additional global simulations with $N_{\rm dd} = 100$ components ("bench").

---

[2] Since the solution represents water saturation, we should ensure that $u_\mu \in [0,1]$ a.e.; in practice, I set $\bar{u}_{\max} = 0.5$ in all our numerical simulations of this manuscript; I refer to [TT11] for further numerical investigations.

Figure 4.5 investigates the performance of the adaptive enrichment procedure. We apply [TT11, Algorithm 6.1] with a residual-based error indicator to the nonlinear diffusion problem (4.1); I refer to [TT11] for the details. We assess performance based on $n_{\text{test}} = 20$ out-of-sample randomly-chosen configurations. Figure 4.5(a) and (b) show boxplots of the relative H^1 error after each iteration of the training algorithm — iteration 0 corresponds to the performance of the CB-ROM without global enrichment. Iteration 0 corresponds to a reduced space of size $n = 20$; iterations $it = 1, 2, 3$ correspond to reduced spaces of size $n = 20 + 10 \cdot it$. I observe that the enrichment iterations significantly improve performance of the CB-ROM and reduce the impact of the initial sampling distribution.

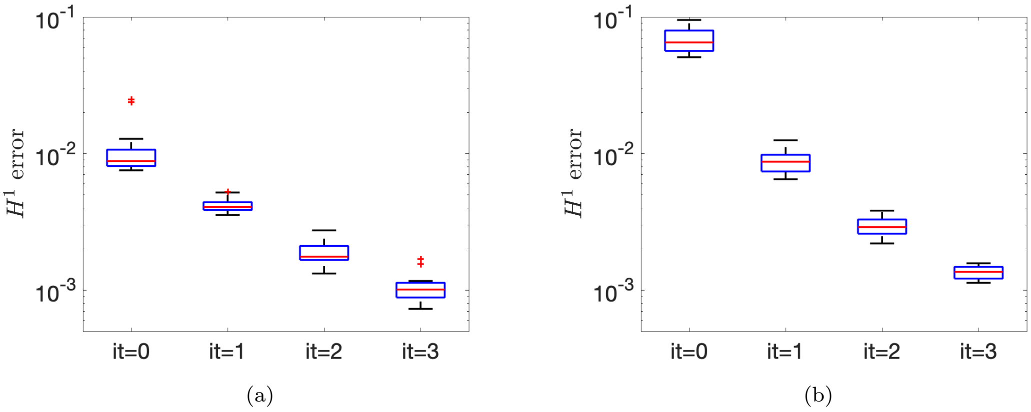

Figure 4.5: nonlinear problem; adaptive enrichment. (a)-(b) boxplots of the relative H^1 error on the test set for smooth and Gaussian sampling of localized BCs.

Figure 4.6 shows the maximum relative in-sample and out-of-sample H^1 error for the same sampling strategies considered in Figure 4.5. To facilitate the interpretation, we also provide the fitted exponential curve $\widehat{E} = \exp(\alpha n + \beta)$ obtained by discarding the first datapoint. For this model problem, numerical results suggest nearly-exponential in-sample convergence of the adaptive enrichment strategy.

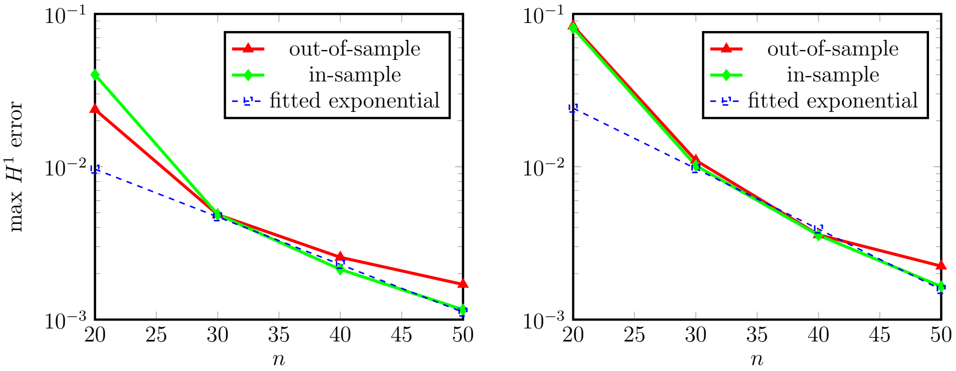

(a) $\alpha = 1$ (b) Gauss

Figure 4.6: nonlinear problem; adaptive enrichment. Behavior of the maximum relative error on training (in-sample) and test (out-of-sample) sets for smooth ($\alpha = 1$) and Gaussian sampling.

4.3 Domain decomposition methods for MOR

Together with Iollo and Sambataro, I developed a DD strategy for overlapping partitions, for nonlinear elliptic and parabolic PDEs. Our approach is derived from the standard overlapping Schwartz (OS) method and reads as a constrained optimization statement that penalizes the jump at the components' interfaces subject to the approximate satisfaction of the PDE in each local subdomain. Furthermore, the approach relies on the decomposition of the local states into a port component associated with the solution on interior boundaries and a bubble component that vanishes at ports. Below, I review the basic idea of the approach in a simplified setting; I refer to [TT9] and to the PhD thesis [86] for a thorough presentation.

4.3.1 Methodology

I introduce the formulation in the simplified case of two instantiated components Ω_1, Ω_2 (cf. Figure 4.7) — to simplify notation, I do not distinguish between archetype and instantiated components. I denote by $\mathcal{X}_i \subset H^1(\Omega_i)$ a suitable Hilbert space in Ω_i; I further define the *bubble space* $\mathcal{X}_{i,0} = \{v \in \mathcal{X}_i : v|_{\Gamma_i} = 0\}$ and the *port space* $\mathcal{U}_i = \{v \in \mathcal{X}_i : v|_{\Gamma_i} = 0\}$, for $i = 1, 2$. Then, I introduce the additive or multiplicative OS iterations as

$$\begin{cases} \text{find } \ u_1^{(k)} \in \mathcal{X}_1 \ : \ \mathfrak{R}_1(u_1^{(k)}, v) = 0 \ \ \forall\, v \in \mathcal{X}_{1,0}, \ \ u_1^{(k)}|_{\Gamma_1} = u_2^{(k-1)}; \\ \text{find } \ u_2^{(k)} \in \mathcal{X}_2 \ : \ \mathfrak{R}_2(u_2^{(k)}, v) = 0 \ \ \forall\, v \in \mathcal{X}_{2,0}, \ \ u_2^{(k)}|_{\Gamma_2} = \begin{cases} u_1^{(k)}, \\ u_1^{(k-1)}, \end{cases} \end{cases} \tag{4.4}$$

for $k = 1, 2, \ldots$. Here, $u_i^{(k)}$ denotes the state estimate at the k-th iteration in the i-th subdomain, while $\mathfrak{R}_1, \mathfrak{R}_2$ are the variational forms associated with the PDE of interest in Ω_1, Ω_2. *Multiplicative* Schwarz iterations correspond to setting $u_2^{(k)}|_{\Gamma_2} = u_1^{(k)}$ in $(4.4)_2$, while *additive* Schwarz iterations correspond to setting $u_2^{(k)}|_{\Gamma_2} = u_1^{(k-1)}$. Convergence of the OS iterations to a limit state $(u_1^\star, u_2^\star)$ implies that $\|u_1^\star - u_2^\star\|_{L^2(\Gamma_1 \cup \Gamma_2)} = 0$. We thus propose to consider the formulation

$$\min_{u_1 \in \mathcal{X}_1, u_2 \in \mathcal{X}_2} \|u_1 - u_2\|_{L^2(\Gamma_1 \cup \Gamma_2)} \quad \text{s.t. } \ \mathfrak{R}_i(u_i, v_i) = 0 \ \ \forall\, v_i \in \mathcal{X}_{i,0}, \ i = 1, 2. \tag{4.5}$$

Clearly, the pair $(u_1^\star, u_2^\star)$ is a solution to (4.5); in [TT9, section 4], we show that, provided that the overlapping size δ is strictly positive, the solution to (4.5) is unique and depends continuously on data for linear coercive problems. Note that, for linear problems, the solution to (4.5) can be computed directly without the need for an iterative scheme: we thus refer to our approach as to one-shot (OS) overlapping Schwarz (OS) method and we use the abbreviation OS2.

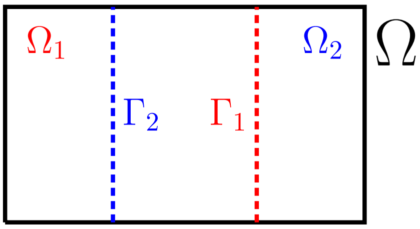

Figure 4.7: configuration considered for illustration and for the analysis of the linear coercive problem.

In order to recast (4.5) into an unconstrained problem, we denote by $u_1^{\rm p}, u_2^{\rm p}$ the port solutions, that is the restrictions of u_1 and u_2 to the corresponding ports; then, we introduce the extension operators $\mathtt{E}_i : \mathcal{U}_i \to \mathcal{X}_i$ and the local *port-to-bubble* solution maps $\mathfrak{F}_{i,0} : \mathcal{U}_i \to \mathcal{X}_{i,0}$ such that, given $w \in \mathcal{U}_i$, we have $\mathfrak{R}_i(\mathfrak{F}_{i,0}(w) + \mathtt{E}_i w, v_i) = 0 \ \ \forall\, v_i \in \mathcal{X}_{i,0}$, for $i = 1, 2$ — note that the bubble field is uniquely determined by the corresponding port solution. Then, we obtain the unconstrained OS2 statement:

$$\min_{u_1^{\rm p} \in \mathcal{U}_1, u_2^{\rm p} \in \mathcal{U}_2} \mathfrak{f}(u_1^{\rm p}, u_2^{\rm p}) := \|\mathfrak{F}_{1,0}(u_1^{\rm p}) + \mathtt{E}_1 u_1^{\rm p} - \mathfrak{F}_{2,0}(u_2^{\rm p}) - \mathtt{E}_2 u_2^{\rm p}\|^2_{L^2(\Gamma_1 \cup \Gamma_2)}. \tag{4.6}$$

The present derivation can be viewed as a *static condensation* of bubble degrees of freedom and is similar in scope to the approach in [49]. Following taxonomy from the optimization literature, we might view our approach as *black-box* — as opposed to *all-at-once* [43, section 1.1].

Practical implementation of a CB-MOR approach based on (4.5)-(4.6) requires to address three major tasks:

1. (*data compression*) the minimization statement (4.6) is infinite-dimensional: we should thus drastically reduce the dimensionality of the port spaces $\mathcal{U}_1, \mathcal{U}_2$;

2. (*reduction of local problems*) the local problems associated with the evaluation of the port-to-bubble maps are also infinite-dimensional: we should thus resort to standard (monolithic) MOR techniques to devise low-rank approximations of the bubble fields;

3. (*hyper-reduction of the objective function*) evaluation of the objective function in (4.6) requires integration over the whole curve $\Gamma_1 \cup \Gamma_2$: we should thus devise a low-dimensional quadrature rule that requires evaluation of the local fields in a moderate number of quadrature points.

In [TT9], we propose specialized MOR strategies to address these three tasks: we resort to proper orthogonal decomposition (POD, [95]) based on the method of snapshots [88] to build low-dimensional port spaces; we rely on Galerkin ROMs (cf. Chapter 2) with hyper-reduction based on empirical quadrature/mesh sampling and weighting [32, 101]; finally, we consider two distinct approaches to speed up the computation of the objective function: the former is based on empirical quadrature, while the latter relies on the empirical interpolation method (EIM, [11]) .

Exploiting the static condensation of the bubble degrees of freedom, we can interpret the OS2 ROM as a minimum residual formulation of the port (or interface) problem associated with the underlying PDE. In [TT9], we discuss this interpretation for linear coercive problems. I remark that, similarly to [58], our analysis exploits a variational interpretation of the Schwarz method.

In order to investigate the structure of (4.6), I introduce the bubble and port reduced spaces $\mathcal{Z}_i \subset \mathcal{X}_{i,0}$ and $\mathcal{W}_i \subset \mathtt{E}_i(\mathcal{U}_i) \subset \mathtt{X}_i$ and the ROBs $Z_i = [\zeta_{i,1}, \ldots, \zeta_{i,n}] : \mathbb{R}^n \to \mathcal{Z}_i$ and $W_i = [\psi_{i,1}, \ldots, \psi_{i,m}] : \mathbb{R}^m \to \mathcal{W}_i$. Then, I define the discrete local (Galerkin) residuals:

$$\widehat{\mathbf{R}}_i : \mathbb{R}^n \times \mathbb{R}^m \to \mathbb{R}^n \quad \text{s.t.} \quad \left(\widehat{\mathbf{R}}_i(\boldsymbol{\alpha}, \boldsymbol{\beta})\right)_j = \mathfrak{R}_i\left(Z_i \boldsymbol{\alpha} + W_i \boldsymbol{\beta}, \zeta_{i,j}\right), \quad j = 1, \ldots, n, \;\; i = 1, 2, \tag{4.7}$$

and the port-to-bubble maps

$$\mathbf{F}_i : \mathbb{R}^m \to \mathbb{R}^n \quad \text{s.t.} \quad \widehat{\mathbf{R}}_i(\mathbf{F}_i(\boldsymbol{\beta}), \boldsymbol{\beta}) = \mathbf{0} \quad j = 1, \ldots, n, \;\; i = 1, 2. \tag{4.8}$$

Finally, it is easy to verify that there exists two matrices $\mathbf{P}, \mathbf{Q}$ such that (4.6) can be rewritten as

$$\min_{\boldsymbol{\beta} = [\boldsymbol{\beta}_1, \boldsymbol{\beta}_2] \in \mathbb{R}^{2m}} \; g(\boldsymbol{\beta}) = \left\| \mathbf{P} \mathbf{F}(\boldsymbol{\beta}) + \mathbf{Q} \boldsymbol{\beta} \right\|_2^2, \quad \text{where } \mathbf{F}(\boldsymbol{\beta}) = \left[\begin{array}{c} \mathbf{F}_1(\boldsymbol{\beta}_1) \\ \mathbf{F}_2(\boldsymbol{\beta}_2) \end{array} \right], \tag{4.9}$$

which reads as a nonlinear least-square problem of size $2m$. I observe that the evaluation of the port-to-bubble maps (4.8) involves the solution to a system of n nonlinear equations with n unknowns; on the other hand, the gradient of $\mathbf{F}$ is block-diagonal and

$$\nabla \mathbf{F}_i(\boldsymbol{\beta}_i) = -\left(\partial_{\boldsymbol{\alpha}} \widehat{\mathbf{R}}_i\right)^{-1} \partial_{\boldsymbol{\beta}} \widehat{\mathbf{R}}_i \big|_{(\boldsymbol{\alpha}, \boldsymbol{\beta}) = (\mathbf{F}_i(\boldsymbol{\beta}), \boldsymbol{\beta})}, \quad i = 1, 2;$$

the evaluation of $\nabla \mathbf{F}_i$ hence involves the solution to m linear systems of size n.

We can consider three classes of methods to solve (4.9): (i) gradient-free methods; (ii) gradient-descent/quasi Newton methods; (iii) the Gauss-Newton method (GNM) or the Levemberg-Marquandt algorithm (LMA). The first class of methods includes additive and multiplicative OS methods. The second class of methods relies on the gradient of the objective g in (4.9): it is possible to show that the evaluation of ∇g does not require the full assembly of $\nabla \mathbf{F}$ and involves the solution to only two (one for each subdomain) linear systems of size n. The third class of methods requires the full assembly of $\nabla \mathbf{F}$: it is hence computationally feasible only if the number of modes is small (port reduction). Nevertheless, GNM and LMA exploit the underlying structure of the problem: as a result, they are expected to be more robust and converge in fewer iterations, as shown in the numerical experiments.

4.3.2 Numerical results

Model problem. I review the numerical investigations performed in [TT8] for a two-dimensional (plane stress) nonlinear (neo-Hookean) elasticity problem; the PhD thesis [86] includes further numerical investigations for a nonlinear unsteady THM problem. The problem at hand shares the same geometric configuration with the problem studied in [TT8] for radioactive management applications. We consider the constitutive law for the first Piola Kirchhoff stress tensor

$$P(F(u)) = \lambda_2 \left(F(u) - F(u)^{-\top}\right) + \lambda_1 \log\left(\det(F(u))\right) F(u)^{-\top}. \tag{4.10a}$$

Here, $F(u) = \mathbb{1} + \nabla u$ is the deformation gradient associated with the displacement u, λ_1, λ_2 are the Lamé constants given by

$$\lambda_1 = \frac{E\nu}{1 - \nu^2}, \qquad \lambda_2 = \frac{E}{2(1 + \nu)}, \tag{4.10b}$$

where E is the Young's modulus, and ν is the Poisson's ratio. We consider the domain $\Omega = (0,1)^2$ depicted in Figure 4.8; we set $\nu = 0.3$ and we consider $E = E_k$ in ω_k for $k = 1, 2, 3$. We prescribe normal homogeneous Dirichlet conditions on the left and right boundaries; homogeneous Dirichlet conditions on the bottom boundary $\Gamma_{\rm btm}$ and the Neumann conditions:

$$P(F(u))\mathbf{n}\big|_{\Gamma_{\rm top}} = g_{\rm top} := \left[\begin{array}{c} 0 \\ -4x_1(1 - x_1) \end{array} \right], \quad P(F(u))\mathbf{n}\big|_{\Gamma_{\rm r,q}} = g_{\rm r} := -s \left[\begin{array}{c} 0 \\ 1 \end{array} \right], \quad q = 1, \ldots, Q_{\rm a} \tag{4.10c}$$

with $s > 0$.

The system of equations below summarizes the problem: we seek the solution $u : \Omega \to \mathbb{R}^2$ to the system

$$\begin{cases} -\nabla \cdot P(F(u)) = 0 & \text{in } \Omega \\ u \cdot \mathbf{n} = 0 & \text{on } \{0,1\} \times (0,1) \\ P(F(u))\mathbf{n} = g_{\rm r} & \text{on } \Gamma_{\rm r} \\ P(F(u))\mathbf{n} = g_{\rm top} & \text{on } \Gamma_{\rm top} \\ u = 0 & \text{on } \Gamma_{\rm btm} = (0,1) \times \{0\} \setminus \Gamma_{\rm r} \end{cases} \tag{4.11}$$

where $\Gamma_{\rm r} = \bigcup_{q=1}^{Q_{\rm a}} \Gamma_{\rm r,q}$. Our goal is to estimate the solution to (4.11) for any choice of the Young's moduli (E_1, E_2, E_3) associated with the regions $\omega_1, \omega_2, \omega_3$ in $[25,30] \times [10,20] \times [10,20]$, any value of $s \in [0.4, 1]$ in (4.10c), and any $Q_{\rm a} \in \{2, \ldots, 7\}$. Note that variations of $Q_{\rm a}$ induce topological changes that prevent the application of standard monolithic techniques.

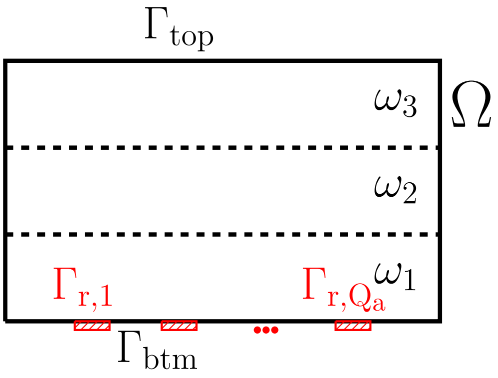

Figure 4.8: global system. $\Gamma_{\rm top}$ and $\Gamma_{\rm r,1}, \ldots, \Gamma_{\rm r,Q_a}$ are associated with the stress conditions; the regions $\{\Gamma_{\rm r,q}\}_q$ are of equal size $\ell_{\rm r} > 0$, and the distance between consecutive regions is constant and equal to $\lceil > \ell_{\rm r}$.

Results. Below, I denote by m the dimension of the reduced port space and by n the dimension of the reduced bubble space; in the tests I set $m = n$ and I consider the same value of m (and n) for all instantiated components; performance is assessed based on $n_{\rm test} = 20$ out-of-sample simulations. In Figure 4.9, I investigate the performance of the optimization method: I consider the quasi-Newton method, the Gauss-Newton method and the multiplicative OS method (cf. [TT9, Algorithm 4]). Figure 4.9(a) shows the behavior of the objective function (cf. (4.6)) for several values of the port size m; Figure 4.9(b) shows the number of iterations required to meet the convergence criterion. I observe that the three methods lead to the same value of the objective function: this is expected since they all aim to minimize the same target. I further observe that GNM converges with much fewer iterations.

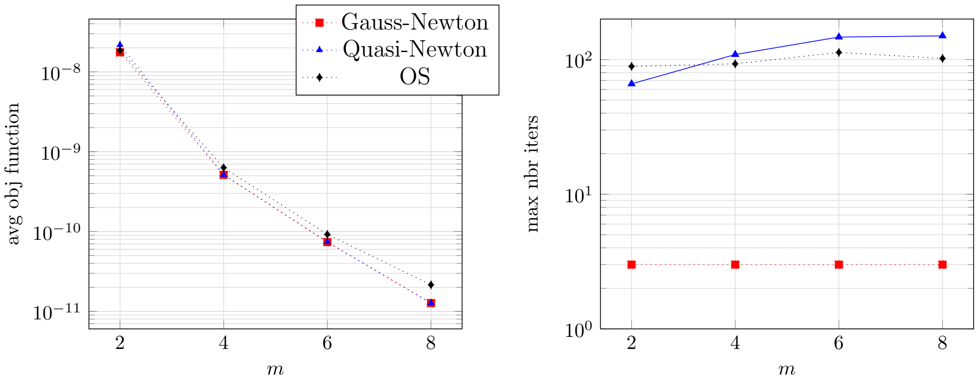

(a) (b)

Figure 4.9: comparison between Gauss-Newton, quasi-Newton, OS ($n = m$). (a) behavior of the objective function. (b) number of iterations.

In Figure 4.10, I investigate the sensitivity of two (OS and GNM) optimization algorithms with respect to the size of the overlap. In more detail, I study the behavior of the objective function, the number of iterations, and the computational cost for three choices of the overlapping size δ (cf. Figure 4.10(a)). As for the previous test, I observe that the value of the objective function is essentially the same for both OS and GNM; on the other hand, the number of iterations that are required by OS is much larger; furthermore, the number of iterations of OS increases significantly as we decrease the size of the overlap, while for GNM the iteration count is unchanged. I conclude that GNM is significantly more robust than OS with respect to the overlapping size. Finally, I notice that GNM is nearly 20 times faster than OS for $\delta = 1/6\ell_{\mathrm{r}}$ and $m = 16$.

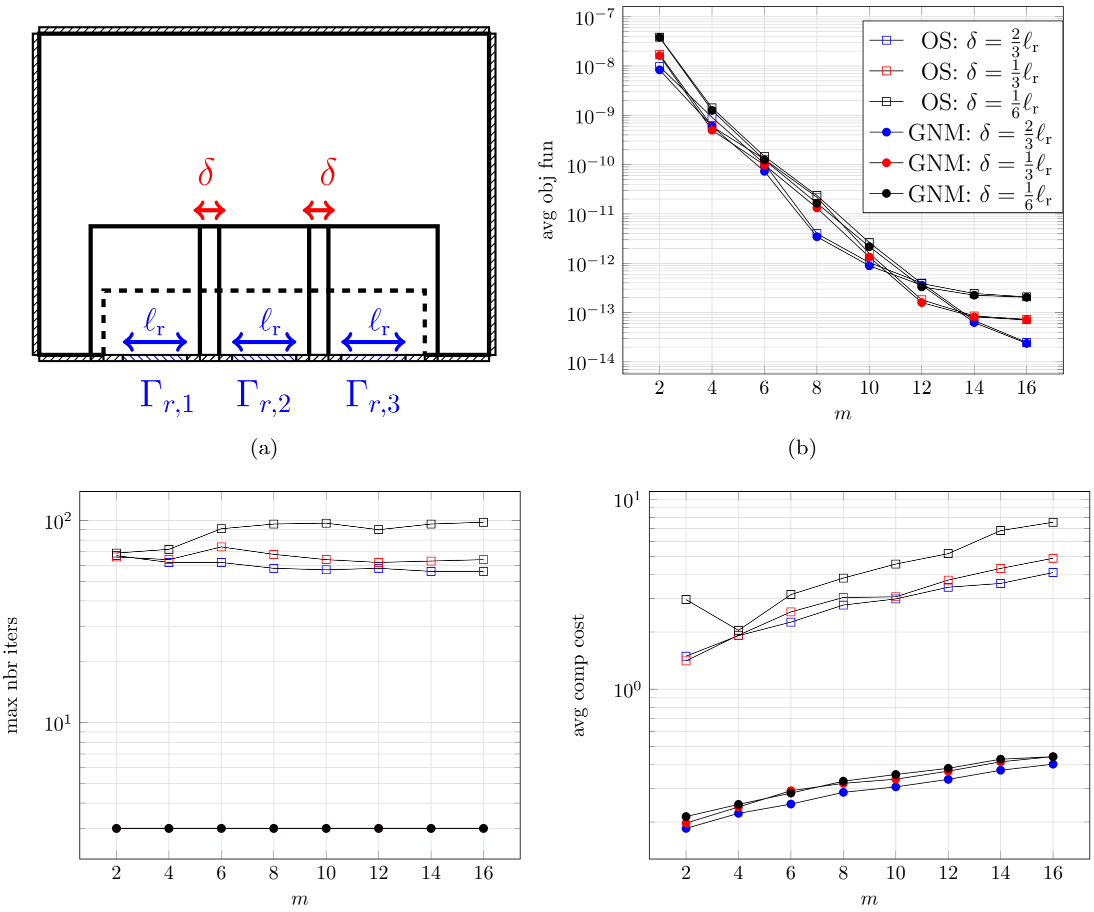

(a)

(b)

(c)

(d)

Figure 4.10: sensitivity with respect to the overlapping size δ for OS and GNM, for several values of m. (a) geometric configuration. (b) average objective function. (c) maximum number of iterations. (d) average computational cost.

4.4 Research perspectives

CB-MOR is an active area of research at the intersection between numerical analysis, computational mechanics and scientific computing. I plan to further work on this subject in the near future, with focus on steady and unsteady PDEs.

- I collaborate with Lei Zhang (Tongji University) to devise one-shot approches for non-overlapping partitions, and multi-physics problems that might involve fluid-structure interaction (FSI) and might rely on independent HF solvers for different components of the problem. The recent work [TT16] addresses the development of an optimization-based DD framework for stationary incompressible flows with local LSPG reduced-order models (cf. Chapter 2), and extends the localized training and adaptive enrichment method proposed in [TT11] to the incompressible Navier-Stokes equations.
- I collaborate with Kathrin Smetana to analyze performance of randomized methods for nonlinear PDEs. The ultimate goal is to identify accurate sampling strategies to explore the parameter domain and then train local ROMs for coupled systems.

Chapter 5

Conclusions

Model order reduction of parametric PDEs is a well-established field in scientific computing that has experienced significant developments in the past two decades, for a broad range of problems in computational mechanics. Despite the numerous examples of applications of MOR to large-scale industrial applications (e.g., [6, 14, 96]), the practical deployment of projection-based MOR techniques remains limited. My research at Inria aims to overcome the limitations of state-of-the-art MOR methods and ultimately enable their application to real-world problems.

So far, my research on MOR has focused on three axes that concern three grand challenges of MOR methods.

- *Linear-subspace model reduction of parametric systems.* I developed hyper-reduced projection-based ROMs for nonlinear PDEs with internal variables and geometric parameters, and I addressed the integration of the methodology with the industrial FE code `code_aster`; I further developed constrained formulations for unsteady PDEs to ensure long-term stability of Galerkin ROMs for turbulent flows; finally, I devised weighted least-square Petrov-Galerkin formulations for steady-state conservation laws.

- *Nonlinear model reduction based on coordinate transformations.* I proposed a new optimization-based framework to the problem of registration in bounded domains. Registration aims to identify and then track coherent structures of compact support through the vehicle of a smooth, parametric bijection from the domain Ω in itself. I developed and analyzed a parametric registration technique for arbitrary two-dimensional domains; furthermore, I proposed an actionable methodology to couple the method with linear-subspace PROMs and mesh adaptation. I further proposed a nonlinear interpolation strategy — dubbed convex displacement interpolation — that exploits registration techniques to define parameter-dependent modal expansions.

- *Component-based model reduction of nonlinear PDEs.* I proposed a new data compression strategy that combines localized training based on oversampling and randomized prescription of boundary conditions with adaptive enrichment .for nonlinear steady-state problems. I further proposed an optimization-based domain decomposition method that relies on the decomposition of the local states into a port component — associated with the solution on interior boundaries — and a bubble component that vanishes at ports to formulate the coupled reduced system as a nonlinear least-squares problem that can be solved using the Gauss-Newton method.

I believe that the results presented in this manuscript show the promise of the proposed methods and also motivate further investigations: to provide concrete examples, I am particularly interested in the development of effective variational space-time formulations, the extension of registration techniques to three-dimensional problems, and the development of component-based MOR methods based on locally-trained inter-operable parametric components for unsteady PDEs.

In the future, I plan to keep working on MOR of parameterized systems with particular emphasis on two subjects: application of MOR to inverse problems (parameter calibration, design & optimization), and structure preservation.

- *MOR for inverse problems.* The development of effective MOR techniques for inverse problems is particularly challenging due to the absence of a clear separation between offline and online stage, which forces the on-the-fly constructions and updates of the PROM. Towards this end, we should develop sharp goal-oriented *a posteriori* error estimators. Furthermore, we should also devise multi-fidelity optimization strategies that are able to combine information from models of different accuracy.

- *Structure preservation.* Several independent studies have shown the importance of preserving structural properties of the PDE system in the reduction process. Typical structural properties include pointwise properties (e.g., positivity of density and pressure in compressible flows, non-negativity of water height in hydraulics) and dynamic properties (e.g., energy/entropy conservation): the former are typically ensured using variable transformations, while the latter require a careful choice of the projection scheme, time discretization, and hyper-reduction.

Bibliography

[1] S. R. Ahmed, G. Ramm, and G. Faltin. Some salient features of the time-averaged ground vehicle wake. *SAE transactions*, pages 473–503, 1984.

[2] S. R. Allmaras and F. T. Johnson. Modifications and clarifications for the implementation of the Spalart-Allmaras turbulence model. In *Seventh international conference on computational fluid dynamics (ICCFD7)*, volume 1902. Big Island, HI, 2012.

[3] D. Amsallem and C. Farhat. Interpolation method for adapting reduced-order models and application to aeroelasticity. *AIAA journal*, 46(7):1803–1813, 2008.

[4] H. Antil, S. E. Field, F. Herrmann, R. H. Nochetto, and M. Tiglio. Two-step greedy algorithm for reduced order quadratures. *Journal of Scientific Computing*, 57:604–637, 2013.

[5] L. Arpaia, H. Beaugendre, L. Cirrottola, A. Froehly, M. Lorini, L. Nouveau, and M. Ricchiuto. H-and r-adaptation on simplicial meshes using MMG tools. In *Mesh Generation and Adaptation: Cutting-Edge Techniques*, pages 183–208. Springer, 2022.

[6] J. Ballani, D. P. Huynh, D. J. Knezevic, L. Nguyen, and A. T. Patera. A component-based hybrid reduced basis/finite element method for solid mechanics with local nonlinearities. *Computer Methods in Applied Mechanics and Engineering*, 329:498–531, 2018.

[7] F. Ballarin, E. Faggiano, S. Ippolito, A. Manzoni, A. Quarteroni, G. Rozza, and R. Scrofani. Fast simulations of patient-specific haemodynamics of coronary artery bypass grafts based on a POD–Galerkin method and a vascular shape parametrization. *Journal of Computational Physics*, 315:609–628, 2016.

[8] J. Barnett and C. Farhat. Quadratic approximation manifold for mitigating the Kolmogorov barrier in nonlinear projection-based model order reduction. *Journal of Computational Physics*, 464:111348, 2022.

[9] N. Barral. *Time-accurate anisotropic mesh adaptation for three-dimensional moving mesh problems.* PhD thesis, Université Paris 6 Pierre et Marie Curie, 2015.

[10] N. Barral, G. Olivier, and F. Alauzet. Time-accurate anisotropic mesh adaptation for three-dimensional time-dependent problems with body-fitted moving geometries. *Journal of Computational Physics*, 331:157–187, 2017.

[11] M. Barrault, Y. Maday, N. C. Nguyen, and A. T. Patera. An 'empirical interpolation'method: application to efficient reduced-basis discretization of partial differential equations. *Comptes Rendus Mathematique*, 339(9):667–672, 2004.

[12] F. Bassi and S. Rebay. A high-order accurate discontinuous finite element method for the numerical solution of the compressible Navier–Stokes equations. *Journal of computational physics*, 131(2):267–279, 1997.

[13] P. Benner, M. Ohlberger, A. Cohen, and K. Willcox. *Model reduction and approximation: theory and algorithms.* SIAM, 2017.

[14] M. Bergmann, A. Ferrero, A. Iollo, E. Lombardi, A. Scardigli, and H. Telib. A zonal Galerkin-free POD model for incompressible flows. *Journal of Computational Physics*, 352:301–325, 2018.

[15] P. J. Blonigan, K. Carlberg, F. Rizzi, M. Howard, and J. A. Fike. Model reduction for hypersonic aerodynamics via conservative LSPG projection and hyper-reduction. In *AIAA Scitech 2020 Forum*, page 0104, 2020.

[16] M. Braack, E. Burman, V. John, and G. Lube. Stabilized finite element methods for the generalized Oseen problem. *Computer Methods in Applied Mechanics and Engineering*, 196(4-6):853–866, 2007.

[17] C.-H. Bruneau and M. Saad. The 2D lid-driven cavity problem revisited. *Computers & fluids*, 35(3):326–348, 2006.

[18] A. Buhr. Exponential convergence of online enrichment in localized reduced basis methods. *IFAC-PapersOnLine*, 51(2):302–306, 2018.

[19] A. Buhr and K. Smetana. Randomized local model order reduction. *SIAM journal on scientific computing*, 40(4):A2120–A2151, 2018.

[20] K. Carlberg, C. Farhat, J. Cortial, and D. Amsallem. The GNAT method for nonlinear model reduction: effective implementation and application to computational fluid dynamics and turbulent flows. *Journal of Computational Physics*, 242:623–647, 2013.

[21] S. Chaturantabut and D. C. Sorensen. Nonlinear model reduction via discrete empirical interpolation. *SIAM Journal on Scientific Computing*, 32(5):2737–2764, 2010.

[22] E. T. Chung, Y. Efendiev, and W. T. Leung. Residual-driven online generalized multiscale finite element methods. *Journal of Computational Physics*, 302:176–190, 2015.

[23] R. R. Craig Jr and M. C. Bampton. Coupling of substructures for dynamic analyses. *AIAA journal*, 6(7):1313–1319, 1968.

[24] J. H. Curry, J. R. Herring, J. Loncaric, and S. A. Orszag. Order and disorder in two-and three-dimensional bénard convection. *Journal of Fluid Mechanics*, 147:1–38, 1984.

[25] W. Dahmen, C. Plesken, and G. Welper. Double greedy algorithms: Reduced basis methods for transport dominated problems. *ESAIM: Mathematical Modelling and Numerical Analysis*, 48(3):623–663, 2014.

[26] N. Dal Santo and A. Manzoni. Hyper-reduced order models for parametrized unsteady navier-stokes equations on domains with variable shape. *Advances in Computational Mathematics*, 45(5):2463–2501, 2019.

[27] C. Dapogny, C. Dobrzynski, and P. Frey. Three-dimensional adaptive domain remeshing, implicit domain meshing, and applications to free and moving boundary problems. *Journal of computational physics*, 262:358–378, 2014.

[28] E. de France. Finite element *code_aster*, analysis of structures and thermomechanics for studies and research. Open source on www.code-aster.org, 1989.

[29] S. A. de Parga, J. Bravo, J. Hernández, R. Zorrilla, and R. Rossi. Hyper-reduction for Petrov–Galerkin reduced order models. *Computer Methods in Applied Mechanics and Engineering*, 416:116298, 2023.

[30] J. L. Eftang and A. T. Patera. Port reduction in parametrized component static condensation: approximation and a posteriori error estimation. *International Journal for Numerical Methods in Engineering*, 96(5):269–302, 2013.

[31] R. Everson and L. Sirovich. Karhunen–Loeve procedure for gappy data. *JOSA A*, 12(8):1657–1664, 1995.

[32] C. Farhat, T. Chapman, and P. Avery. Structure-preserving, stability, and accuracy properties of the energy-conserving sampling and weighting method for the hyper reduction of nonlinear finite element dynamic models. *International journal for numerical methods in engineering*, 102(5):1077–1110, 2015.

[33] C. Farhat, S. Grimberg, A. Manzoni, and A. Quarteroni. Computational bottlenecks for PROMs: precomputation and hyperreduction. *Model order reduction*, 2:181–244, 2020.

[34] P. F. Fischer, J. W. Lottes, and S. G. Kerkemeier. nek5000 web page, 2008.

[35] L. P. Franca and S. L. Frey. Stabilized finite element methods: II. The incompressible Navier-Stokes equations. *Computer Methods in Applied Mechanics and Engineering*, 99(2-3):209–233, 1992.

[36] T. Gelhard, G. Lube, M. A. Olshanskii, and J.-H. Starcke. Stabilized finite element schemes with LBB-stable elements for incompressible flows. *Journal of computational and applied mathematics*, 177(2):243–267, 2005.

[37] M. Guo and J. S. Hesthaven. Reduced order modeling for nonlinear structural analysis using Gaussian process regression. *Computer methods in applied mechanics and engineering*, 341:807–826, 2018.

[38] B. Haasdonk. Reduced basis methods for parametrized PDEs–a tutorial introduction for stationary and instationary problems. *Model reduction and approximation: theory and algorithms*, 15:65, 2017.

[39] B. Haasdonk and M. Ohlberger. Reduced basis method for finite volume approximations of parametrized linear evolution equations. *ESAIM: Mathematical Modelling and Numerical Analysis*, 42(2):277–302, 2008.

[40] S. Haker, L. Zhu, A. Tannenbaum, and S. Angenent. Optimal mass transport for registration and warping. *International Journal of computer vision*, 60:225–240, 2004.

[41] P. Henning and D. Peterseim. Oversampling for the multiscale finite element method. *Multiscale Modeling & Simulation*, 11(4):1149–1175, 2013.

[42] J.-M. Hervouet. *Hydrodynamics of free surface flows: modelling with the finite element method.* John Wiley & Sons, 2007.

[43] R. Herzog and K. Kunisch. Algorithms for PDE-constrained optimization. *GAMM-Mitteilungen*, 33(2):163–176, 2010.

[44] J. S. Hesthaven, G. Rozza, and B. Stamm. *Certified reduced basis methods for parametrized partial differential equations*, volume 590. Springer, 2016.

[45] C. Himpe, T. Leibner, and S. Rave. Hierarchical approximate proper orthogonal decomposition. *SIAM Journal on Scientific Computing*, 40(5):A3267–A3292, 2018.

[46] R. Horaud, F. Forbes, M. Yguel, G. Dewaele, and J. Zhang. Rigid and articulated point registration with expectation conditional maximization. *IEEE Transactions on Pattern Analysis and Machine Intelligence*, 33(3):587–602, 2010.

[47] W. Huang and R. D. Russell. *Adaptive moving mesh methods*, volume 174. Springer Science & Business Media, 2010.

[48] W. C. Hurty. Dynamic analysis of structural systems using component modes. *AIAA journal*, 3(4):678–685, 1965.

[49] D. B. P. Huynh, D. J. Knezevic, and A. T. Patera. A static condensation reduced basis element method: approximation and a posteriori error estimation. *ESAIM: Mathematical Modelling and Numerical Analysis*, 47(1):213–251, 2013.

[50] D. B. P. Huynh, G. Rozza, S. Sen, and A. T. Patera. A successive constraint linear optimization method for lower bounds of parametric coercivity and inf–sup stability constants. *Comptes Rendus Mathematique*, 345(8):473–478, 2007.

[51] K. Kaneko, P.-H. Tsai, and P. Fischer. Towards model order reduction for fluid-thermal analysis. *Nuclear Engineering and Design*, 370:110866, 2020.

[52] S. Kaulmann, B. Flemisch, B. Haasdonk, K.-A. Lie, and M. Ohlberger. The localized reduced basis multiscale method for two-phase flows in porous media. *International Journal for Numerical Methods in Engineering*, 102(5):1018–1040, 2015.

[53] C. T. Kelley and D. E. Keyes. Convergence analysis of pseudo-transient continuation. *SIAM Journal on Numerical Analysis*, 35(2):508–523, 1998.

[54] S. G. Krantz and H. R. Parks. *The implicit function theorem: history, theory, and applications.* Springer Science & Business Media, 2002.

[55] T. Lassila, A. Manzoni, A. Quarteroni, and G. Rozza. Model order reduction in fluid dynamics: challenges and perspectives. In *Reduced Order Methods for modeling and computational reduction*, pages 235–273. Springer, 2014.

[56] K. Lee and K. T. Carlberg. Model reduction of dynamical systems on nonlinear manifolds using deep convolutional autoencoders. *Journal of Computational Physics*, 404:108973, 2020.

[57] H. Lienhart, C. Stoots, and S. Becker. Flow and turbulence structures in the wake of a simplified car model (Ahmed model). In *New Results in Numerical and Experimental Fluid Mechanics III. Notes on Numerical Fluid Mechanics (NNFM)*, 2002.

[58] P.-L. Lions. On the Schwarz alternating method. I. In *First international symposium on domain decomposition methods for partial differential equations*, volume 1, page 42. Paris, France, 1988.

[59] A. Loseille and F. Alauzet. Continuous mesh framework part I: well-posed continuous interpolation error. *SIAM Journal on Numerical Analysis*, 49(1):38–60, 2011.

[60] A. Loseille and F. Alauzet. Continuous mesh framework part II: validations and applications. *SIAM Journal on Numerical Analysis*, 49(1):61–86, 2011.

[61] E. Luke, E. Collins, and E. Blades. A fast mesh deformation method using explicit interpolation. *Journal of Computational Physics*, 231(2):586–601, 2012.

[62] J. Ma, W. Qiu, J. Zhao, Y. Ma, A. L. Yuille, and Z. Tu. Robust L_2 E estimation of transformation for non-rigid registration. *IEEE Transactions on Signal Processing*, 63(5):1115–1129, 2015.

[63] J. Ma, J. Wu, J. Zhao, J. Jiang, H. Zhou, and Q. Z. Sheng. Nonrigid point set registration with robust transformation learning under manifold regularization. *IEEE transactions on neural networks and learning systems*, 30(12):3584–3597, 2018.

[64] Y. Maday, A. T. Patera, and D. V. Rovas. A blackbox reduced-basis output bound method for noncoercive linear problems. In D. Cioranescu and J. L. Lions, editors, *Nonlinear Partial Differential Equations and Their Applications, Stud. Math. Appl.*, pages 533–569, 2002.

[65] B. Maiseli, Y. Gu, and H. Gao. Recent developments and trends in point set registration methods. *Journal of Visual Communication and Image Representation*, 46:95–106, 2017.

[66] MATLAB. *R2022a*. The MathWorks Inc., Natick, Massachusetts, 2022.

[67] M. D. McKay, R. J. Beckman, and W. J. Conover. A comparison of three methods for selecting values of input variables in the analysis of output from a computer code. *Technometrics*, 42(1):55–61, 2000.

[68] J. M. Melenk and I. Babuška. The partition of unity finite element method: basic theory and applications. *Computer methods in applied mechanics and engineering*, 139(1-4):289–314, 1996.

[69] D. Modesti and S. Pirozzoli. A low-dissipative solver for turbulent compressible flows on unstructured meshes, with Open-FOAM implementation. *Computers & Fluids*, 152:14–23, 2017.

[70] I. Mozolevski, E. Süli, and P. R. Bösing. hp-version a priori error analysis of interior penalty discontinuous galerkin finite element approximations to the biharmonic equation. *Journal of Scientific Computing*, 30(3):465–491, 2007.

[71] A. Myronenko and X. Song. Point set registration: Coherent point drift. *IEEE transactions on pattern analysis and machine intelligence*, 32(12):2262–2275, 2010.

[72] F. Nicoud and F. Ducros. Subgrid-scale stress modelling based on the square of the velocity gradient tensor. *Flow, turbulence and Combustion*, 62(3):183–200, 1999.

[73] M. Ohlberger and F. Schindler. Error control for the localized reduced basis multiscale method with adaptive on-line enrichment. *SIAM Journal on Scientific Computing*, 37(6):A2865–A2895, 2015.

[74] A. T. Patera. A spectral element method for fluid dynamics: laminar flow in a channel expansion. *Journal of Computational Physics*, 54(3):468–488, 1984.

[75] B. Peherstorfer. Model reduction for transport-dominated problems via online adaptive bases and adaptive sampling. *SIAM Journal on Scientific Computing*, 42(5):A2803–A2836, 2020.

[76] G. Peyré, M. Cuturi, et al. Computational optimal transport: With applications to data science. *Foundations and Trends® in Machine Learning*, 11(5-6):355–607, 2019.

[77] C. Prud'Homme, D. V. Rovas, K. Veroy, L. Machiels, Y. Maday, A. T. Patera, and G. Turinici. Reliable real-time solution of parametrized partial differential equations: Reduced-basis output bound methods. *J. Fluids Eng.*, 124(1):70–80, 2002.

[78] A. Quarteroni, A. Manzoni, and F. Negri. *Reduced basis methods for partial differential equations: an introduction*, volume 92. Springer, 2015.

[79] A. Quarteroni and A. Valli. *Numerical Approximation of Partial Differential Equations*. Springer Publishing Company, Incorporated, 1st ed. 1994. 2nd printing edition, 2008.

[80] V. Resseguier, E. Mémin, and B. Chapron. Geophysical flows under location uncertainty, Part I Random transport and general models. *Geophysical & Astrophysical Fluid Dynamics*, 111(3):149–176, 2017.

[81] G. Rozza, M. Hess, G. Stabile, M. Tezzele, and F. Ballarin. *Basic ideas and tools for projection-based model reduction of parametric partial differential equations*, pages 1–47. Handbook on Model Order Reduction: Snapshot-Based Methods and Algorithms, De Gruyter, 2021.

[82] G. Rozza, D. B. P. Huynh, and A. T. Patera. Reduced basis approximation and a posteriori error estimation for affinely parametrized elliptic coercive partial differential equations. *Archives of Computational Methods in Engineering*, 15(3):229–275, 2008.

[83] M. Ruzhansky and M. Sugimoto. On global inversion of homogeneous maps. *Bulletin of Mathematical Sciences*, 5(1):13–18, 2015.

[84] D. Ryckelynck. A priori hyperreduction method: an adaptive approach. *Journal of computational physics*, 202(1):346–366, 2005.

[85] D. Ryckelynck. Hyper-reduction of mechanical models involving internal variables. *International Journal for numerical methods in engineering*, 77(1):75–89, 2009.

[86] G. Sambataro. *Réduction de modèle basée sur des composants élémentaires pour des systèmes Thermo-Hydro-Mécaniques.* PhD thesis, Université de Bordeaux, 2022.

[87] D. Shepard. A two-dimensional interpolation function for irregularly-spaced data. In *Proceedings of the 1968 23rd ACM national conference*, pages 517–524, 1968.

[88] L. Sirovich. Turbulence and the dynamics of coherent structures. I. Coherent structures. *Quarterly of applied mathematics*, 45(3):561–571, 1987.

[89] K. Smetana. A new certification framework for the port reduced static condensation reduced basis element method. *Computer methods in applied mechanics and engineering*, 283:352–383, 2015.

[90] P. Spalart and S. Allmaras. A one-equation turbulence model for aerodynamic flows. In *30th aerospace sciences meeting and exhibit*, page 439, 1992.

[91] T. E. Tezduyar. Stabilized finite element formulations for incompressible flow computations. *Advances in applied mechanics*, 28:1–44, 1991.

[92] T. E. Tezduyar and Y. Osawa. Finite element stabilization parameters computed from element matrices and vectors. *Computer Methods in Applied Mechanics and Engineering*, 190(3-4):411–430, 2000.

[93] P.-H. Tsai and P. Fischer. Parametric model-order-reduction development for unsteady convection. *Frontiers in Physics*, page 711, 2022.

[94] K. Veroy, C. Prud'Homme, D. Rovas, and A. Patera. A posteriori error bounds for reduced-basis approximation of parametrized noncoercive and nonlinear elliptic partial differential equations. In *16th AIAA Computational Fluid Dynamics Conference*, page 3847, 2003.

[95] S. Volkwein. Model reduction using proper orthogonal decomposition. *Lecture Notes, Institute of Mathematics and Scientific Computing, University of Graz. see http://www. uni-graz. at/imawww/volkwein/POD. pdf*, 1025, 2011.

[96] K. M. Washabaugh, M. J. Zahr, and C. Farhat. On the use of discrete nonlinear reduced-order models for the prediction of steady-state flows past parametrically deformed complex geometries. In *54th AIAA Aerospace Sciences Meeting*, page 1814, 2016.

[97] H. Wendland. *Scattered data approximation*, volume 17. Cambridge university press, 2004.

[98] M. Yano. A space-time Petrov–Galerkin certified reduced basis method: Application to the Boussinesq equations. *SIAM Journal on Scientific Computing*, 36(1):A232–A266, 2014.

[99] M. Yano. Discontinuous Galerkin reduced basis empirical quadrature procedure for model reduction of parametrized nonlinear conservation laws. *Advances in Computational Mathematics*, 45(5):2287–2320, 2019.

[100] M. Yano, J. Modisette, and D. Darmofal. The importance of mesh adaptation for higher-order discretizations of aerodynamic flows. In *20th AIAA Computational Fluid Dynamics Conference*, page 3852, 2011.

[101] M. Yano and A. T. Patera. An LP empirical quadrature procedure for reduced basis treatment of parametrized nonlinear PDEs. *Computer Methods in Applied Mechanics and Engineering*, 344:1104–1123, 2019.

[102] M. J. Zahr and P.-O. Persson. An optimization-based approach for high-order accurate discretization of conservation laws with discontinuous solutions. *Journal of Computational Physics*, 365:105–134, 2018.

[103] M. J. Zahr, A. Shi, and P.-O. Persson. Implicit shock tracking using an optimization-based high-order discontinuous Galerkin method. *Journal of Computational Physics*, 410:109385, 2020.

Publications of the author

[TT1] E. Agouzal, J.-P. Argaud, M. Bergmann, G. Ferté, S. Michel-Ponnelle, and T. Taddei. Projection-based model order reduction for prestressed concrete with an application to the standard section of a nuclear containment building. *arXiv preprint arXiv:2401.05098*, 2024.

[TT2] E. Agouzal, J.-P. Argaud, M. Bergmann, G. Ferté, and T. Taddei. A projection-based reduced-order model for parametric quasi-static nonlinear mechanics using an open-source industrial code. *International Journal for Numerical Methods in Engineering*, 125(4):n/a, 2024.

[TT3] E. Agouzal and T. Taddei. Accelerated construction of projection-based reduced-order models via incremental approaches. *Advanced Modeling and Simulation in Engineering Sciences*, 11(8), 2024.

[TT4] N. Barral, T. Taddei, and I. Tifouti. Registration-based model reduction of parameterized PDEs with spatio-parameter adaptivity. *Journal of Computational Physics*, 499:112727, 2024.

[TT5] S. Cucchiara, A. Iollo, T. Taddei, and H. Telib. Model order reduction by convex displacement interpolation. in preparation.

[TT6] A. Ferrero, T. Taddei, and L. Zhang. Registration-based model reduction of parameterized two-dimensional conservation laws. *Journal of Computational Physics*, 457:111068, 2022.

[TT7] L. Fick, Y. Maday, A. T. Patera, and T. Taddei. A stabilized POD model for turbulent flows over a range of Reynolds numbers: Optimal parameter sampling and constrained projection. *Journal of Computational Physics*, 371:214–243, 2018.

[TT8] A. Iollo, G. Sambataro, and T. Taddei. An adaptive projection-based model reduction method for nonlinear mechanics with internal variables: Application to thermo-hydro-mechanical systems. *International Journal for Numerical Methods in Engineering*, 123(12):2894–2918, 2022.

[TT9] A. Iollo, G. Sambataro, and T. Taddei. A one-shot overlapping Schwarz method for component-based model reduction: application to nonlinear elasticity. *Computer Methods in Applied Mechanics and Engineering*, 404:115786, 2023.

[TT10] A. Iollo and T. Taddei. Mapping of coherent structures in parameterized flows by learning optimal transportation with Gaussian models. *Journal of Computational Physics*, 471:111671, 2022.

[TT11] K. Smetana and T. Taddei. Localized model reduction for nonlinear elliptic partial differential equations: localized training, partition of unity, and adaptive enrichment. *SIAM Journal on Scientific Computing*, 45(3):A1300–A1331, 2023.

[TT12] T. Taddei. An offline/online procedure for dual norm calculations of parameterized functionals: empirical quadrature and empirical test spaces. *Advances in Computational Mathematics*, 45(5-6):2429–2462, 2019.

[TT13] T. Taddei. A registration method for model order reduction: data compression and geometry reduction. *SIAM Journal on Scientific Computing*, 42(2):A997–A1027, 2020.

[TT14] T. Taddei. An optimization-based registration approach to geometry reduction. *arXiv preprint arXiv:2211.10275*, 2022.

[TT15] T. Taddei. Compositional maps for registration in complex geometries. *arXiv preprint arXiv:2308.15307*, 2023.

[TT16] T. Taddei, X. Xu, and L. Zhang. A non-overlapping optimization-based domain decomposition approach to component-based model reduction of incompressible flows. *Journal of Computational Physics*, accepted.

[TT17] T. Taddei and L. Zhang. A discretize-then-map approach for the treatment of parameterized geometries in model order reduction. *Computer Methods in Applied Mechanics and Engineering*, 384:113956, 2021.

[TT18] T. Taddei and L. Zhang. Registration-based model reduction in complex two-dimensional geometries. *Journal of Scientific Computing*, 88(3):79, 2021.

[TT19] T. Taddei and L. Zhang. Space-time registration-based model reduction of parameterized one-dimensional hyperbolic PDEs. *ESAIM: Mathematical Modelling and Numerical Analysis*, 55(1):99–130, 2021.